Nonlinear Stochastic Dynamics and Signal Amplifications in Sensory Hair Cells

A dissertation presented to

the faculty of

the College of Arts and Sciences of Ohio University

In partial fulfillment

of the requirements for the degree

Doctor of Philosophy

Rami M. A. Amro

August 2015

This dissertation titled

Nonlinear Stochastic Dynamics and Signal Amplifications in Sensory Hair Cells

by

RAMI M. A. AMRO

has been approved for

the Department of Physics and Astronomy

and the College of Arts and Sciences by

Alexander B. Neiman

Associate Professor of Physics and Astronomy

Robert Frank

Dean of College of Arts and Sciences

# Abstract

AMRO, RAMI M. A., Ph.D., August 2015, Physics

Nonlinear Stochastic Dynamics and Signal Amplifications in Sensory Hair Cells (122 pp.)

Director of Dissertation: Alexander B. Neiman

Hair cells are mechanosensors specializing in detection and amplification of weak mechanical stimuli in the auditory and vestibular peripheral sensory systems in vertebrates. In amphibians, hair cells exhibit two distinct mechanisms of amplification: via active motility of the hair bundle and via nonlinear resonant properties of the membrane potential. We use computational and theoretical approaches to study how the interaction of these two mechanisms affect spontaneous dynamics of hair cells and shape their responses to weak mechanical stimuli. We develop a two-compartment model incorporating a Hodgkin–Huxley type system for the membrane potential and a nonlinear stochastic oscillator for the hair bundle. We show that the bidirectional coupling between two compartments affects significantly the dynamics of the cell. Self-sustained oscillations of the hair bundles and membrane potential can result from coupling of initially quiescent mechanical and electrical compartments. The coherence of stochastic spontaneous oscillations can be maximized by tuning the coupling strength. Consistent with previous experimental work, we show that dynamical regimes of the hair bundle change in response to variations in the conductances of basolateral ion channels. Randomness of the hair bundle compartment is a limiting factor of the sensitivity. We found that sensitivity of the hair cell to weak mechanical perturbation is maximized by varying coupling strength. Using an analytical approach we show that such a non-monotonic dependence of sensitivity on coupling strength is a generic property of bidirectionally coupled unequally noisy oscillators. Furthermore, we show analytically that the phase coherence in such systems changes non-monotonically in response to increasing noise levels in the less coherent oscillator, a novel counter–intuitive effect.

*To my father and mother who held my hand and supported me till the last moment, and thereafter.*

# ACKNOWLEDGMENTS

First and foremost I would like to express my deepest gratitude to my PhD advisor Prof. Alexander B. Neiman for the distinguished support, understanding, guidance, encouragement and patience he offered through my study. Without him I couldn't achieve this far.

Throughout my study at Ohio University, I appreciated discussions with faculty and colleagues within and outside the field which always enriched my understanding and established new directions in my thoughts. I am very thankful to all of them. In particular, I would like to thank my PhD committee: Prof. Michael H. Rowe, Prof. David F. J. Tees, Prof. Horacio Castillo, and Prof. Todd Young for their insightful discussions, and guidance through my dissertation. Special thanks to Prof. David F. Russell for the support, advice, and guidance. I really appreciate the time he spent with me doing experiments on sensory receptors in paddlefish back in the summer of 2012, after which I came to appreciate how hard it is to do experiments in live animals. I would like to thank Prof. Benjamin Lindner, Prof. Lutz Schimansky–Geier, and Prof. Andrey Shilnikov for enlightening discussions. Special thanks to Prof. Dolores Bozovic for fruitful discussions, and offering me further opportunity to continue my research in her lab at UCLA. I would like to thank Prof. M.D. A. James Hudspeth, and Prof. Jong–Hoon Nam for their clarifying discussions on hair cell anatomy and dynamics.

I would like to acknowledge financial support from the Condensed Matter and Surface Sciences Program (CMSS), and Quantitative Biology Institute (QBI) at Ohio University. We gratefully acknowledge the support of NVIDIA Corporation with the donation of the Tesla K40 GPU used for this research.

Lastly but most certainly not least, special thanks to my mother Fatima, father Mohammad, brothers and sisters for their unconditional love and support, without whom my life would be full of loneliness.

# Table of Contents

# List of Figures

# GLOSSARY

**Apical side**; is the side of the hair cell which face up toward the otolithic membrane. 8, 11, 13

**Basolateral**; i.e. associated with the cell body or cell membrane, near the base. 9, 54, 71

**Bullfrog sacculus**; is a part of the bullfrog ear in which hair cells are embedded. The cells in this suborgan are responsible for detecting sound or seismic variations. 8, 28

**Cell soma**; a synonym to the cell body. 9, 13, 26

**Compressive nonlinearity**; a phenomenon in which the response to high level stimuli is suppressed as compared to that of small stimuli. 8, 12

**Endolymph**; a solution surrounding the hair bundle, and it is rich with potassium ions, and relatively (with respect to the total concentration of ions) low calcium concentration. 11, 16, 17, 32

**Macula**; is a Latin word which means ”spot”. it is the patch where hair cells reside in. 16

**Otolithic membrane**; is a thick membrane that overlies the hair bundles in the sacculus. In the auditory system, such a membrane is called the tectorial membrane. 14

**Perilymph**; a fluid in which the cell soma is immersed, and it has low potassium and moderate calcium concentrations. 11, 23

**Stereocilia**; is the plural of stereocilium, a stiff rod–like protrusion pinned which appears on the apical side of the cell. 11, 13, 14

**Vestibular periphery**; is the organ that is responsible for the sense of balance in the inner ear. 8

# 1 Introduction

[1] Sensory hair cells are mechanoreceptors transducing mechanical stimuli to electrical signals in auditory and vestibular periphery in vertebrates. The detecting element is located in the hair bundle, a ciliated structure on the apical side of the cell, which possesses mechanically gated ion channels: they open or close in response to deflection of the hair bundle. In this way, deflection of the hair bundle is transferred to a flow of positively charged ions (mostly potassium) which depolarize the cell body. Exquisite sensitivity, frequency selectivity, and compressive nonlinearity are pronounced characteristics of sensory hair cells [13–16]. These characteristics are due to active processes in the machinery of both nonmammalian [7, 17] and mammalian hair cells [18] (see [1] for a recent review). In particular, in some low-frequency nonmammalian hair cells, these active processes may result in spontaneous oscillations of the hair bundles [8], which enhances sensitivity and selectivity of the hair cell [19] and may result in collective phenomenon of otoacoustic emission [20, 21]. Spontaneous hair bundle oscillations are inherently noisy due to several sources of randomness, which limits sensitivity and selectivity of the hair bundle to weak mechanical stimuli [22]. In bullfrog sacculus, free standing hair bundles exhibit a diverse range of stochastic self-sustained oscillations [8, 9, 23].The frequency of these oscillations ranges from 5–50 Hz, and their amplitude can be as large as 80 nm [8]. Several studies suggested that the hair bundle may operate on the verge of Andronov–Hopf bifurcation, which provide the hair cell with giant sensitivity and sharp selectivity, along with the compressive nonlinearity [15, 16, 24, 25]. Variations of the membrane potential affect the hair bundle dynamics and the mechano-electrical transduction. Earlier studies documented the phenomenon called reverse electro-mechanical transduction in which voltage and hair bundle flutuations recorded simultaneously were correlated. Hair bundles deflect in response to somatic electrical stimulation [26, 27]. Inhibition of basolateral

[1] Part of this section was published in Amro and Neiman (2014) [12].

potassium currents results in drastic changes in spontaneous dynamics of the hair bundle [11].

Despite these theoretical and experimental findings, the role of these electrical oscillations and bidirectional coupling in shaping the spontaneous and response dynamics of the hair cell are still unknown. Partly, this is due to experimental difficulties in simultaneous recording of the hair bundle displacement and the membrane potential, which call for a modeling approach.

This Dissertation uses a modeling approach and methods of nonlinear dynamics to study how the interaction between hair bundle and the cell soma membrane potential affects the emergence of distinct dynamical regimes, and the role of this interaction in shaping the response of the hair cell to weak mechanical stimuli. It employs a model of the bullfrog saccular hair cells. Saccular hair cells of bullfrog are in use by many experimental groups as a well developed experimental model to study general principles of auditory sensory physiology.

## 1.1 Hearing in mammals

The hearing organ in mammals is divided into three parts: outer ear, middle ear, and inner ear. Starting from the external ear, sound waves (composed of compressions and rarefactions regions) propagate through the ear canal knocking the ear drum (*tympanic membrane*) which marks the end of the outer ear. Pressure variations on the tympanic membrane shake the three minuscule bones (*ossicles*, see Fig. 1.1–A); the malleus, incus, and the stapes. These minuscule bones in turn transfer the mechanical vibrations to the cochlea through repetitive hits into small oval–shaped membrane (*oval window*) near the base of the cochlea and opens in the scala vestibuli (Fig. 1.1–B). Vibrations on the oval window are transformed into surface waves propagating along the snail shaped, fluid filled cochlea [16]. The energy of these waves is dissipated into the viscous fluid as they

propagate. Compressions and expansions of this viscous fluid are translated into transverse signals on two elastic structures; the basilar membrane, and Ressner's membrane.

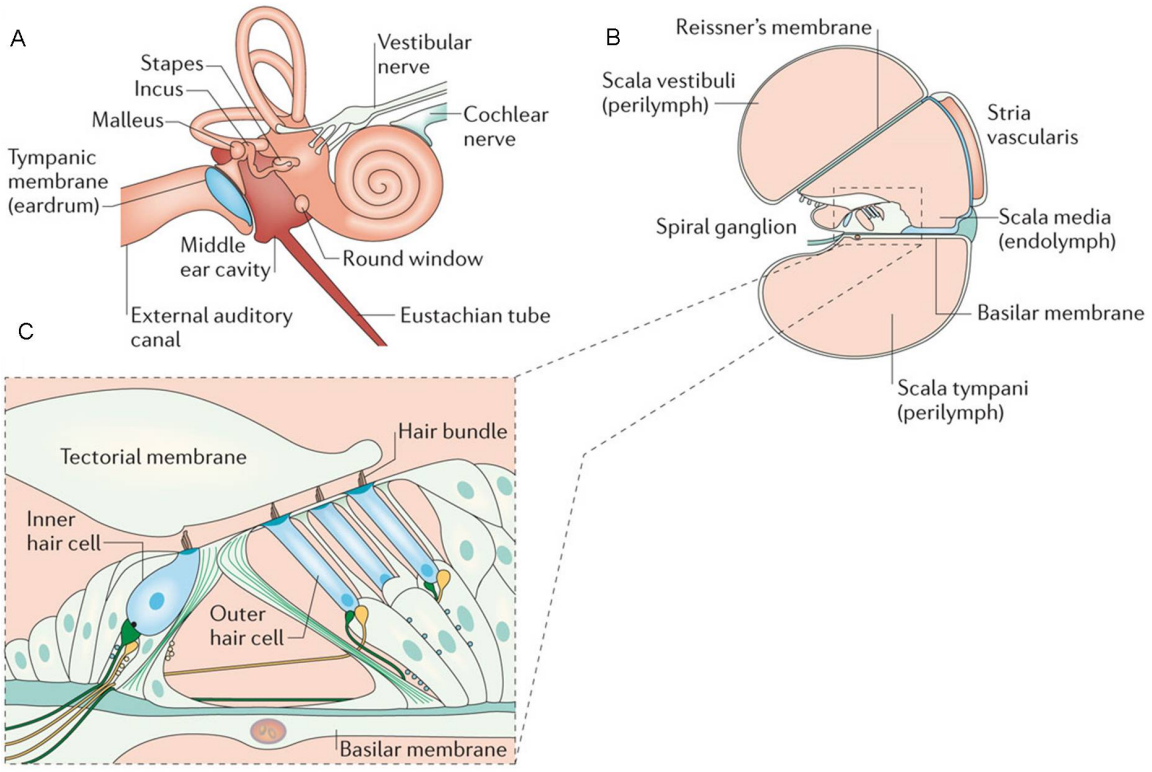


Figure 1.1: Schematic diagram of the human ear. (A) The main components of the human ear: the external ear (ear canal, and tympanic membrane), middle ear (the three miniscule bones; malleus, incus, and stapes), and the inner ear (semicircular canal, and the spiral shaped organ called the cochlea). (B) Cross section of the unfolded cochlea with the three scalae partitions shown and the organ of corti (dashed-line square). (C) A zoom in view of the organ of Corti. In this view, one line of inner hair cells and three lines of outer hair cells surrounded by supporting cells and embedded on the top of the basilar membrane, with techtorial membrane overlying their hair bundles. Reprinted by permission from Macmillan Publishers Ltd: Nature Reviews Neuroscience [1], copyright 2014.

The unfolded cochlea, the basilar membrane extends along the cochlea. Located on the basilar membrane is the organ of Corti, in which one line of inner hair cells (IHCs) and three to five lines of outer hair hair cells (OHCs) are embedded. IHCs are smaller, rounded and responsible for acoustical sensing, while OHCs are elongated and reserved

for the cochlear amplification [18]. Each ear contains ~15000 of these hair cells (OHCs and IHCs combined).

Hair cells are mainly composed of a group of fine protrusions on the apical side, termed as the hair bundle due to its ciliated structure, and a cell body which is located on the basal side. The hair bundle is immersed in viscous endolymph which has an excess of potassium and low calcium concentration, while the cell body is immersed in low potassium and moderate calcium perilymph. Overlying these hair cells is a gelatinous like membrane (*tectorial membrane*) and plays a major role in coupling the motion of these hair bundles.

Each hair bundle is composed of 20-300 stereocilia arranged in rows of increasing height, each stereocilium has one or two mechanically sensitive ion channels. Travelling waves along the basilar membrane displace the hair bundle, leading to a shearing motion of the hair bundle against the tectorial membrane. The shearing motion of the adjacent stereocilia triggers the opening of the mechanoelectrical transduction (MET) ion channels, causing the inflow of positively charged ions which depolarize the cell membrane; the large variations in the membrane potential trigger action potentials in the associated auditory–nerve fibers through the release of neurotransmitters [16]. These action potentials propagate to the central nervous system, Consequently, the mechanical stimulus is encoded into electrical signal.

Human hearing spans three orders of magnitude in frequency; we can detect sounds in the frequency range 20–20000 Hz, and resolve tones which differ in frequency by 0.5%. Moreover, sounds at the threshold of hearing (0 dB) result in small (sub-nanometer) displacements on the the basilar membrane which are comparable to thermal fluctuations, while sounds with high intensity (120 dB, a million times larger in amplitude) results only in nearly 10 nm displacements on the basilar membrane [14]. This remarkable amplifications of small amplitude perturbations and compression of large amplitude stimuli requires the existence of active process and nonlinearity in the cochlea.

Early in 1863 Hermann von Helmholtz suggested that the cochlea is a passive detector, and so it works like a linear Fourier analyzer. However, the sharp frequency selectivity observed in human hearing is unexplainable with this analogy if we consider the damped behavior of these waves and the broadening in their spectra due to the presence of the viscous fluid in the cochlea. Later on, George von Békésy in 1920's observed that the basilar membrane is thick and stiff at the base, while it is thinner and more elastic near the apex. Using intensive sound pressure levels stimulation (120-140 dB due to the equipment limitations), Békésy noticed that the amplitude of the travelling wave peaks at a frequency-dependent location on the basilar membrane. Moreover, the response of the basilar membrane is in linear relation with the stimulus amplitude. In 1971, in contrast to Békésy's linear cochlea assumption, Rhode in his experiments on squirrel monkey showed that the cochlea exhibits frequency dependent nonlinearity, and the response to pure-tone low amplitude stimulus is linear, while that for large amplitude stimulus is suppressed tremendously in a phenomenon later known as *compressive nonlinearity*: the basilar membrane sensitivity follow a power law with an exponent $-2/3$ for large amplitude stimuli [28]. The observations of poor frequency selectivity by Békésy in dead cochlea was confronted by large frequency selectivity and sharp tuning curves in other mammals [29], indicating that the existence of a nonlinear process and amplifications. Therefore, the live cochlea is better described as an active system.

In addition to these observations, a healthy mammalian ear not only works as a detector and amplifier, but is also capable of emitting sounds. This remarkable discovery was made in 1978 by Kemp, and termed as spontaneous otoacoustic emission (SOAE) [30]: the ear emitting sounds in a quiet environment. Later on, this astonishing observation was attributed to unknown nonlinear mechanisms located in the cochlear amplifier [31]. In the 1980s, the SOAE phenomenon was shown to exist in many mammalian and nonmammalian species [32–35]. The origin of this process may be caused by two different activities in the

inner ear: OHCs in humans posses the capability of changing their length in response to hyperpolarization and depolarization of their membrane potential (electromotility) [36,37], and so the tectorial membrane will shake in response to the longitudinal motion of these hair cells, resulting in travelling waves on the basilar membrane. As a result a microphone installed in the ear canal will detect threshold oscillations in a quiet environment. The second possible mechanism is the spontaneous activity of the hair bundle [5]. In lower vertebrates, *in vitro* spontaneous oscillations of the hair bundle were observed in several species including frogs [5, 8], and chicken [38] and thought to contribute to SOAE.

Despite differences in the hearing and vestibular organs among vertebrates, sensory hair cells have similar structure. Hair cells are mainly composed from ciliated structure at the apical side (hair bundle). The hair bundle is composed of tens of stereocilia (plural of stereocilium). Each hair bundle is populated with several MET channels, which conduct ionic current upon opening due to the deflection of the hair bundle. On the basal side, each sensory hair cell has a cell soma, which is also populated with several thousands of voltage gated ion channels. The sensory nerves communicate with the hair cell through chemical synapses.

Sensory hair cells also exist in the vestibular system, which is composed of five organs: three semicircular canals specialized to detect the head acceleration as it has six degrees of freedom; the other two organs are the saccule and the utricle and are responsible for gravitational sensing. Each of these organs has several thousands hair cells. Overlying these hair cells is a gelatinous membrane and on top of is a fibrous layer called the *otolithic membrane*.

## 1.2 Bullfrog saccular hair cells

Depending on the amplitude and frequency of the incoming stimulus, a specific endorgan/s of the bullfrog auditory/vestibular system will respond: three endorgans coexist

in bullfrog, The sacculas which is capable of detecting sound/seismic frequencies in the range 20-120 Hz, the amphibian papilla detects sounds with 100-1250 Hz, and the basilar papilla which responds to high frequency sounds up to 2000 Hz. This wide detection range is attributed partly to physiological variations of the detecting element: ciliated-hair cells are physiologically different among these endorgans (they may vary in the same organ too, such as in amphibian and basilar papilla). Such physiological variations modify the detection capabilities of the hair cells [39, 40] within these suborgans.

The bullfrog saccular hair cells are specialized in detecting sound and seismic variations. The sensory epithelium contains several thousands of them [41]. Each is composed of a tuft of stiff stereocilia arranged in quasi-hexagonal shape [42] and sits on the apical surface of the cell body. Each hair bundle is capped in the otolithic membrane (25-30 $\mu$m thick) which overlies these hair cells [41]. In the plane of bilateral symmetry, they are arranged from shorter to taller stereocilium in stair case shape [43]. On the taller side of the tuft, there is a larger stereocilium, called the kinocilium [43]. The kinocilium is the only cilium attached to the otolithic membrane, and imposes an offset on the hair bundle position.

The number of stereocilia in a single hair bundle falls in the range of 50-60 stereocilium [3, 44, 45], and they vary within 1-15 $\mu$m in height as indicated in Fig. 1.2–A, and B. The oblique gating spring (*tip link*) connects every stereocilium to the MET channel's gating swing on the neighbouring stereocilium as shown in Fig. 1.2–C, D [43, 46, 47]. Studies showed that these tip links are made of helical strands of cadherin23 and protocadherin15 [48, 49], their diameter fall within 5-8 nm, and are 150–200 nm in length [45, 47]. A stiff actin filaments exists at the core of each individual stereoclium [43]. Each stereocilium is nearly 400 nm in diameter [50], and tapers to 100 nm at its base at which only few tens of actin filaments in its rootlet as compared to 600 actin filament in its bulk. These variations in the number of the actin cores make the stereocilium very

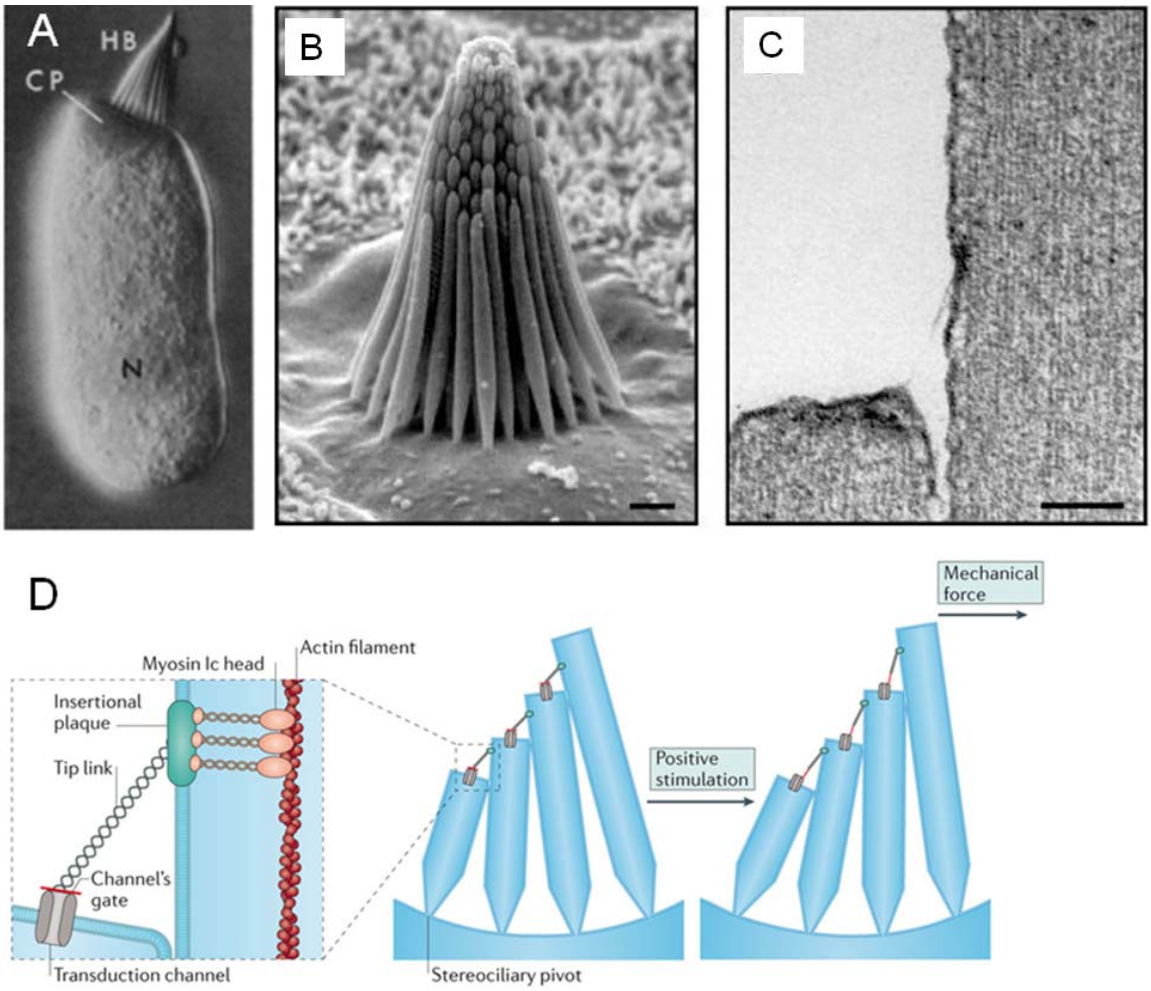


Figure 1.2: Bullfrog saccular hair cells. (A) A light micrograph image of bullfrog saccular hair cell with the hair bundle attached with cell soma containing the nucleus (N), from [2]. Reprinted with permission from AAAS. (B) A hair bundle (scale bar= 1 $\mu$ m). (C) A tip link connecting two neighbouring stereocilia (scale bar = 0.1 $\mu$ m). Modified from [3]. (D) Schematic diagram of the hair bundle; (left) a zoom in view of the transduction machinery (middle) with the main components shown. (Right) MET channels are in the open state upon applying positive mechanical stimulus. Reprinted by permission from Macmillan Publishers Ltd: Nature Reviews Neuroscience [1], copyright 2014.

brittle [51] at the insertion point in the cuticular plate. The concavity of the cuticular plate, and tip links preserve the hair bundle's rigidity [52, 53], thus, for angular deflections up to 30 deg (< 300 nm) the hair bundle moves as single object [43, 53]. In addition to tip links,

other types of lateral cross links between neighbouring stereocilia exist. Studies showed that the hair bundle maintains its rigidity (sliding adhesion) even when these additional lateral connections are cut [53].

*In vivo* saccular hair cells are aggregated in terms of activation polarity (the direction toward the right in Fig. 1.2–D middle and right panels), mostly to two regions across the macula [41]. They operate in groups due to the existence of the otolithic membrane which reduces noise effects, suppresses spontaneous activity,and phase–locks the motion of these hair cells [27, 54]. Indeed, biophysical models showed that coupling hair bundles reduces noise level, enhances sensitivity, frequency selectivity, and amplification [55–58].

## 1.3 Adaptation in hair cells

Due to the high concentration of potassium and moderate calcium concentration in the viscous endolymph [59], sustained positive stimulus on the hair bundle intensify the tip links, leading to building pressure on the MET channels gate, causing them to open. Experimental studies showed that upon opening of the MET channels, an abrupt increase in the transduction current, which is mainly composed of potassium ions and minor (10%) contribution of calcium ions, followed by fast negative displacement of the hair bundle (called as the twitch, Fig. 1.3–B) for a short time period. Later on, the hair bundle proceeds with a relaxing motion in the same direction as the stimulus, resulting in saturating decrease in the current versus time relationship (cf. Fig. 1.3–B). By recording the peak value of the current for gradually increasing stimulus magnitudes, studies showed that the current-displacement relationship follows a smooth sigmoid as in Fig. 1.3–A. Doing the experiment again but after applying +700 nm a positive offset in place, a shift of the current-displacement curve in the same direction of the imposed offset was observed (Fig. 1.3–A). Both observations indicate the existence of an adaptation mechanism responsible for moderating the time course of the channels' opening, and adjusting the hair bundle position

so that it sustains its response to imposed stimuli. Adaptation of the hair bundle to static stimulus is observed in different animals' [60] auditory and vestibular organs, such as in turtles, birds, and mammals. Albeit, adaptation times in the bullfrog saccular hair cells are lower than those in turtle [60] and mouse [61] auditory hair cells due to differences in the characteristic frequencies of hair bundles between these species.

Although the adaptation mechanism is not fully understood , many experimental studies have been carried out to investigate this astonishing behavior. Experiments which are done using different ionic concentrations of the endolymph showed that the effect is remarkably reduced for lower concentrations of calcium in the endolymph [62–64], indicating the existence of an intracellular component that is responsible for the adaptation mechanism, whose activity is calcium dependent. Nevertheless, experiments performed on mammalian hair cells show that the adaptation mechanism is *not* calcium dependent, and at best, calcium can bind to an extracellular element and modulate the resting open probability of the MET channels [65].

As mentioned earlier, two phases of adaptation exist (for review, see [1]), with the fast phase preceding the slower one. In both phases, $Ca^{2+}$ is hypothesised to play a significant role [45, 60, 64, 66, 67]: $Ca^{2+}$ may bind to MET channel and stabilize the closed state [45] through conformational changes [45]. Alternatively, $Ca^{2+}$ may bind to a "release element" that slackens the tip links and renders the MET channel in the closed state [61]. In addition, $Ca^{2+}$ may bind to intracellular "reclosure element" in series with the tip link, reducing its tension and allowing the channel to close [26]. This phenomenon was termed as the 'twitch' [68, 69] and serves as fast adaptation process as it lasts for sub-milliseconds [45, 66], or 0.5 to 5 ms [60], despite these speculations, the exact origin of fast adaptation is still unknown.

Unlike fast adaptation, slow adaptation is mediated by the activity of groups of myosin-1c molecular motors [66, 70]. These motors (perhaps 50 motors) are attached on

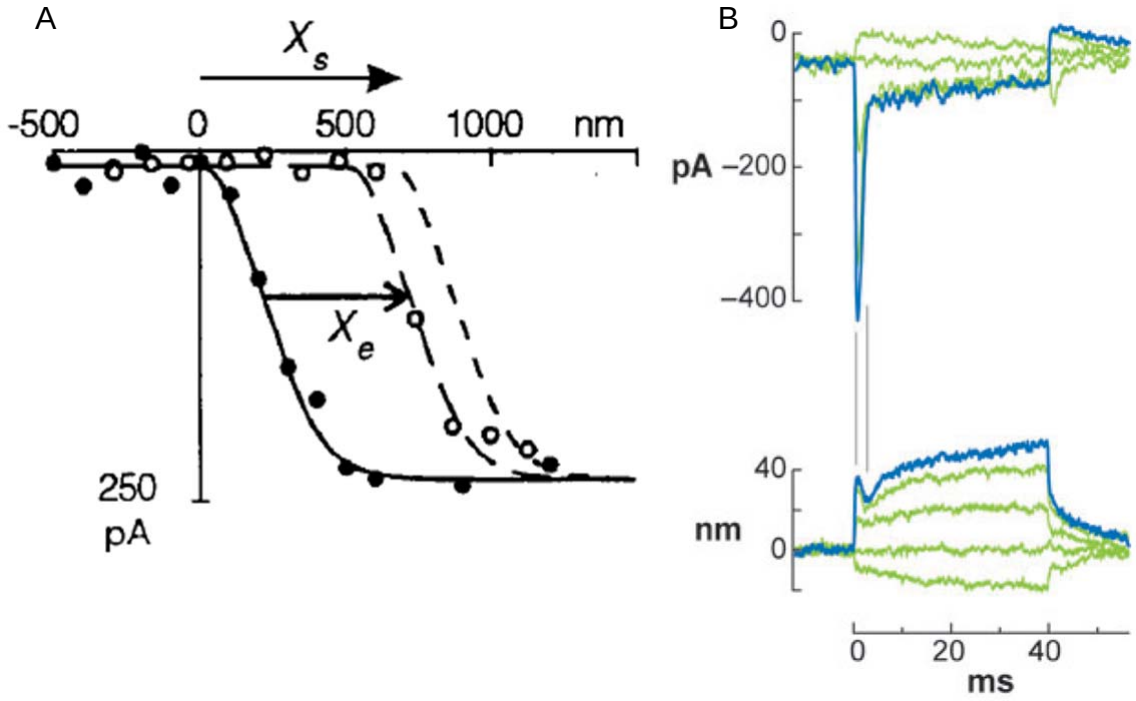


Figure 1.3: Effect of static offset on the current versus displacement curve in bullfrog saccular hair cells. (A) Current-displacement curve before (filled dots) and after (circles) applying 700 nm positive offset [4]. (B) Transduction current (top), and hair bundle displacement (bottom) in response to positive and negative stimulus steps, the blue curve corresponds to positive step. Modified from [3]

one end to the actin core, and on the other end to the insertional plaque [71] near the MET channel. Located toward the tail of myosin-1c complex is the protein cadherin23 [45, 60, 64, 66, 67], which is populated with $Ca^{2+}$ binding sites. According to the gating spring model, upon positive deflection of the hair bundle; $Ca^{2+}$ ions flow in the cell, and bind to cadherin23. The binding of $Ca^{2+}$ causes the transduction complex (insertional plaque, and possibly the MET channel) to slip down over a time course of tens of milliseconds, and at a rate of ~1-2 $\mu$m/s. Note that the slippage rate is similar to that of the motion of myosin-1c along the actin core [72]. The slippage of the transduction complex relaxes the tension exerted by the tip links on the channel's gate, allowing it to regulate the transduction current, and restore the hair bundle sensitivity [45]. Similarly,

for negative stimuli, molecular motors actively climb along the actin core, increasing the tension on the tip links and so restore the resting open probability of the channels. Despite similarities in the slow adaptation mechanism for positive and negative offsets, the shift in the current versus displacement curve is asymmetric. It proceeds at larger but constant rates for positive offsets, and slower tension–dependent rates for negative ones [72]. A much faster component on the order of few hundreds of microseconds also exists, and thought to be voltage dependent as it acts on tip links, or the MET channel, but doesn't require current through the MET channel [68].

A careful look at the shift (Fig. 1.3–A), shows that the curve only shifted by 80% relative to the magnitude of the imposed offset [4], indicating that the adaptation is not complete. Incomplete adaptation implies the existence of an additional intracellular component that pulls on the channel in the opposite direction to the tip links, and so make it easier to close compared to the case when it doesn't exist. In other words, the channels restore the nearly closed state in less hair bundle displacement. This additional component, termed the extent spring, is suggested to be responsible for the incompleteness of the adaptation [70].

## 1.4 Spontaneous oscillations of the hair bundle in the bullfrog saccular hair cells

*In vitro* free–standing hair bundles with the otolithic membrane removed exhibit diverse self-sustained oscillations as indicated in Fig. 1.7–A; such as noisy quiescent, periodic, spiking, or bursting, [8]. Nevertheless, observations *in vivo* showed that the bursting activity is preserved only for cells with the otolithic membrane removed. The frequency of these oscillations ranges from 5-50 Hz, and their amplitude can be as large as 80 nm [8]. Figure 1.4 shows the activity of hair a bundle which exhibits limit cycle oscillations (A), with the power spectrum (B) indicating the characteristic frequency of the hair bundle. The finite width of the power spectrum curve is a result of the noisy nature of

the hair bundle oscillations and indicative of the quality of the oscillations. The noisy nature of the hair bundle oscillations is thought to be a result of Brownian motion of the bundle due to the viscous endolymph, stochastic opening and closing of MET channels and stochastic binding and unbinding of molecular motors from the actin core [22]. For a passive system in thermal equilibrium, the amplitude of the oscillations should be proportional to the thermal energy. Comparison between the hair bundle response to small stimulus and its autocorrelation function reveals that the hair bundle violates the fluctuation dissipation theorem, indicating that the hair bundle is not in thermal equilibrium with its environment. Therefore, an energy consuming element results in these oscillations, thus, spontaneous activity can't be merely due to thermal fluctuations [5], rather, they represent an example of self–sustained stochastic oscillator.

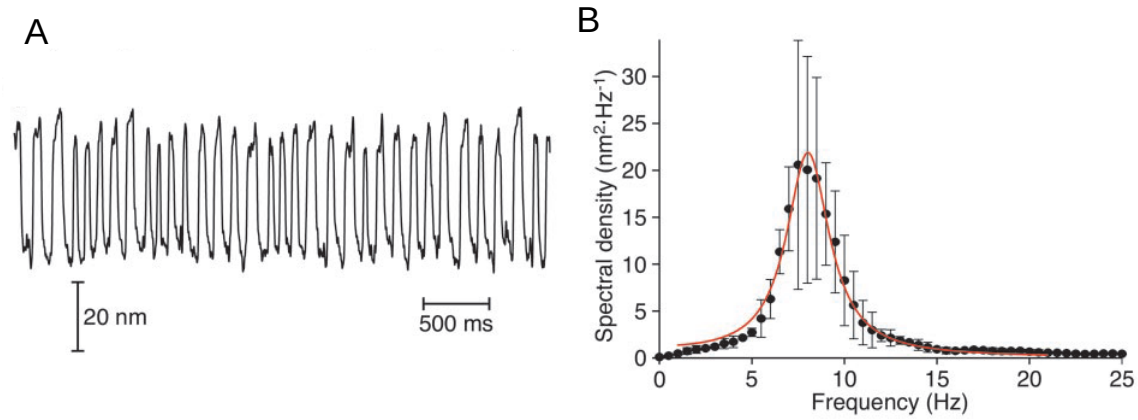


Figure 1.4: Spontaneous activity of hair bundle. (A) Time trace of the hair bundle position. (B) Power spectral density calculated for the trace in A. Modified from [5].

Experimental studies showed that upon positive deflections of the hair bundle, the stiffness of the hair bundle - the slope of the force versus displacement relationship in (Fig. 1.5, A)- behaves linearly, except for a narrow range where the stiffness becomes negative, hence the term *negative stiffness*. Negative stiffness is a result of the concerted

opening of the MET channels. Gating compliance – the concerted opening of the MET channels– result in a relaxing displacement of the hair bundle in the same direction as the positive stimulus. As a result, the experienced force is reduced, and a negative stiffness regime appears in the force–displacement relation, as indicated in Figure 1.5–A.

A widely accepted idea to explain the spontaneous activity (Fig. 1.5–C) of the hair bundle is that the interaction between two intrinsic processes occur in the hair bundle: Adaptation mechanisms [73] combined with negative stiffness of the hair bundle [6, 22] (reviewed in [45, 60]). A satisfactory way to explain this is by looking to panels B and C in Fig. 1.5; starting from the black (dashed line) in B, the two green stars represent two stable positions of the hair bundle (defined by the zero force ($F$) condition in the rest state)

$$F = K_s X - Z P_0,$$

where $K_s$ is the combined gating spring stiffness of N stereocilia, and their pivot stiffness; $Z$ is the gating sensitivity of the MET channel, and it is proportional to N, the geometrical aspects of each stereocilium, in addition to the length of the channels' gate (gating swing); $P_0$ is the open probability of the MET channels (for review see [74]).

Since the transduction current at the rest state is low but nonzero, the open probability ($P_0$= 0.15 [62]) of the channels is low. Thus, molecular motors try to open the channels, causing the relation (Fig. 1.5–B, black dashed line) to migrate along the green dashed lines toward the left (blue curve). At this stage, the negative green star becomes unstable, as the shift proceed until point 1, and a new stable point appears (point 2). Then the hair bundle deflects to the stable point 2 at which the channels are widely open ($P_0$=1), and adaptation proceeds slowly in the reverse direction, causing the relation to shift toward the right (red curve). Similarly as point 1, point three becomes unstable, and the hair bundle deflects toward the left (point 4 in B and C). A continuous repetition of this cycle result is a sequence of positive and negative excursions that compose the time trace in C [6].

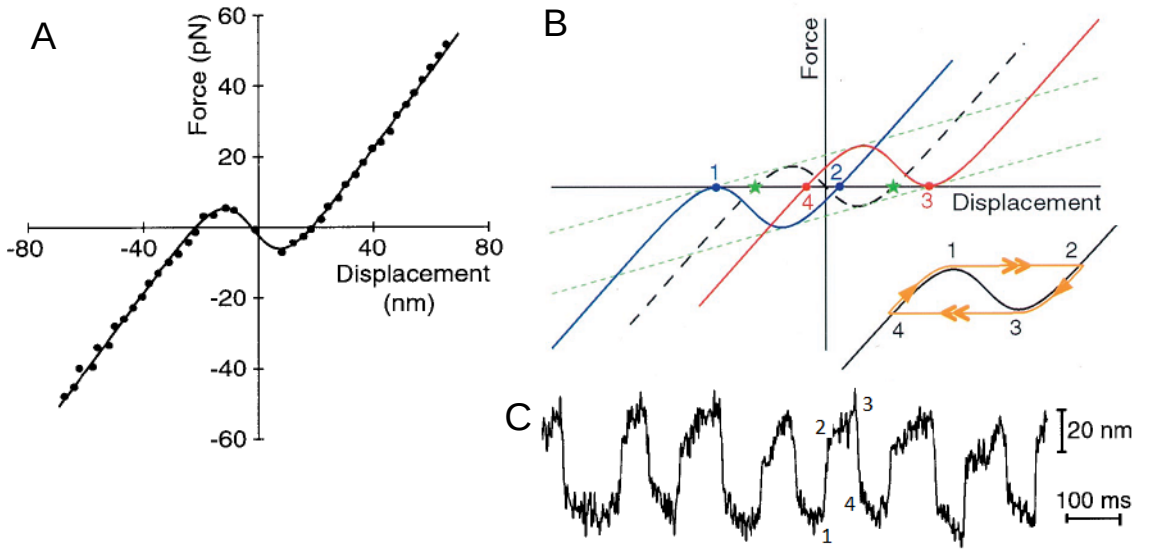


Figure 1.5: Negative stiffness of hair bundle. (A) Force versus displacement of bullfrog sacullar hair cell. (B) Three model generated force versus displacement relationships, each corresponds to the stiffness of the hair bundle for the points numbered in C; the inset indicates the corresponding hair bundle position along the force displacement relationship. (C) Displacement as a function of time for noisy hair bundle performing limit cycle oscillations. Modified from [6].

Bullfrog saccular hair cells respond to a band-limited frequency range as shown in Fig. 1.6–A. The sensitivity curve indicates that the hair bundle is responding maximally to stimuli in a frequency-dependent manner, making the hair bundle selective to certain frequencies. Moreover, hair bundle response varies based on the stimulus magnitude: for a weak stimulus on the order of few picoNewtons, and very large (> 100 pN) stimuli, the bundle responds linearly, while it responds nonlinearly by compressing the stimulus for stimuli between these two extremes. Figure 1.6–B shows that the hair bundle compressive nonlinear response follows a power low with an exponent $(-2/3)$ similar to that reported in cochlear hair cells. Meanwhile, active processes help the hair bundle to amplify its response to weak oscillatory mechanical stimuli [19], making the hair bundle capable of

detecting perturbations on the order of a few angstroms [23, 71] and sound levels up to six orders of magnitude larger than atmospheric pressure [7, 9].

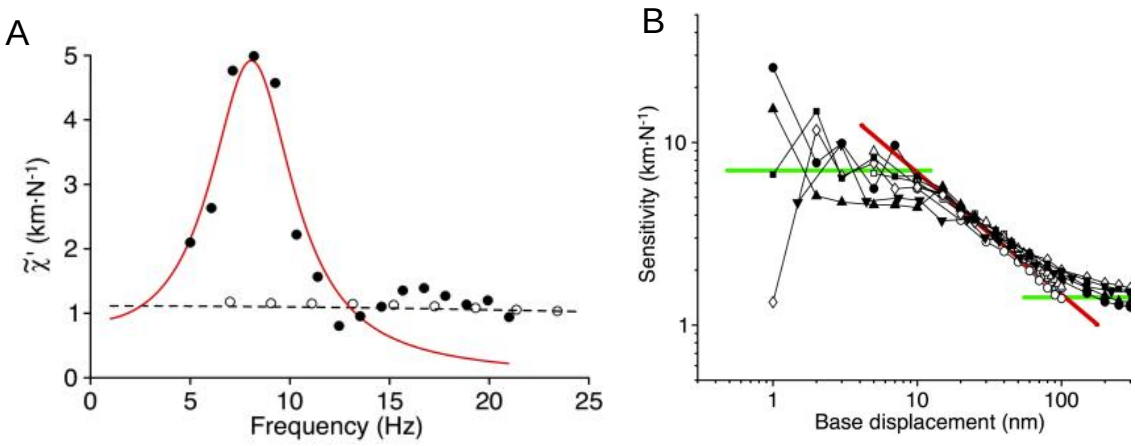


Figure 1.6: Sensitivity curves of bullfrog saccular hair bundle which displayed spontaneous limit cycle noisy oscillations. (A) Sensitivity of oscillatory (black dots) hair bundle, whose natural frequency ~ 8 Hz, as a function of the frequency of 15 nm sinusoidal stimulus. Empty circles correspond to the sensitivity of a hair bundle that showed no oscillations [5]. Red line is a shifted Lorentzian function fitted to the sensitivity data points in black. (B) Sensitivity of a sacculus hair bundle to imposed sinusoidal stimuli, the hair bundle displayed spontaneous activity with frequency ~ 9 Hz [7].

## 1.5 Spontaneous oscillations of the membrane potential

On the basal side of the hair cell is the cell body (*soma*), which has various groups of voltage gated ion channels. The soma is immersed in perilymph, where sodium [60] and calcium are in excess [64]. In the early 1980s, experiments documented electrical resonances, manifested in decaying membrane potential oscillations, in response to current pulses. These electrical resonances are suggested to be the source of frequency selectivity of the receptor potential both in turtle cochlear hair cells [75, 76] and bullfrog saccular hair cells [41, 77, 78]. Previous modeling efforts to study electrical resonances [79] suggested that the quality and the frequency of these oscillations vary as a function of the membrane

potential. The frequency of these resonances fall in the range 10–250 Hz [77,80]. Although electrical resonances are shown to exist in the lower vertebrates and birds, they are rare for mammalian hair cells (for review see [81]). Nevertheless, recent recordings from immature rat vestibular hair cells showed similar electrical resonances as those in nonmammalian hair cells with frequencies in the range 5-40 Hz [82].

Previous studies attributed the origin of the electrical resonances to the interaction between ionic currents on the basal side. *In vitro* current-isolation techniques documented six dynamically significant currents [10, 83–87]: voltage gated calcium current $I_{Ca}$, mixed sodium and potassium current $I_h$, leak current $I_L$, [$Ca^{2+}$]-regulated potassium currents $I_{BKS,T}$ with its both steady ($I_{BKS}$) and transient components ($I_{BKT}$), the delayed rectifier potassium current $I_{DRK}$, and inward-rectifier potassium current $I_{K1}$. At reference membrane potential of -55 mV, the former three currents ($I_{Ca}$, $I_h$, and $I_L$) are inward depolarizing currents, while the latter three currents ($I_{BKS,T}$, $I_{DRK}$, and $I_{K1}$) are hyperpolarizing outward currents. $I_{Ca}$, $I_{DRK}$,and $I_{BKS,T}$ are activated at depolarized potentials, while $I_{K1}$ and $I_h$ are activated at hyperpolarized potentials [10].

The dynamical state of the membrane potential is dependent on the existent proportion of each current (Fig. 1.8) [10]: oscillatory hair cells have large $I_{Ca}$, $I_{BKT}$, and $I_{DRK}$; while, cells with spiking activity posses large $I_{K1}$ and small but not negligible amount of $I_{BKT}$ and $I_{DRK}$. Moreover, cells reside in equilibrium characterized by large $I_{BKT}$ and lower $I_{K1}$. Experimental observations confirmed that membrane potential acquires similar but less noisy dynamical patterns as those of the hair bundle in addition to bursting activity (c.f. Fig. 1.7–A and B) [10] as a result of the interplay between inward and outward currents.

An experimental investigation carried out by Rutherford and Roberts [10] showed that partial blockade of $I_{BKT}$ alters the frequency and amplitude of oscillations, and reverts nonspiking hair cells to spiking activity. The presence of large depolarization-activated currents stabilize the membrane potential. Large depolarizing activated currents are more

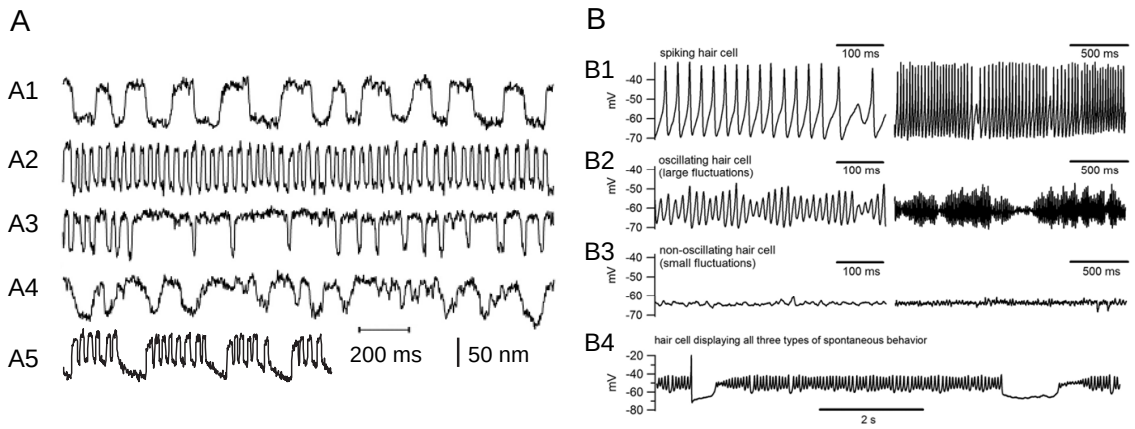


Figure 1.7: *In vitro* spontaneous mechanical [8] (A) and membrane potential (B) oscillations of in bullfrog saccular hair cells. (A1,A2) Slow and fast limit cycle oscillations. (A3) Bistable behavior. (A3) Noisy behavior with no obvious frequency. (A5) Bursting behavior in free standing hair bundle [9]. (B1) Spiking with occasional failure. (B2) Variable amplitude oscillations with no obvious frequency. (B3) No oscillations, or small fluctuations. (B4) Longer recording, shows the spiking behavior of the membrane potential moving abruptly between a depolarized state and a hyperpolarized one. Taken from [10]

expressed in nonoscillatory hair cells, while oscillatory activity is driven by $I_{K1}$, and $I_h$ [86]. However, despite these advances, the role of each individual current in shaping membrane potential oscillations is under debate, meanwhile experimental protocols [88] are shown to alter the quality and frequency of electrical resonances [84].

To investigate the role of these currents in shaping the membrane potential activity, previous studies modelled [86, 87, 89] the ion channels on the basal side using Hodgkin-Huxley type system. The existence of self sustained oscillations (Fig. 1.7), and compressive nonlinearity implies that membrane potential also exhibits characteristics similar to those of a Hopf bifurcation [90]. A dynamical model which incorporated the dynamics of the six ionic currents proved that a Hopf bifurcation does exist [89] using the theory of nonlinear dynamics. Moreover, by varying the strength of $I_{BKT}$ and $I_{K1}$, the membrane potential showed self-sustained oscillations with broad spectrum of oscillatory activity that ranges

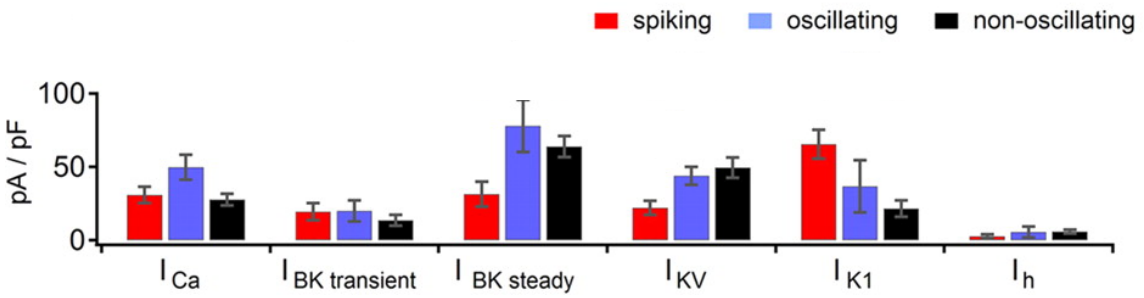


Figure 1.8: Average fitted current densities for three kinds of hair cells under *in vitro* conditions: spiking (red), oscillatory (blue), and non-oscillating hair cells from a preparation of rana pipenies frog's saccular hair cells. Current intensities are measured by stepping the membrane potential from -120 to -30 mv using voltage clamp techniques. Modified from [10]

from periodic, quasi-periodic, spiking, and bursting to chaotic patterns [89] similar to those observed in experiment [10] (Fig. 1.7–B).

Experimental studies showed that the spiking and oscillatory activity of the membrane potential results in periodic activity in afferent neurons [10] as a result of calcium influx into the cell body [91]. Calcium influx mediates bursts of neurotransmitter (most likely glutamate) from the hair cell into the synaptic gap in chick [92] and in bullfrog amphibian papilla [93]. Experimental observations suggest that the frequency of neurotransmitter bursts are within the frequency range of voltage spontaneous oscillations [10, 91]. Thus cell soma membrane potential plays a significant role in afferent spiking activity. Hence, electrical characteristics of the membrane potential are significant in the sensing mechanism.

Correlations between the hair bundle's deflections and the membrane potential are observed experimentally ( reviewed in [14, 18]). A hair bundle deflects in response to somatic electrical stimulation [26, 94]. Moreover, the resting position of the hair bundle, and consequently the adaptation curve shift to the left in response to depolarized membrane potential [95]. These observations were limited to *non–oscillatory* hair cells. In Chapter

3 we will study the effect of fixed membrane potential on the spontaneous and response dynamics of the hair bundle. In addition, recent experimental studies showed that inhibition of somatic ionic currents result in variations in the dynamical behavior of hair bundle innate movements [11]. These observations suggest that the $Ca^{2+}$-dependent processes which are involved in the bundle mechanics are voltage dependent mechanisms [26]. Thus, backward electro–mechanical transduction is evident in sensory hair cells.

Meanwhile the MET current is activated mechanically upon positive deflections [43, 96] of the bundle. The inflow of positive ions depolarizes the cell body [66]. Blocking the MET channels reversibly hyperpolarized the soma membrane potential in chick hair cells [97]. A slight increase in MET conductance results in voltage oscillations, but these oscillations disappear for large MET conductance [87]. Moreover, small changes in the MET current result in spiking activity [10]. Considering all of these observations, both mechano–electrical and reverse transduction serve as bi-directional coupling between mechanical (hair bundle) and electrical (membrane potential) dynamics.

Previous modelling efforts accounted for the experimentally observed dynamics of the hair bundle, and membrane potential [79, 86, 87, 89, 90]. Fewer studies were developed to account for the interaction between hair bundle and membrane potential. Vilfan and Duke suggested a self–tuning mechanism of the hair cell to Andronov–Hopf instability using a linear resonator model for the membrane potential [73]. A linear resonator model for the membrane potential coupled bidirectionally to a stochastic hair bundle was developed by Han and Neiman and they showed that the coherence of the hair bundle oscillations is enhanced by the higher quality of membrane potential oscillations [98]. In addition to these two models, a deterministic model of weakly coupled nonlinear hair bundle and membrane potential showed that the membrane potential may enhance amplification and nonlinear compression in the vicinity of Andronov–Hopf bifurcation [99]. Despite these modeling efforts and experimental observations, the role of membrane potential

dynamics in shaping of spontaneous and response dynamics of the hair cell is still not well understood. In particular, no experimental simultaneous recording of oscillating hair bundles and membrane potential has been reported.

The general goal of this study is to investigate how the interactions of active hair bundle mechanics with variations of membrane potential shape the spontaneous dynamics, overall sensitivity and selectivity of hair cells.

Specific aims are:

- To develop a two compartmental model of hair cells based on the existing experimental and computational studies of the hair bundles mechanics and the membrane potential dynamics of the bullfrog sacculus.

- To model a voltage clamp experiment of the hair bundle, i.e. to study the effect of the membrane potential on deterministic and stochastic dynamics of the hair bundle.

- To fully characterize the deterministic dynamics of the model, including the mechanisms of self-sustained oscillations and the synchronization of the hair bundle mechanical movements with the membrane voltage oscillations.

- To provide a comprehensive description of stochastic dynamics of the hair cell in the presence of thermal fluctuations. This includes calculation of the sensitivity functions and isolation of regions in the parameter space of the model which optimize operational performance of the hair cell sensor.

- To provide a generic description of the role of noise and coupling in optimizing the coherence, sensitivity, and frequency selectivity of coupled unequally noisy oscillators.

This dissertation is organized as follows. Chapter 2 develops the model and describes the methods used in the numerical simulations. Chapter 3 studies the dynamics of

the voltage clamped hair bundle. In Chapter 4, the dynamics of the hair cell as one entity, i.e. the coupled mechanical and electrical compartments is investigated. In this chapter, different dynamical regimes are isolated in the parameter space of experimentally controllable parameters. The effect of bidirectional coupling on spontaneous and response dynamics of the hair cell system is investigated. Chapter 5 is devoted to theoretical study of two coupled unequally noisy oscillators.

# 2 Models and research methods

*Part of the material in this chapter was published in Amro and Neiman (2014)* [12]

## 2.1 Introduction

For modeling purposes, the hair cell was considered as two coupled compartments: the mechanical compartment (hair bundle), and the electrical compartment (soma membrane potential). In the mechanical compartment, the model accounts for the hair bundle displacement, which is a result of the shearing motion of the stereoclia, and the stochastic motion of molecular motors along the actin core. On the basal side, the membrane potential is described using a Hodgkin–Huxley formalism, where ion channel kinetics, and consequently the ionic currents are modeled by using channels' activation and deactivation variables. In this chapter, the details of modeling of both compartments will be introduced. Following the models of each compartment, the two compartments will be coupled bidirectionally.

Figure 2.1 sketches the two-compartment model of the hair cell. The forward coupling is introduced by using the MET current, while the backward coupling is modeled by using the effect of the membrane potential on the calcium concentration near the molecular motors sites in the stereocilium [60, 100], or near the intracellular element that is in series with the tip links [26, 68]. To describe this motion, we establish two coordinates in the plane of bilateral symmetry of the hair bundle. The first coordinate is along the maximal sensitivity axis of the hair bundle (parallel to the otolithic membrane), the other axis is along the actin core in the stereocilium. Symbols in the former coordinate system are given in capital letters ($X$,$X_a$), while those in the latter axis are given by small letters ($x$,$x_a$). The two coordinates are related such that $X_i = x_i/\kappa$, where $\kappa = 0.14$ is a geometrical factor, and it is the same for all stereocilia [50].

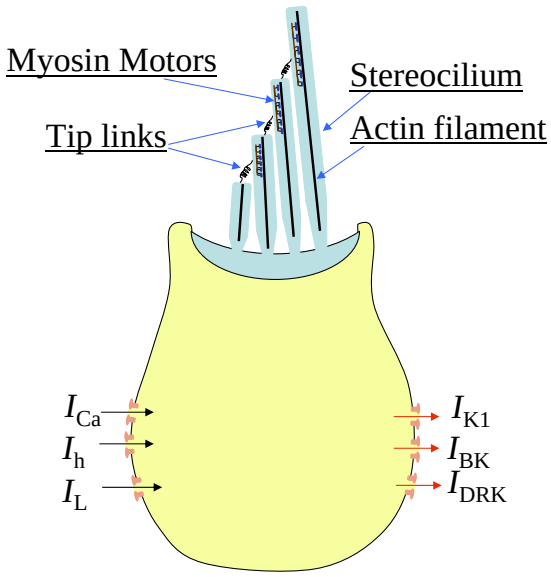


Figure 2.1: Schematic diagram of a hair cell highlighting the main components used in modeling. The hair bundle is composed of an array of stereocilia arranged in rows of increasing height. Neighboring stereocilia are linked by tip links. Mechano-electrical transduction (MET) channels located on stereocilia open or close in response to deflection of the hair bundle which stresses or relaxes the tip links. The myosin molecular motors anchored to the insertion plaque near MET channels contribute to adaptation. The basolateral membrane of the cell contains several types of ion channels. Two sets of ionic currents are shown. First, inward currents include the voltage gated calcium current ($I_{Ca}$), the mixed sodium and potassium h-type current ($I_h$), and the leak current ($I_L$). Second, the outward currents: the [$Ca^{2+}$]-regulated potassium BK current ($I_{BK}$) with its steady $I_{BKS}$ and transient $I_{BKT}$ components, the delayed rectifier potassium current ($I_{DRK}$); and the inward–rectifier potassium current ($I_{K1}$).

## 2.2 Hair bundle modeling

We adopted a model proposed by Jülicher et.al. in 2003 [22]. The hair bundle is treated as a single structure subjected to elastic forces, forces exerted by MET channels, forces exerted by myosin motors, and random forces. This model proved to generate hair bundle dynamics similar to those observed in experiment. Briefly, the model maps the motion of the bundle to the motion of a single stereocilium as the stereocilia move in concert [52]. The hair bundle model in Eq. 2.1 is composed of two stochastic Langevin equations. The

first equation describes the position of hair bundle's tip $X(t)$, while the second equation gives the position of the myosin-1c molecular motors's, $X_a(t)$. Positive displacements of the hair bundle correspond to deflection to the right of the equilibrium position (also to the right in Fig. 2.1). Positive displacements of the molecular motors correspond to downward sliding of these motors along the actin core,

$$\begin{aligned}\lambda\frac{dX}{dt} &= -K_{\mathrm{GS}}(X - X_{\mathrm{a}} - D\,P_{\mathrm{o}}) - K_{\mathrm{SP}}X + F_{\mathrm{ext}}(t) + \epsilon\sqrt{2k_{\mathrm{B}}T\lambda}\eta(t),\\ \lambda_{\mathrm{a}}\frac{dX_{\mathrm{a}}}{dt} &= K_{\mathrm{GS}}(X - X_{\mathrm{a}} - D\,P_{\mathrm{o}}) - F_{\max}(1 - S\,P_{\mathrm{o}}) + \epsilon\sqrt{2k_{\mathrm{B}}T_a\lambda_{\mathrm{a}}}\eta_{\mathrm{a}}(t).\end{aligned} \tag{2.1}$$

In Eq. 2.1, $F_{\mathrm{ext}}(t)$ stands for the external stimulus, $K_{\mathrm{SP}}$=0.6 mN/m is the stereocilia pivots stiffness, and $K_{\mathrm{GS}}$= 0.75 mN/m is the combined stiffness of the gating springs and the load. $D$=60.9 nm is the gating swing, which is the distance by which the hair bundle displacement increases upon the opening of a single MET channel. $\lambda$=2.8 $\mu$Ns/m and $\lambda_{\mathrm{a}}$=10.0 $\mu$Ns/m are the drag coefficients of the hair bundle and molecular motors, respectively. The noise terms $\eta(t)$ and $\eta_{\mathrm{a}}(t)$ are two uncorrelated Gaussian white noise sources which represent the Brownian motion of the hair bundle in the viscous endolymph, stochastic opening and closing of ion channels and the stochastic binding and unbinding of the molecular motors along the actin filament [22]. A dimensionless parameter $\epsilon$ controls the noise strength and takes on two values: 0 for the deterministic case, and 1 for full noise strength.

Since the hair bundle oscillations are slower than the MET channel opening and closing dynamics [101], we assume that MET channels equilibrate instantaneously. We use a two-state model of the MET channel in which a channel switches between open and closed sates [102]. An energy favourable closed state separated by nearly $\Delta G = 10k_{\mathrm{B}}T$ from the open state [102]. The open probability of the MET channel can be written as [22],

$$P_{\mathrm{o}}(X, X_{\mathrm{a}}) = \frac{1}{1 + A\,e^{-(X-X_{\mathrm{a}})K_{\mathrm{GS}}D/(Nk_{\mathrm{B}}T)}}, \tag{2.2}$$

with $A = e^{[\Delta G + K_{GS} D^2/(2N)]/(k_B T)}$, where $k_B$ and T=300 K are the Boltzmann's constant and the ambient temperature respectively, $T_a = 1.5T$ is an effective temperature of the motors. $N$=50 is the total number of the MET channels in the hair bundle.

The control parameters of the hair bundle model are $Ca^{2+}$ feedback strength, $S$, and the maximal force, $F_{max}$, generated by the motors when [$Ca^{2+}$] vanishes. Deterministic and stochastic dynamics of the hair bundle model was studied in details in [22, 67, 103].

### 2.3 Membrane potential modeling

The electrical compartment is modeled using a Hodgkin-Huxley type system [89]. It includes six ionic currents (Fig. 2.1) quantified in several experimental studies on bullfrog saccular hair cells [10, 86]. The model for the membrane potential contains 12 differential equations. The six ionic currents that are used in the model are as follows. The inward–rectifier potassium current $I_{K1}$ (K1) has steady state half activation potential $V_{1/2}$=-110 mV, reversal potential $E_k$=-95 mV, and deactivates for potentials positive to $V_0$=-55 mV. The BK current is a $Ca^{2+}$ and voltage regulated potassium current with steady and transient components $I_{KBS,T}$ has $V_{1/2}$=-61.6 mV. The non-inactivating delayed-rectifier potassium current, $I_{DRK}$, has $V_{1/2}$=-48.3 mV. Four inward currents are: voltage-gated $Ca^{2+}$ current $I_{Ca}$, with $V_{1/2}$=-55 mV; cation h-type current, $I_h$, with $V_{1/2}$=-87 mV; leak current, $I_L$ and MET current, $I_{MET}$.

The time evolution of the membrane potential is described by,

$$C_m \frac{dV}{dt} = -I_{K1} - I_{BKS} - I_{BKT} - I_{DRK} - I_h - I_{Ca} - I_L - I_{MET}, \tag{2.3}$$

where $C_m$=10 pF is the membrane capacitance. The equations for each individual current and their time varying activation and deactivation dynamical equations are given below. The dynamics of these currents are assuming an isopotential cell body, and their individual equations are a result of solving the equivalent electrical circuit for these currents. Thus, by measuring the activation and deactivation rates and maximal conductances for each current,

a complete set of equations is established for the dynamics of every current. The equations for the individual currents are the following:

The inward–rectifier current ($I_{K1}$) [86]:

$$
\begin{aligned}
I_{K1} &= g_{K1}\,[0.7\,m_{K1f}(V) + 0.3\,m_{K1s}(V)]\,(V + 95) \\
\tau_{K1f,s}\,\frac{dm_{K1f,s}}{dt} &= m_{K1\infty} - m_{K1f,s} \\
m_{K1\infty} &= [1 + \exp((V + 110)/11)]^{-1} \\
\tau_{K1f} &= 0.7\exp[-(V + 120)/43.8] + 0.04 \\
\tau_{K1s} &= 14.1\exp[-(V + 120)/28] + 0.04,
\end{aligned}
\tag{2.4}
$$

where $g_{K1}$ is the maximum conductance, and used as a control parameter.

Cation h-current ($I_h$) [86]:

$$
\begin{aligned}
I_h &= g_h\left[3m_h^2(1 - m_h) + m_h^3\right](V + 45) \\
\tau_h\,\frac{dm_h}{dt} &= m_{h\infty} - m_h \\
m_{h\infty} &= [1 + \exp((V + 87)/16.7)]^{-1} \\
\tau_h &= 63.7 + 135.7\,\exp\left[-\left(\frac{V + 91.4}{21.2}\right)^2\right],
\end{aligned}
\tag{2.5}
$$

where $g_h = 2.2$ nS is the maximal conductance.

Delayed rectifier current ($I_{DRK}$) [85]:

$$
\begin{aligned}
I_{DRK} &= \mathrm{DRK}\;P_{DRK}\,\frac{VF^2}{RT}\,\frac{0.112 - 0.002\,e^{-FV/RT}}{1 - e^{-FV/RT}}\,m_{DRK}^2 \\
\tau_{DRK}\,\frac{dm_{DRK}}{dt} &= m_{DRK\infty} - m_{DRK} \\
m_{DRK\infty} &= [1 + \exp((V + 48.3)/4.19)]^{-1/2} \\
\tau_{DRK} &= (\alpha_{DRK} + \beta_{DRK})^{-1} \\
\alpha_{DRK} &= \left(3.2\,e^{-V/20.9} + 3\right)^{-1} \\
\beta_{DRK} &= \left(1467\,e^{V/5.96} + 9\right)^{-1},
\end{aligned}
\tag{2.6}
$$

where $P_{\mathrm{DRK}}$=2.4×10$^{-14}$ L/s is the maximum permeability, $F$ and $R$ are the Faraday and the universal gas constants respectively.

Voltage gated $Ca^{2+}$ current ($I_{\mathrm{Ca}}$) [85]:

$$
\begin{aligned}
I_{\mathrm{Ca}} &= g_{\mathrm{Ca}} m_{\mathrm{Ca}}^3 (V - 42.5) \\
\tau_{\mathrm{Ca}} \frac{dm_{\mathrm{Ca}}}{dt} &= m_{\mathrm{Ca}\infty} - m_{\mathrm{Ca}} \\
m_{\mathrm{Ca}\infty} &= \left[1 + \exp\left(-(V + 55)/12.2\right)\right]^{-1} \\
\tau_{\mathrm{Ca}} &= 0.046 + 0.325 \exp\left[-\left(\frac{V + 77}{51.67}\right)^2\right],
\end{aligned}
\tag{2.7}
$$

where $g_{\mathrm{Ca}}$ = 1.2 nS.

The $Ca^{2+}$ activated potassium current (BK) has a steady (BKS) and a transient (BKT) components [86]:

$$
\begin{aligned}
I_{\mathrm{BKS}} &= b\, P_{\mathrm{BKS}} \frac{VF^2}{RT} \frac{0.112 - 0.002\, e^{-FV/RT}}{1 - e^{-FV/RT}} (O_2 + O_3) \\
I_{\mathrm{BKT}} &= b\, P_{\mathrm{BKT}} \frac{VF^2}{RT} \frac{0.112 - 0.002\, e^{-FV/RT}}{1 - e^{-FV/RT}} (O_2 + O_3)\, h_{\mathrm{BKT}},
\end{aligned}
\tag{2.8}
$$

where $P_{\mathrm{BKS}}$=2×10$^{-13}$ L/s, and $P_{\mathrm{BKT}}$=14×10$^{-13}$ L/s are the BK currents respective maximum permeabilities. Dimensionless parameter $b$ was used to control the strength of BK currents. $I_{\mathrm{BKS}}$ has an additional inactivation gate, whose dynamics are described by [86]

$$
\begin{aligned}
\tau_{\mathrm{BKT}} \frac{dh_{\mathrm{BKT}}}{dt} &= h_{\mathrm{BKT}\infty} - h_{\mathrm{BKT}} \\
h_{\mathrm{BKT}\infty} &= \left[1 + \exp\left((V + 61.6)/3.65\right)\right]^{-1} \\
\tau_{\mathrm{BKT}} &= 2.1 + 9.4 \exp\left[-\left((V + 66.9)/17.7\right)^2\right].
\end{aligned}
\tag{2.9}
$$

The kinetics of BK currents and $[Ca^{2+}]$ dynamics is given by [78]:

$$\begin{aligned}
\frac{dC_1}{dt} &= k_1[Ca^{2+}]C_0 + k_{-2}C_1 - (k_{-1} + k_2[Ca^{2+}])C_1 \\
\frac{dC_2}{dt} &= k_2[Ca^{2+}]C_1 + \alpha_c O_2 - (k_{-2} + \beta_c)C_2 \\
\frac{dO_2}{dt} &= \beta_c C_2 + k_{-3}O_3 - (\alpha_c + k_3[Ca^{2+}])O_2 \\
\frac{dO_3}{dt} &= k_3[Ca^{2+}]O_2 - k_{-3}O_3 \\
\frac{d[Ca^{2+}]}{dt} &= -0.00061 I_{Ca} - 2800[Ca^{2+}],
\end{aligned} \tag{2.10}$$

where $C_0 = 1 - (C_1 + C_2 + O_2 + O_3)$, $k_j = k_{-j}/[k_j(0)e^{-\delta_j \frac{FV}{RT}}]$, $j = 1, 2, 3$; and $\alpha_c = \alpha_c(0)e^{\frac{V}{V_A}}$, $\beta_c = 2500\ s^{-1}$. The rest of the parameters in Eq.(2.10) are the same as in [78]: $k_1(0)$=6 $\mu$M, $k_2(0)$=45 $\mu$M, $k_3(0)$= 20 $\mu$M; $k_{-1}$=300 $s^{-1}$, $k_{-2}$=5000 $s^{-1}$, $k_{-3}$=1500 $s^{-1}$; $\alpha_c(0)$=450 $s^{-1}$, and $V_A$=33 mV. The constants $\delta_1 = \delta_3$=0.2, and $\delta_2$=0.

The leak current ($I_L$) is:

$$I_L = g_L\, V, \tag{2.11}$$

where $g_L = 0.1$ nS.

The mechano-electrical transduction current ($I_{MET}$) is:

$$I_{MET} = g_{MET}\, P_o(X, X_a)\, V, \tag{2.12}$$

where the maximum conductance of MET channels ($g_{MET}$) served as the forward coupling strength and the open probability of MET channels, $P_o(X, X_a)$, is given by Eq.(2.2). In Eqs.(2.11,2.12) the reversal potential of MET and leak currents were set to 0 mV as in [79].

## 2.4 Bidirectional coupling

In Eq.(2.3) the inward mechano-electrical transduction (MET) current, $I_{MET}$,

$$I_{MET} = g_{MET} P_o(X, X_a) V, \tag{2.13}$$

serves as the forward coupling between mechanical and electrical compartments, and the MET conductance, $g_{\mathrm{MET}}$, is the forward coupling strength. Positive deflections of the hair bundle leading to MET channels opening result in depolarization of the cell.

To introduce the backward coupling, we sought to find a relation between the membrane potential and calcium concentration near myosin motor sites. The stall force $F_a$ of the motors is calcium dependent and is approximated by a linear relation, $F_a = F_{\max}[1 - S\,P_{\mathrm{o}}(X, X_{\mathrm{a}})]$, where the calcium feedback strength $S$ is defined as [22, 67],

$$S = -\frac{[Ca^{2+}]_M}{F_{\max}} \frac{dF_a}{d[Ca^{2+}]}, \tag{2.14}$$

such that, $[\mathrm{Ca}^{2+}]_M$ is the $\mathrm{Ca}^{2+}$ concentration near the motor sites. $[\mathrm{Ca}^{2+}]_M$ varies upon changing of membrane potential: hyperpolarized membrane potential (more negative) results in larger inward driving force on $\mathrm{Ca}^{2+}$, leading to a larger concentration of calcium ions near the motor sites, $[\mathrm{Ca}^{2+}]_M$, and consequently to larger values of calcium feedback strength $S$. The dependence of $[\mathrm{Ca}^{2+}]_M$ versus $V$ is calculated using the current Goldman-Hodgkin-Katz equation,

$$[Ca^{2+}]_M = \gamma [Ca^{2+}]_{ext} \frac{\beta V}{1 - e^{\beta V}}, \quad \beta = \frac{2q_e}{k_B T}, \tag{2.15}$$

where $[Ca^{2+}]_{ext}$ is extracellular $\mathrm{Ca}^{2+}$ concentration, $\gamma$ is a dimensionless constant, and $q_e$ is elementary charge. If $S_0$ is the calcium feedback strength at a reference potential, $V_0$, and $[Ca^{2+}]_{M0}$ is $\mathrm{Ca}^{2+}$ concentration at motor sites at $V_0$, then $S$ for any $V$ can be written as

$$S = \frac{[\mathrm{Ca}^{2+}]_M}{[\mathrm{Ca}^{2+}]_{M0}} S_0. \tag{2.16}$$

Then using (2.15) we obtain,

$$S(V) = S_0 \frac{V}{V_0} \frac{1 - e^{\beta V_0}}{1 - e^{\beta V}}.$$

In the following, the reference membrane potential $V_0$ was set at $V_0 = -55$ mV as in [8, 22]. For voltage variations in the range -80 to -30 mV, $S(V)$ in Eq.(2.16) can be linearized

around $V_0$,

$$S(V) = S_0\left[1 + \left(1 - \frac{\beta V_0}{1 - e^{-\beta V_0}}\right)\frac{V - V_0}{V_0}\right],$$

where the pre-factor, $1 - \frac{\beta V_0}{1-e^{-\beta V_0}} = 0.9386$. In order to scale the effect of the membrane potential we introduce a dimensionless parameter $\alpha$ which accounts for the backward coupling strength in our model,

$$S(V) = S_0\left[1 + \alpha\,\frac{V - V_0}{V_0}\right]. \tag{2.17}$$

Hyperpolarization of the cell below the reference potential, $V_0$, leads to an increase of the calcium feedback strength, $S$. This corresponds to an increase of $[Ca^{2+}]_M$ resulting in closure of MET channels. Depolarization of the cell above $V_0$ results in decrease of $S$.

Equations (2.13) and (2.17) provide bidirectional coupling between the hair bundle dynamics (2.1) and the membrane potential (2.3). To conclude, the hair cell system is described by a system of differential equations totalling 14 differential equations. Its two compartments are coupled bidirectionally via Eqs.(2.13) and (2.17). Noise terms are included in the mechanical compartment only (2.1), as experimental studies showed that the MET current (2.13) is responsible for most of fluctuations in saccular hair cells [104].

## 2.5 Stochastic and deterministic methods

Bifurcation analysis of the *deterministic model* was performed using the parameter continuation software package CONTENT [105]. Numerical simulations are carried out using the Runge-Kutta method. All software was written in Fortran. The synchronous dynamics of both compartments were characterised by calculating the relative phase difference between mechanical and electrical oscillation. To do so, sequences of times at which local minima of the hair bundle position, $t_x(j)$, and of the membrane potential, $t_v(k)$, were extracted. The relative phase was then calculated by co-locating the time of the hair bundle local $j$-th minimum within the time interval of two consecutive minima of the

membrane potential,

$$\varphi(j) = \frac{t_x(j) - t_v(k)}{t_v(k+1) - t_v(k)}, \quad t_v(k) < t_x(j) < t_v(k+1). \tag{2.18}$$

A phase map was then constructed, $\varphi(j+1) = \Phi[\varphi(j)]$ (see Fig. 4.4–B in chapter 4). The appearance of a single fixed point in the phase map corresponds to a stable limit cycle in the relative phase series and refers to 1:1 synchronization between mechanical and electrical oscillations. Multiple fixed points correspond to $n : m$ synchronization where the hair bundle performs $n$ oscillations per $m$ cycles of the membrane potential. A sequence of a countable set of points which shows a line corresponds to quasi periodic oscillations in the original system, while scattered points correspond to chaotic behavior in the original system as shown in Fig. 4.5–B.

A quasiperiodic regime corresponding to invariant curves in the phase map and can be distinguished from chaos by calculating the largest Lyapunov exponent (LE) which is 0 for quasiperiodic regimes and has a positive value for chaos. The largest LE was calculated by measuring the rate of divergence (or convergence) of the Euclidean norm between two trajectories of the 12 dimensional system, which have slightly different initial conditions as in [89].

The synchronization index (SI) was used to quantify the degree of synchronization between hair bundle and membrane potential oscillations. The SI was calculated using

$$\rho = \sqrt{\langle \cos(2\pi\varphi)\rangle_t^2 + \langle \sin(2\pi\varphi)\rangle_t^2},$$

where the $\langle ... \rangle_t$ indicates averaging over all points in the map. the SI changes in the interval [0,1]; $\rho = 0$ when mechanical and electrical oscillations are completely out of synchrony, while, $\rho = 1$ represents perfect synchronization.

*In the presence of noise*, the model equations were integrated using the Euler-Maruyama scheme with a fixed time step of $10^{-4}$ s [106]. Spontaneous stochastic dynamics was characterized by the power spectral densities (PSDs) of the hair bundle displacement

and of the membrane potential, calculated from long (600 s) time series using the Welch periodogram method with Hamming window [107]. The quality factor, $Q$, of stochastic oscillations were estimated from the corresponding PSD as $Q = f_p/\Delta f_p$, where $f_p$ is the peak frequency and $\Delta f_p$ is the width of this peak at half maximal power.

*Input – output relations* of the model in response to external stimulus force, $F_{\text{ext}}$ were characterized by two frequency-dependent sensitivity functions: "mechanical", $\chi_M$, and "electrical", $\chi_V$. For a sinusoidal external force,

$$F_{\text{ext}}(t) = F_0 \cos(2\pi f_s t), \tag{2.19}$$

these sensitivity functions are defined as

$$\chi_M(f_s) = |\tilde{X}(f_s)|/F_0, \quad \chi_V(f_s) = |\tilde{V}(f_s)|/F_0, \tag{2.20}$$

where $f_s$ and $F_0$ are the stimulus frequency and amplitude respectively; $|\tilde{X}(f_s)|$ and $|\tilde{V}(f_s)|$ are the magnitudes of the first Fourier harmonic of the time dependent ensemble averages of the hair bundle position, $\langle X(t)\rangle$, and of the membrane potential, $\langle V(t)\rangle$. These time-dependent means were calculated by averaging an ensemble of $10^4$ realizations of $X(t)$ and $V(t)$, over 500 periods of external sinusoidal force. Averaging over this large number of realizations guarantees the smoothness of the output signal in the range of [0 , 30] Hz, thus accurate estimation for the sensitivity for large stimulation frequencies was achieved. This method is used to estimate both linear and nonlinear response as in [7, 22, 108].

In the linear response regime, i.e. for weak stimulus, $F_0 \leq 1$ pN, we used broad-band noise stimulation as in [89]. In this method $F_{\text{ext}} = s(t)$, where $s(t)$ is band-limited Gaussian noise with the variance $\sigma_s^2$ and cutoff frequency, $f_c$. The PSD of the stimulus is $G_{ss}(f) = \sigma_s^2/(2f_c)$ for frequencies within $[0\,, f_c]$ and 0, otherwise. In the following we used $f_c = 200$ Hz. The sensitivity functions for the noisy signal ($\epsilon = 1$) are then defined as [107],

$$\chi_M(f) = \frac{|G_{sX}(f)|}{G_{ss}(f)}, \quad \chi_V(f) = \frac{|G_{sV}(f)|}{G_{ss}(f)}, \tag{2.21}$$

where $G_{sX}(f)$ is the cross-spectral densities between the stimulus and the hair bundle position, $G_{sV}(f)$ is the cross-spectral density between the stimulus and the membrane potential. An obvious advantage of this method is that it allows estimation of sensitivity functions at all frequencies within the stimulus band at once for a given parameter setting, avoiding variation of the frequency of the sinusoidal force [89]. Figure 4.12 in chapter 4 shows that both methods of sensitivity estimation coincide.

In the rest of this thesis, we will use this model and these methods. In Chapter 3 the, hair bundle dynamics under voltage clamp mode will be studied. Methods for calculating the sensitivity of the hair bundle in response to sinusoidal membrane potential variations will be introduced as needed.

# 3 Dynamics of the hair bundle under voltage clamp

## 3.1 Introduction

Voltage clamp, i.e. an experiment when the voltage across membrane of a cell is fixed, is a typical protocol in neurophysiology. Earlier studies on *non-oscillating* hair cells showed static deflections of the hair bundle position in response to stepping changes of command potential [94, 95]. However, no voltage clamp experiments are published for oscillating hair bundles. Such an experiment would be crucial for the investigation of reverse electro-mechanical transduction.

This chapter addresses in detail the effect of voltage clamp on spontaneous and response dynamic of the hair bundle. It investigates whether changes in the membrane potential can reverse the dynamical state of the hair bundle. In particular, how the membrane potential influences the coherence of hair bundle oscillations and how it affects the sensitivity and frequency selectivity of the hair bundle. Understanding the dynamic aspects of the hair bundle under voltage clamp sets the basis for a more detailed study using dynamical membrane potential in Chapter 4.

In the following, the backward coupling strength was set to $\alpha = 1$. Thus the effect of the electro–mechanical coupling is not addressed here. Instead, we postpone this to the next chapter. In addition, we set the membrane potential to a specific value $V = V_c$ in a similar manner to experiments performed on preparations under voltage clamp conditions. The questions are addresses in the following order. First, we study deterministic dynamics in control parameters $S_0$, $F_{max}$, and $V_c$ plane. Second, we investigate the stochastic spontaneous dynamics. Finally, we proceed to quantify the sensitivity of the hair bundle in response to weak sinusoidal voltage stimulus.

## 3.2 Deterministic dynamics under a voltage clamp

The dynamics of the hair bundle are described using the two dimensional stochastic system (Eq. 2.1 in Chapter 2).

$$\begin{aligned}\lambda\frac{dX}{dt} &= -K_{\mathrm{GS}}(X - X_{\mathrm{a}} - D\,P_{\mathrm{o}}) - K_{\mathrm{SP}}X + F_{\mathrm{ext}}(t) + \epsilon\sqrt{2k_{\mathrm{B}}T\lambda}\eta(t),\\ \lambda_{\mathrm{a}}\frac{dX_{\mathrm{a}}}{dt} &= K_{\mathrm{GS}}(X - X_{\mathrm{a}} - D\,P_{\mathrm{o}}) - F_{\mathrm{max}}(1 - S\;P_{\mathrm{o}}) + \epsilon\sqrt{2k_{\mathrm{B}}T\lambda_{\mathrm{a}}}\eta_{\mathrm{a}}(t),\end{aligned} \tag{3.1}$$

where

$$P_{\mathrm{o}}(X, X_{\mathrm{a}}) = \frac{1}{1 + A\,e^{-(X-X_{\mathrm{a}})K_{\mathrm{GS}}D/(Nk_{\mathrm{B}}T)}},$$

such that $A = e^{[\Delta G + K_{\mathrm{GS}}D^2/(2N)]/(k_{\mathrm{B}}T)}$, and

$$S(V) = S_0\left[1 + \alpha\,\frac{V - V_0}{V_0}\right].$$

is given in terms of the membrane potential and the resting membrane potential $V_0 = -55$ mV.

Deterministic dynamics ($\epsilon = 0$) are investigated using the parameter-continuation software package CONTENT [105]. Here, we use the calcium feedback strength at the resting membrane potential ($S_0$) and the maximal force exerted by molecular motors in absence of calcium ($F_{max}$) as control parameters, and study the bifurcation analysis using them. In addition, later in this section, we will use the parameter $V_c$ which stands for the value of the voltage to which the membrane potential is clamped as an additional control parameter.

Figure 3.1 shows bifurcation diagram of the hair bundle on the parameter plane $(F_{max}, S_0)$. The black region corresponds to quiescent state of the system, while color-coded area refers to self-sustained limit cycle oscillations. This oscillation region is isolated by the lines of Andronov–Hopf bifurcations. The effect of command voltage $V_c$ is shown in Fig. 3.2. Notice the similarity of the bifurcations diagrams in Fig. 3.1 and Fig. 3.2–B, albeit the curve in Fig. 3.2–B is flipped. In both Fig. 3.1 and Fig. 3.2–B, the parameter

space is divided into four main regions. An oscillatory region (OSC) isolated by the loop of Andronov–Hopf bifurcation lines from two other quiescent regimes, the region where the MET channels are mostly closed (MC), and that when MET are mostly open (MO).

In the parameter plane of $S_0$ (or $V_c$ in Fig. 3.2–B) and $F_{max}$, two regions can be distinguished within the oscillation region. First, a region characterized by large amplitude low frequency limit cycle oscillations (the region bounded by dashed lines in Fig. 3.1). For fixed value of $F_{max}$, starting with a value of $S_0$ (or $V_c$) below the lower subcritical bifurcation line (or alternatively, small value of $V_c$ ) oscillations arise by increasing $S_0$ ( $V_c$). For a value of $S_0$ ($V_c$) just below the lower dashed line, increasing $S_0$ ($V_c$) results in the coexistence of three states: a stable equilibrium point, stable limit cycle, and an unstable limit cycle, separating previous two stable attractors. Depending on initial conditions, in this narrow parameter region, the hair bundle settles either at equilibrium or on a stable limit cycle. Stable and unstable limit cycles collide and disappear via a saddle-node bifurcation which for the hair bundle model lies very close to the Andronov–Hopf bifurcation line (not shown) [109]. Crossing the subcritical branch of Andronov–Hopf bifurcation line (dotted line in Figs. 3.1, and 3.2) results in a hard excitation of oscillations, i.e. a stable limit cycle is born with a large amplitude.

Second, the solid lines in Figs. 3.1 and 3.2 refers to supercritical Andronov–Hopf bifurcation. Crossing the supercritical line results in a limit cycle whose amplitude grows smoothly proportional to the square root of distance from the bifurcation line and so refers to a soft excitation of oscillations. Note that the amplitude of the oscillations in this region is smaller compared to the subcritical case (Fig. 3.1–B), while their frequencies are higher as shown in Fig. 3.1–A.

Lastly, a region of an equilibrium bistability is marked by BI in Fig. 3.2–B, and in Fig. 3.1–A, B. In this region, the hair bundle possess two stable equilibria corresponding to

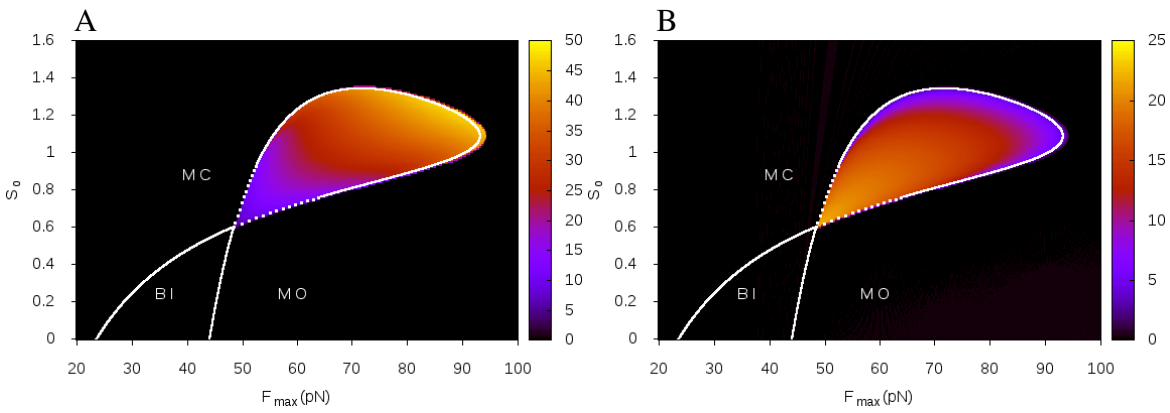


Figure 3.1: Frequency (A) and amplitude (B) maps are generated using the noiseless ($\epsilon = 0$) hair bundle model in the control parameters ($S_0$, and $F_{max}$) plane. Andronov–Hopf bifurcation line (white line) is superimposed on the map. colorbars indicating the values of the frequency (in A), and the amplitude (in B). On both maps, the membrane potential was fixed to $V_c$ =-55 mV, and $\alpha = 1$. Other parameters for the hair bundle are kept the same as in Chapter 2. Indicated on each map are the region where MET channels are mostly closed (MC), MET mostly open (MO), oscillation region (OSC) and a bistability (BI) region.

open and closed states of MET channels. These stable equilibria are separated by a saddle equilibrium.

Now, we turn to the effect of the membrane potential on the oscillation regime in $S_0$, $F_{max}$ plane. We notice that clamping the membrane potential to different levels ($V_c$) affects the oscillation region (Fig. 3.2–A). Stepping $V_c$ from -70 mV to $V_c = -40$ mV extends the oscillation region as shown in Fig. 3.2–A (blue curve versus the red curve). Membrane potential works as a driving force on the calcium ions: the lower the membrane potential the higher the inward (into the stereocila) driving force, hence, higher calcium influx into the stereocilia through the MET channel. Thus, for increasing membrane potential, molecular motors doesn't get enough calcium to stop their motion. In other words, at higher potential, higher values of the calcium feedback ($S_0$) are required to stop the active motion of molecular motors given the membrane potential $V_c$. This explains the expansion of the oscillation regime along the vertical axis ($S_0$) in Fig. 3.2–A. Similar reasoning can be put forward for the expansion along the $F_{max}$ axis.

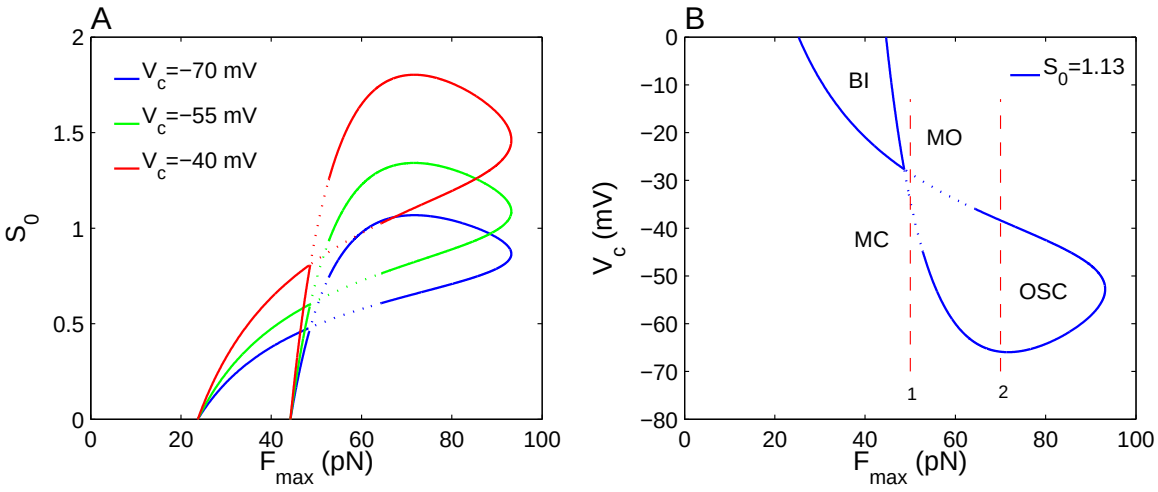


Figure 3.2: Bifurcation diagrams of the hair bundle model, Eq. 3.1. (A) Andronov–Hopf bifurcation lines in the parameter plane of $S_0$ and $F_{max}$ for the indicated values of voltage clamp $V_c$. Dashed lines correspond to the subcritical Hopf bifurcation, while the remaining solid line in the loop stands for the supercritical case. (B) Same as in A, but in the parameter plane of the $V_c$ and $F_{max}$ for fixed $S_0$=1.13. Red dashed lines in B refer to the lines along which $V_c$ was increased. Line 1 and line 2 corresponds to $F_{max}$=50 pN and 70 pN respectively and refer to the two cases studied in the text. Other labels MC, MO, OSC, and BI and other parameters are the same as in Fig. 3.1 above.

Fig. 3.2–B shows this dependence of the oscillation regime on the membrane voltage. In this figure, the command voltage ($V_c$) serves as a control parameter. We notice that the hair bundle possesses an Andronv–Hopf bifurcation in the parameter plane of $V_c$ and $F_{max}$, indicating that the command voltage $V_c$ can be used as a control parameter, i.e. variations of $V_c$ can convert non-oscillating hair bundle to oscillating one and vice versa.

### 3.3 Effect of the membrane potential on spontaneous stochastic dynamics

Hair bundle oscillations are inherently noisy [22]. Noise may excite oscillations outside the deterministic oscillation region. On the other hand, noise leads to fluctuations of amplitude and phase of oscillations when the parameters of a system are within deterministic oscillation region. In this section we turn on the noise terms in Eq. 3.1, $\epsilon = 1$, and study effects of the command voltage on spontaneous stochastic dynamics.

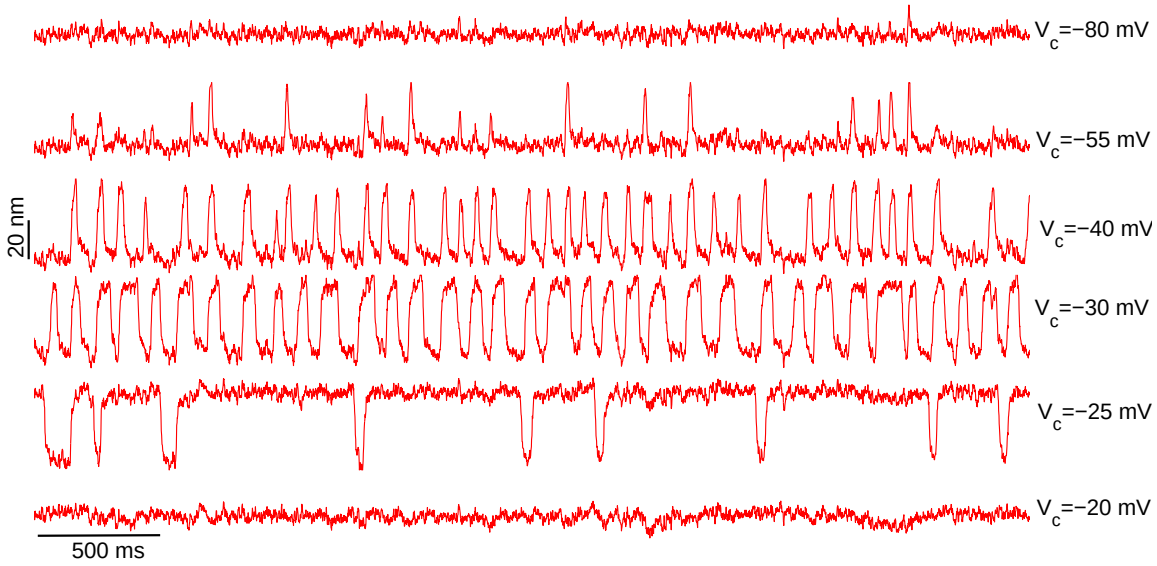


Figure 3.3: Time trace for a hair bundle for which the maximal stall force of the motors, $F_{max}$= 50 pN and chosen such that by stepping the command potential $V_c$, the event of crossing the Andronov–Hopf bifurcation line in the subcritical region takes place. $S_0$=1.13 is kept fixed for this graph. Other parameters are the same as in Fig. 3.1.

Figs. 3.3 and 3.4 show the change in amplitude and frequency of the hair bundle oscillation for increasing values of the command potential. Note the similarity between these oscillation and experimental recordings in Fig. 1.7–A in Chapter 1. Here, we notice from Figs. 3.3 and 3.4 that increasing the membrane potential have drastic effects on the amplitude and the frequency of oscillations. In particular, these changes are more profound in the subcritical case (see Fig. 3.3). In the MC region (Fig. 3.2–B), raising the membrane potential from $V_c = -80$ mV to $-55$ mV, induces large amplitude excursions, which intermittently puts the MET channels in the open state for very short times. Clearly, in the deterministic system the hair bundle is still in the closed state. Thus, these excursions are noise-induced [109]. This was not so obvious in the supercritical regime (Fig. 3.4), as the amplitude of oscillation is small and the frequency is higher than in the subcritical case. Further increase in $V_c$ puts the hair bundle in the OSC regime, and so noise in this regime has a negative consequences on the coherence of the oscillations. Nevertheless,

membrane potential sets the hair bundle to have oscillations with well observed period (Fig. 3.4 for $V_c$=-55, -50 mV, and Fig. 3.3 for $V_c$=-40,-30 mV). For more depolarized membrane potential the hair bundle switches to the quiescent state with large excursions, albeit, those for $F_{max}$ = 50 pN are less frequent and with larger magnitudes. For even larger $V_c$ values the hair bundle settles to the quiescent state, where the channels fluctuate around the open state.

In agreement with previous experimental observations on non-oscillating hair bundles, changes in the membrane potential affect the hair bundle position. Furthermore, our results predict the dynamics of oscillating hair bundle in response to a command potential. Quiescent hair bundles start to oscillate by increasing the command potential $V_c$. Further increase of the membrane potential rendered hair bundle oscillations more coherent. For large depolarized membrane potentials, hair bundle moves to the open state, which is marked by crossing the upper line of the Andronov–Hopf bifurcation in the deterministic system. These observations if reconciled with the effect of the membrane potential on the calcium concentration at the molecular motors (as was discussed in the previous section), lead to an intuitive way of predicting the behavior of the hair bundle response to membrane potential variations.

### 3.4 Effect of the membrane potential on sensitivity of the stochastic hair bundle

Earlier experiments on *non-oscillating* hair bundles documented that the hair bundle responds to variations in the membrane potential, and it has a sensitivity of $\approx$ 0.6 nm/mV, the only value that has been reported experimentally so far [94, 95]. In the following, we calculate the sensitivity of oscillating hair bundle to weak voltage stimuli.

The sensitivity of the hair bundle to sinusoidal variation of the membrane potential was calculated in accordance with the methods introduced in Chapter 2, but here the stimulus is different; instead of using mechanical stimulus, a sinusoidal membrane potential stimulus

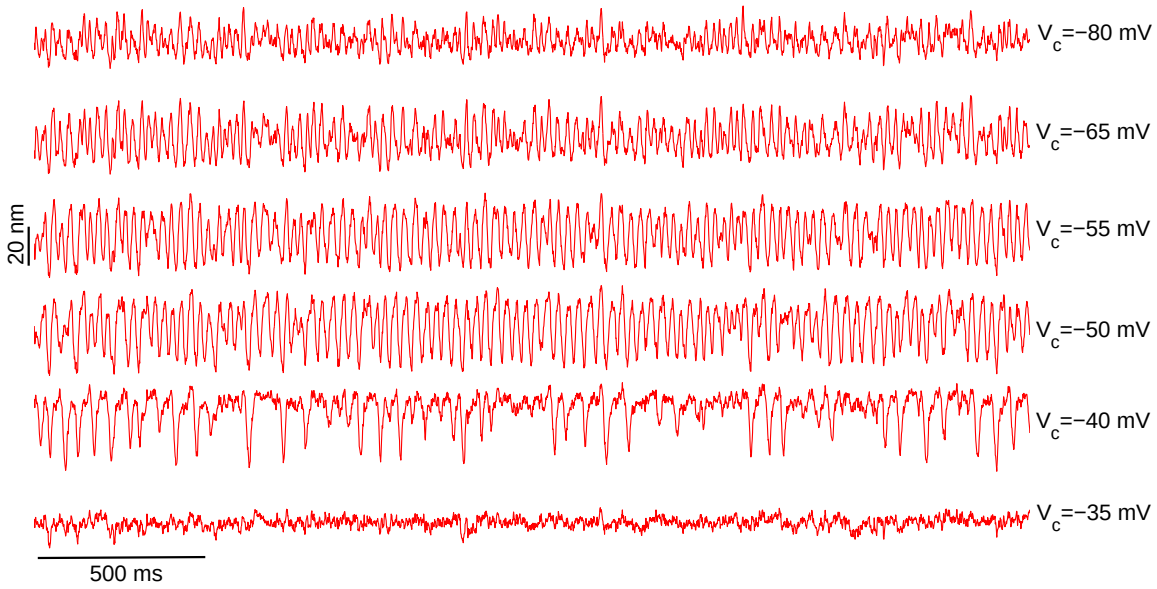


Figure 3.4: Time traces of the hair bundle displacement for increasing values of the command voltage $V_c$. $F_{max}$ = 70 pN is chosen to reflect the changes upon crossing the Andronov–Hopf bifurcation line in the supercritical region. The resting value of the calcium feedback strength $S_0$=1.13 is kept fixed. Other parameter values are the same as in Fig. 3.1.

is used, $V(t) = V_c + \mathsf{v}_s \sin(2\pi f_s)$, where $f_s$ is the stimulus frequency and $\mathsf{v}_s = 5$ mV is the amplitude. Similar to Eq. 2.20 in Chapter 2, the sensitivity of the hair bundle in response to the membrane potential variations is given by,

$$\chi_M(f_s) = |\tilde{X}(f_s)|/\mathsf{v}_s$$

Alternatively, for band-limited Gaussian noise voltage stimulus,

$$V = V_c + \mathsf{v}_s \eta(t)$$

with a standard deviation $\mathsf{v}_s$, and frequency band $[0\,, 80]$ Hz. The sensitivity (response) function is defined using the the auto ($G_{VV}$) and cross spectral ($G_{VX}$) densities of the hair bundle displacement and the stimulus as,

$$\chi_M(f) = \frac{|G_{VX}(f)|}{G_{VV}(f)}.$$

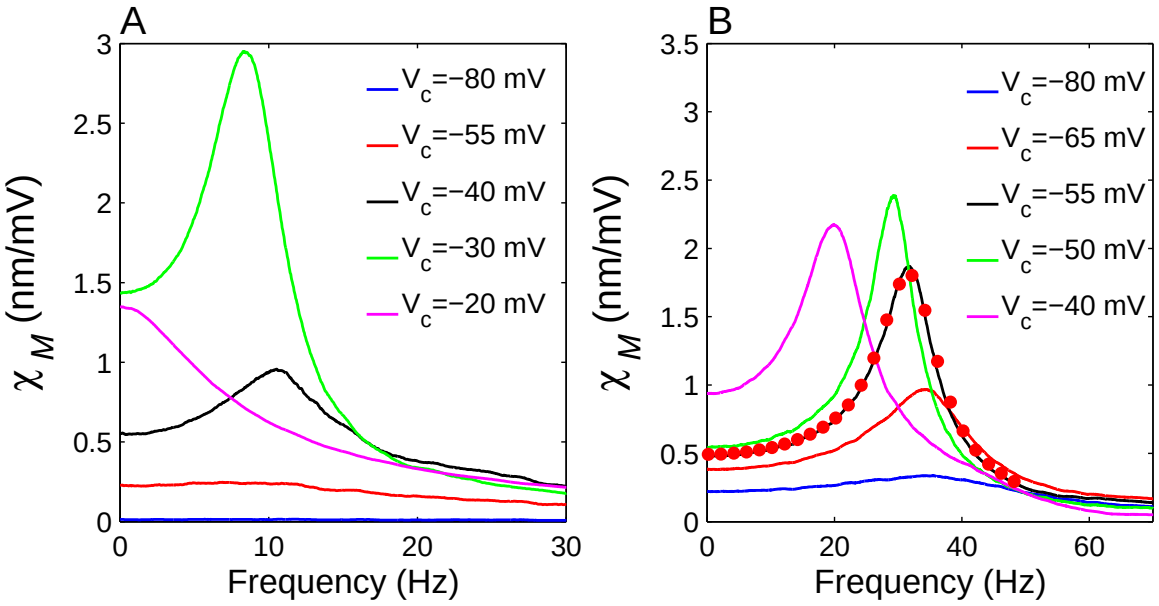


Figure 3.5: Response functions of the hair bundle for increasing voltage clamp values $V_c$. (A) Sensitivity as a function of the driving stimulus frequency ($f_s$), for fixed maximal force of the molecular motors $F_{max}$=50 pN. Calculations are done using white noise stimulus for the membrane potential whose standard deviation $\mathsf{v}_s$ =5 mV. The calculations were done by averaging over an ensemble of $8\times10^3$ time traces, each is 100 seconds in length. (B) Same as in (A) but for $F_{max}$=70 pN. Red dotted curve in B is the sensitivity of the hair bundle for $V_c$ =-55 mV calculated using weak sinusoidal stimulus with amplitude $\mathsf{v}_s$ =5 mV. For both A and B, $S_0$ =1.13, and other parameters are the same as in Fig. 3.1.

The results from the two methods coincide as shown in Fig. 3.5–B (black curve and red dots). Other curves are generated using noise stimulus. The use of band-limited noise stimulus provides faster estimates of the sensitivity, as it gives the response at all frequencies at once, an obvious advantage for experimental implementations.

Figure 3.5 shows that the sensitivity of the hair bundle in response to voltage variations can take values as high as few nm per mV in agreement with previous theoretical studies which treated the membrane potential as a linear resonator [98]. Meanwhile, these values agree with previously reported for *quiescent* hair cells [94]. The sensitivity behaves non–monotonously in response to increasing the DC component $V_c$ of the stimulus. In

addition, the width of the response curves also showed the same trend. These observations indicate that membrane potential plays a crucial role in sensitivity and frequency selectivity indicated by the width of the response function peak. Note that while cells which showed noisy oscillations with no obvious frequency responded minimally to voltage stimulus, increasing the DC component ”converts” non–oscillating cells to oscillating, which boosts their sensitivity at their natural frequency. Nevertheless, quiescent hair cells showed significant sensitivity at low frequencies.

Figure 3.5 shows the sensitivity curves for cells located in the subcritical (Fig. 3.5–A) and supercritical paths to Andronov–Hopf bifurcation (Fig. 3.5–B), for different values of the command voltage, $V_c$. We notice that the peak sensitivity (sensitivity at the peak frequency) attains its maximum value for an optimal value of $V_c$. This optimal value also corresponds nearly to the center of the oscillation region in Fig. 3.2–B. This region is characterized by coherent self–sustained oscillations as shown in Fig. 3.4. We notice also that the sensitivity in the subcritical regime is higher than that of supercritical regime for hair cells which showed coherent oscillations (Fig. 3.3 for $V_c$=-30 mV, and Fig. 3.4 for $V_c$=-50 mV).

## 3.5 Conclusions

We have shown that membrane potential plays a significant role, determining the hair bundle dynamics (quiescence vs. oscillations) and its response. Membrane potential can revert non-oscillatory hair cells to oscillatory ones. In particular, the coherence of hair bundle oscillations is enhanced for optimal values of the membrane potential. Selectivity of the hair bundle as well its response to membrane potential variations are maximized for optimal values of the command voltage too. Our results suggests a faster and more accurate way of estimating the hair bundle sensitivity. Most significantly, the use of noisy stimulus

combined with voltage clamp could enable experimentalists to measure the response of the hair bundle in response to voltage variations at all frequencies at once.

In agreement with previous experimental [94] and theoretical [98] studies the values we obtain for the sensitivity fall within the reported range. In particular, experiments done by Denk and Webb [94] on non-oscillating hair bundle showed that hair bundle deflects by $\approx 0.6$ nm in response to 1 mV change in the command potential $V_c$, a value in agreement with the sensitivity we calculated for *quiescent* hair cells. Our results thus provide experimentally testable prediction for a voltage clamp experiments on oscillating hair cells.

Although our calculations in this chapter assumed externally dictated voltage and so no coupling with voltage compartment, it provides strong argument in favor of the significant role that membrane the potential might play in the dynamics of the whole hair cell system.

# 4 Effect of bidirectional coupling on spontaneous and response dynamics of sensory hair cells

*Part of this chapter was published in two papers of Amro and Neiman (2014)* [12,110]

## 4.1 Introduction

In the previous chapter we considered the effect of voltage clamped membrane potential on the dynamical state of the hair bundle. In this chapter the effect of dynamical membrane potential on the hair bundle dynamics is studied. The membrane potential is modeled using a Hodgkin–Huxley type system and coupled bidirectionally with the hair bundle compartment as introduced in Chapter 2. This chapter addresses in details the effect of bidirectional coupling on the extent of the oscillation regime in the plane of two experimentally testable parameters: the maximal conductance of the inward–rectifier potassium channels ($g_{\mathrm{K1}}$), and the the strength of the calcium–activated potassium channels $b_k$. In addition, it explores the effect of bidirectional coupling strengths ($g_{\mathrm{MET}}$, and $\alpha$) on the spontaneous and stochastic dynamics of the hair cell. The effect of coupling on sensitivity and frequency selectivity of the hair cell in response to weak mechanical stimuli is investigated too.

We minimized the number of control parameters in the model by choosing those which result in pronounced change in the dynamics and can be controlled in an experiment. For mechanical compartment, we considered two fixed sets of parameters: (i) $S_0 = 1.13$, $F_{\max} = 55$ pN, at which the hair bundle is at stable equilibrium, but close to the Andronov–Hopf bifurcation [22]; and (ii): $S_0 = 0.66$, $F_{\max} = 50.2$ pN, at which the hair bundle is at a stable limit cycle regime, oscillating at the frequency of 8.5 Hz. Those regimes are observed for the uncoupled hair bundle, when the EMT coupling strength is set to 0, $\alpha = 0$. Experimental studies have documented diverse voltage oscillatory patterns in

bullfrog saccular hair cells which were correlated to distinct proportions of basolateral ion currents [10] (for further details see Chapter 1). For example, large-amplitude oscillating cells are characterized by a larger fraction of K1 and smaller fraction of BK currents. On the contrary, quiescent cells are correlated with a smaller fraction of K1 and larger fraction of BK currents. Furthermore, oscillations in a quiescent cell can be induced by blocking BK currents [10, 86]. Consequently, the parameters $g_{\mathrm{K1}}$ and $b$, which control the strengths of K1 and BK currents were chosen as control parameters for the electrical compartment as in [89]. The experimentally reported range of the MET conductance, $g_{\mathrm{MET}}$, is from 0.08 to 2.48 nS. Furthermore, MET channels can be blocked as in [10]. We therefore used $g_{\mathrm{MET}}$ as another control parameter for the strength of forward mechano-electrical coupling. Finally, a free parameter $\alpha$ was used to scale the backward electro-mechanical coupling.

## 4.2 Results

The results are organized as follows. First, we describe deterministic dynamics of the hair cell system, concentrating on effect of basolateral currents and coupling strengths on onset of oscillations and their synchrony. Second, we study stochastic dynamics of the model when the hair bundle is subjected to fluctuations. Finally, we describe the response of the hair cell to weak mechanical forcing.

### 4.2.1 Deterministic dynamics

In the deterministic case, $\epsilon = 0$ and $F_{\mathrm{ext}} = 0$ in the mechanical compartment, Eq.(2.1). We start with the case of non-oscillating hair bundle. Lines of Andronov–Hopf (AH) bifurcation shown in panel A of Figs. 4.1 and 4.2 isolate oscillation region on the parameter plane ($b$, $g_{\mathrm{K1}}$) of the hair cell system. Within this region both, the hair bundle and the membrane potential, shows oscillations (panels A2,A3 in Fig. 4.1, A1–A3 in Fig. 4.2, and A2 in Fig. 4.3). Although the shape of oscillation region is similar to that of uncoupled

electrical compartment [89], its size changes significantly with variation of the coupling strengths, $\alpha$ and $g_{\mathrm{MET}}$.

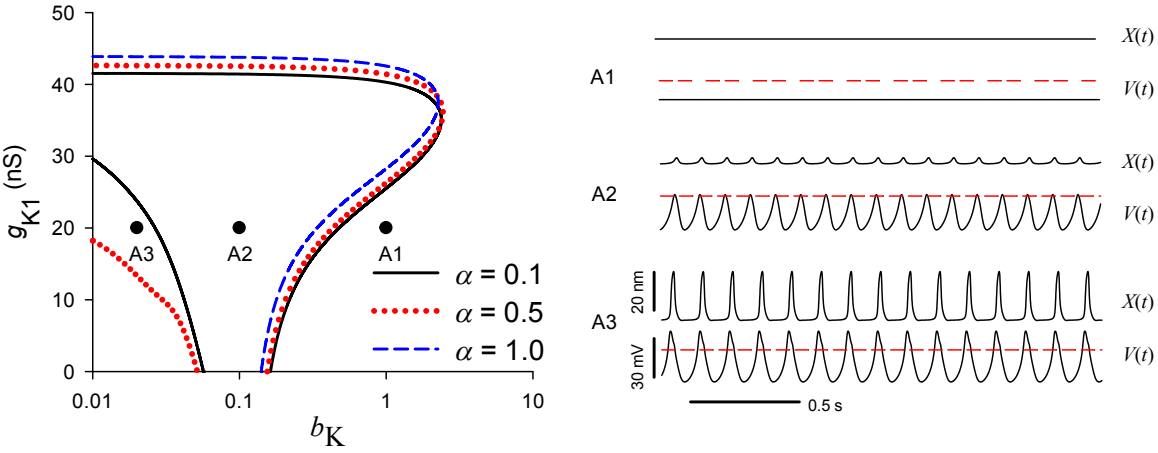


Figure 4.1: Dynamical regimes of the deterministic model ($\epsilon = 0$, in Eq. 2.1 of Chapter 2). Parameters of the mechanical compartment are set to $S_0 = 1.13$, $F_{\mathrm{max}} = 55$ pN, i.e. when uncoupled mechanical compartment is at a stable equilibrium. Left: lines of Andronov–Hopf bifurcation on the parameter plane ($b_{\mathrm{K}}$, $g_{\mathrm{K1}}$) for indicated values of the coupling strength $\alpha$, and fixed $g_{\mathrm{MET}} = 0.5$ nS. Right: Each panel A1–A3 shows the time traces of the hair bundle position $X(t)$ (upper trace) and the membrane potential $V(t)$ (lower trace) corresponding to the filled circles on panels A. Coupling strengths were fixed at $\alpha = 1$, $g_{\mathrm{MET}} = 0.5$ nS for A1–A3. Red dashed line represents the membrane reference potential $V_0$=-55 mV.

An increase of the backward coupling, $\alpha$, results in expansion of oscillation region towards smaller values of BK and K1 currents strength (Fig. 4.1–A). For example, for $\alpha = 0.1$ ( solid black curve in Fig. 4.1A) and small values of $b_{\mathrm{K}}$ and $g_{\mathrm{K1}}$, the cell is at equilibrium with the potential $V$ larger than the reference potential for the hair bundle ($V_0 = -55$ mV). An increase in $\alpha$ (e.g. red curve in Fig. 4.1A) causes a decrease in $[Ca^{2+}]$ near molecular motors in the hair bundle via decrease in the feedback parameter $S$ (Eq. 2.17) in Chapter 2, leading to opening of MET channels and onset of hair bundle oscillations. This in turn activates oscillations in the electrical compartment due to forward

coupling. Amplitude of oscillations becomes large for strong hyperpolarization of the cell (Fig. 4.1–A3), observed for large enough values of $g_{K1}$.

An increase of the forward coupling, $g_{MET}$, leads to an increase of the inward MET current which depolarizes the cell and so larger values of conductances of outward K currents are required to stabilize the cell at an equilibrium. This explains expansion of oscillation region with the increase of the MET conductance, $g_{MET}$ as shown in Fig. 4.1–A.

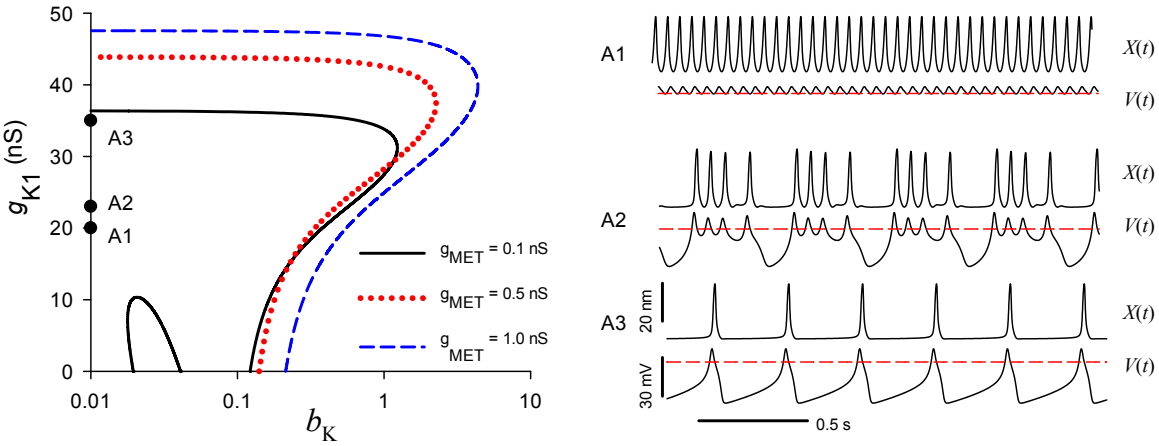


Figure 4.2: Dynamical regimes of the deterministic model. Parameters of the mechanical compartment are the same as in the previous figure, $S_0 = 1.13$, $F_{max} = 55$ pN, i.e. uncoupled mechanical compartment is at a stable equilibrium. Left: lines of Andronov–Hopf bifurcation on the parameter plane ($b_K$, $g_{K1}$) for indicated values of the coupling strength $g_{MET}$ and for $\alpha = 1$. Filled circles correspond to the time traces in A1–A3. Right: Each panel A1–A3 show the hair bundle position $X(t)$ (upper trace) and the membrane potential $V(t)$ (lower trace) as a function of the time for the parameters corresponding to the filled circles on panels A. Coupling strengths were fixed at $\alpha = 1$, $g_{MET} = 0.1$ nS for A1–A3. Red dashed line in A1–A3 represents the membrane reference potential $V_0$=-55 mV.

An important observation from Fig. 4.1 is that mechanical oscillations of the hair bundle are strongly influenced by the basolateral ionic currents. For example, initially quiescent hair bundle at point A1 on Fig. 4.1–A can oscillate (panels A2 and A3) if

BK currents are blocked, which corresponds to a decrease of the parameter $b_{\mathrm{K}}$. Diverse oscillation patterns shown in panels A1 – A3 of Fig. 4.2 are observed for small strength of BK currents (small $b_{\mathrm{K}}$). For the uncoupled electrical compartment these transitions were studied in details in [89]. For fixed values of coupling strengths (Fig. 4.2–A), the increase of the K1 current strength causes the membrane potential to depart from low amplitude oscillation (Fig. 4.2–A1) to a larger amplitude bursting oscillations which have large and slow hyperpolarization excursions due to h-current, $I_{\mathrm{h}}$ (Fig. 4.2–A2) [89]. Because of backward coupling the hair bundle also exhibits bursting patterns. We note, however, that this mechanical bursting differs from recently reported multimodal hair bundle oscillations [9] as in the later work bursting were solely due to hair bundle dynamics, while in our case, it is the result of backward electro-mechanical drive from the membrane potential. Further increase in $g_{\mathrm{K1}}$ results in a sequence of spike–adding bifurcation [89], in which the number of spikes per burst progressively decreases, ultimately leading to slow spiking oscillations (Fig. 4.2–A3) and finally to a hyperpolarized rest potential at which the MET channels are in almost closed state.

The effect of coupling strength on the cell's dynamics is further illustrated in Fig.4.3–A, where both compartments were at stable equilibrium in the absence of coupling ($\alpha = g_{\mathrm{MET}} = 0$). The oscillating region on the parameter plane ($g_{\mathrm{MET}}$, $\alpha$) is bounded by AH bifurcation lines. For chosen parameters, below the lower bifurcation line in Fig.4.3–A, the MET channels are in almost closed state and the rest membrane potential is above the reference potential of the hair bundle, $V > V_0$ (panel A1, Fig.4.3). For a fixed value of $g_{\mathrm{MET}}$ an increase in the backward coupling $\alpha$ results in oscillations of mechanical and consequently electrical compartments (panel A2, Fig.4.3), as explained above. Crossing the upper bifurcation line in Fig.4.3–A corresponds to the transition when MET channels are permanently in open state leading to a large MET current which puts the cell potential in a depolarized rest state (panel A3, Fig.4.3).

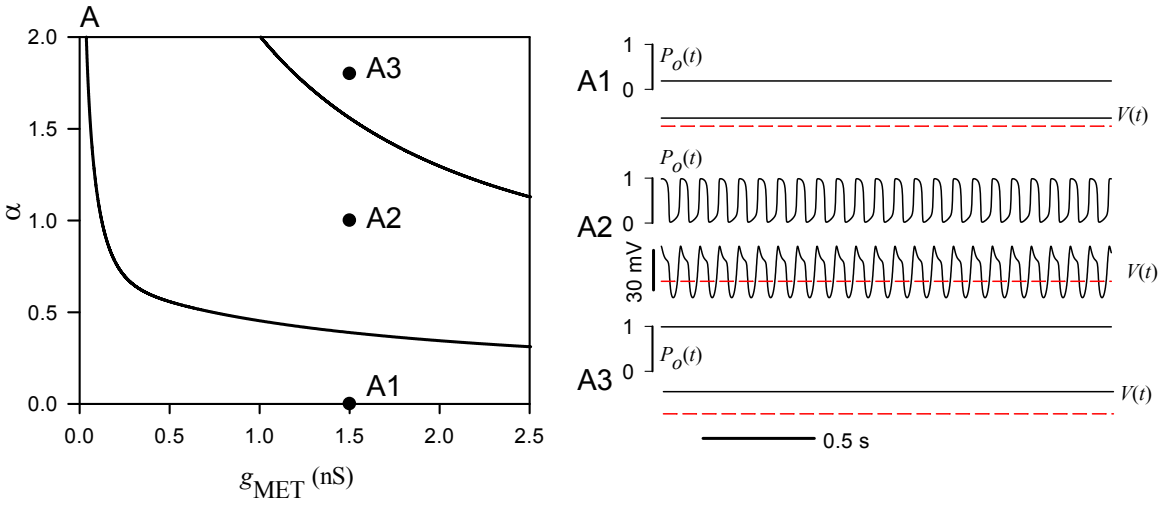


Figure 4.3: Andronov–Hopf bifurcation lines on the parameter plane ($g_{\mathrm{MET}}$, $\alpha$) for $b_{\mathrm{K}}$ = 0.01, $g_{\mathrm{K1}}$ = 1 nS, and $g_{\mathrm{L}}$ = 0. Other parameters are the same as in panels Fig. 4.1. Filled labelled circles correspond to the panels A1–A3. Upper traces in panels A1–A3 show open probability of MET channels, $P_o$, while lower traces corresponds to the membrane potential. Red dashed line represents the membrane reference potential $V_0$=-55 mV.

Next, we consider effects of coupling on mechanical and electrical dynamics when both compartments are oscillating when uncoupled. The parameters of the hair bundle compartment were set at $S_0$ = 0.66 and $F_{\mathrm{max}}$ = 50.18 pN resulting in stable limit cycle oscillations at 8.5 Hz, while the conductances of K1 and BK currents were varied within oscillation region of the uncoupled ($g_{\mathrm{MET}}$ = 0) electrical compartment.

Bidirectional coupling leads to synchronization of self-sustained oscillators [111], which was quantified using phase maps built from time sequences of local extrema in the hair bundle position $X(t)$ and the membrane potential $V(t)$ (see Chapter 2 for details on generating the phase maps). Stable fixed points in such maps indicate phase-locked synchronous dynamics of the model compartments. Quasiperiodic dynamics is reflected by continuous lines in the map (see, e.g. Fig. 4.4–B). The coupling strength resulting in phase and frequency locking depends on frequency detuning of interacting oscillators. Figures 4.4 and 4.5 show results of coupling strengths sweeping for representative examples of

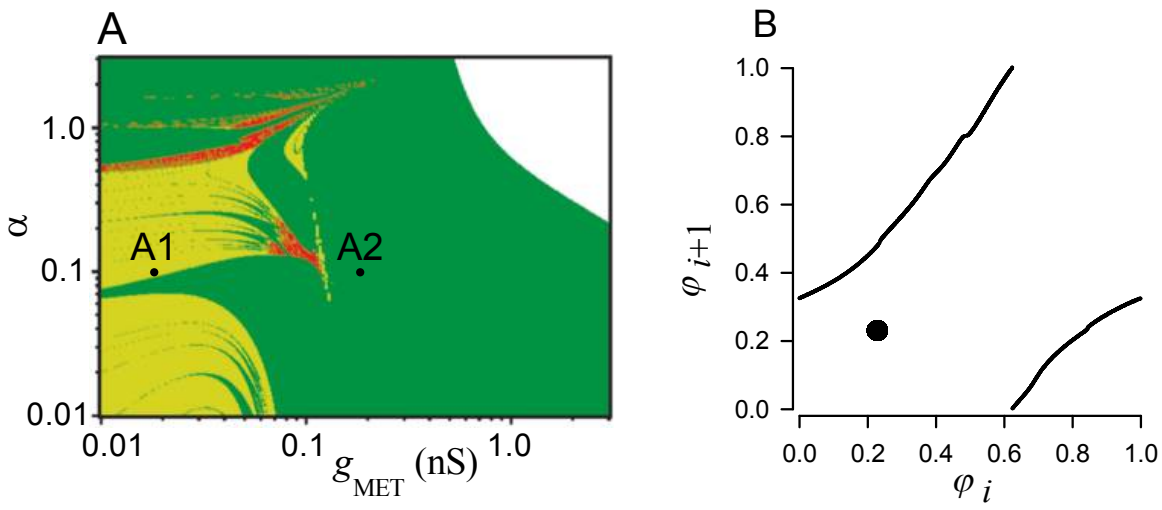


Figure 4.4: Synchronization of the hair cell model compartments. (A) regions of synchronization (the green region), quasiperiodic motion (yellow), chaotic (red) and quiescent (white) regimes on the coupling strengths parameter plane ($g_{\mathrm{MET}}$, $\alpha$). The parameters of the hair bundle compartment are fixed at $S_0 = 0.66$, $F_{\max} = 50.18$ pN. The parameters of electrical compartment, $g_{\mathrm{K1}} = 10$ nS and $b_{\mathrm{K}} = 0.1$, resulted in 9 Hz small-amplitude voltage oscillations in the absence of coupling $g_{\mathrm{MET}} = 0$. Filled black labeled circles on panels A corresponds to phase maps shown on panel B. Filled large circle indicate 1:1 phase locked regime, corresponding to point A2 in panel A. Lines in the phase map on B refers to quasiperiodic motion and corresponds to point A1 in panel A.

weakly and strongly detuned mechanical and electrical compartments. Weakly detuned compartments(Fig. 4.4–A) are phase locked for rather small values of MET conductance, so that for $g_{\mathrm{MET}} > 0.1$ nS, the hair bundle motion and the voltage variations are phase and frequency locked across large range of the backward coupling strength, $\alpha$. Smaller coupling results in multiple synchronization regions separated by regions of quasiperiodic motion (yellow areas in Figure 4.4–A) and small regions of chaos (red areas in Figure 4.4–A).

Fig. 4.5–A exemplifies the case of large detuning when uncoupled electrical compartment is in the regime of large-amplitude low-frequency spiking oscillations resulted by raising K1 current conductance and lowering the BK current conductance. For small values of BK current strength, $b_{\mathrm{K}}$, the uncoupled electrical compartment

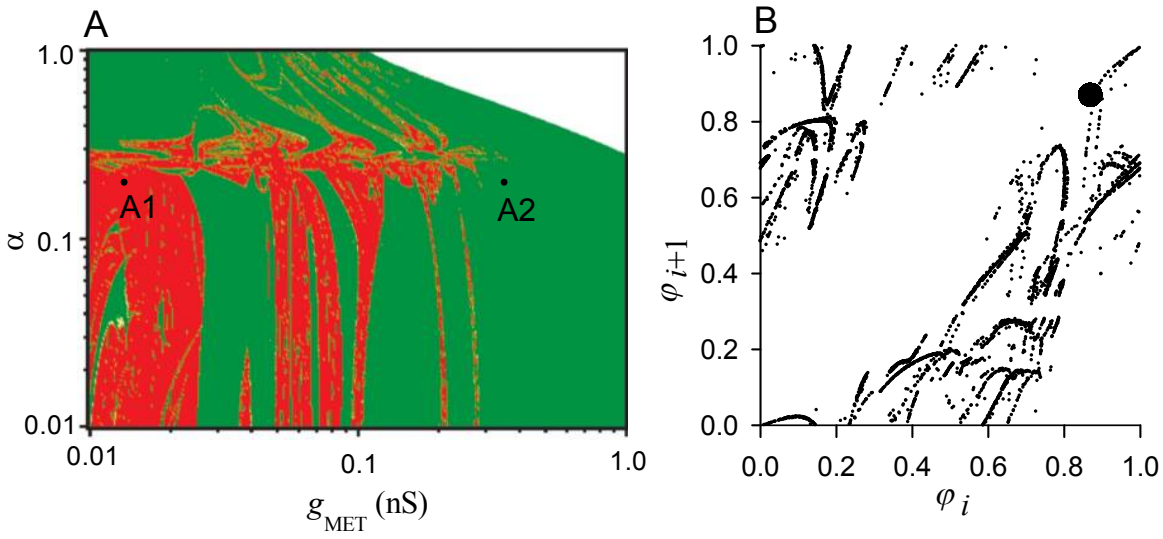


Figure 4.5: Synchronization of detuned hair cell's compartments. A: Regions of synchronization (the green region), quasiperiodic motion (yellow ), chaotic (red) and quiescent (white) on the coupling strengths parameter plane ($g_{\mathrm{MET}}$, $\alpha$). The parameters of the hair bundle compartment are fixed at $S_0 = 0.66$, $F_{\max} = 50.18$ pN. The parameters for the electrical compartment are set to $g_{\mathrm{K1}} = 25$ nS and $b_{\mathrm{K}} = 0.01$, and resulted in large-amplitude spiking oscillations at lower frequency of 4.5 Hz. Filled black labeled circles on panels A correspond to phase maps shown on panel B. B: Phase maps, $\varphi_{i+1} = \Phi(\varphi_i)$, for the marked points on A. Filled large circle indicate 1:1 phase locked regimes, corresponding to points A2 on panels A. Complicated structures on B refers to chaotic oscillations and corresponding to points A1 on panel A.

demonstrates structurally unstable dynamics for increasing values of $g_{\mathrm{K1}}$ with sequences of spike–adding bifurcations in bursting oscillations [89]. Effective backward coupling is strong in this case, resulting in extensive chaotic regions and absence of quasiperiodicity (Fig. 4.5–A), which is consistent with the dynamics of a supercritical circle map [111]. Similar to the case of weak detuning, starting with $g_{\mathrm{MET}} = 0.3$ nS compartments are phase locked across for the entire range of backward coupling strength, $\alpha$. Oscillations region on the coupling strengths parameter plane ($g_{\mathrm{MET}}$, $\alpha$) is bounded by the AH bifurcation line (Figs. 4.4–A, and 4.5–A, upper boundary) which indicates oscillation quenching [111], so that beyond this line both compartments are at rest with MET channels in open state and a depolarized rest membrane potential.

### 4.2.2 Stochastic spontaneous dynamics

In the hair cell model, noise enters into the hair bundle compartment, when the parameter $\epsilon = 1$. Noise can induce hair bundle oscillations even when it is poised in non-oscillating deterministic regimes. This is demonstrated in Fig. 4.6 which should be compared with its deterministic counterpart in Fig. 4.3. In the absence of backward electro-mechanical coupling ($\alpha = 0$) the cell is at stable equilibrium. Noise induces sporadic oscillations of the hair bundle followed by voltage variations due to MET current (Fig. 4.6–A1). These noise-induced oscillations are characterized by a broad peaks in the PSDs of mechanical and electrical compartments (dashed red lines in Fig. 4.6–B,C), notably centered at distinct frequencies.

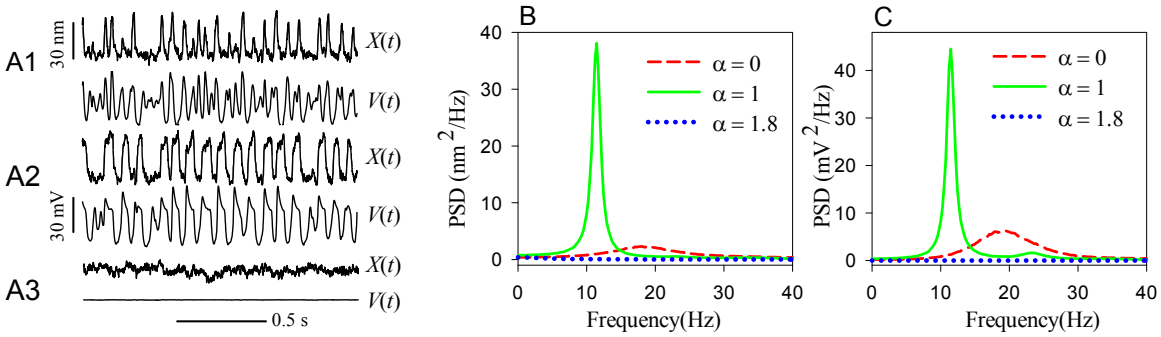


Figure 4.6: Stochastic spontaneous dynamics of initially quiescent hair cell system for different backward coupling strengths. The parameters of the hair bundle compartment are $S_0 = 1.13$, $F_{\max} = 55$ pN; and $b_K = 0.01$, $g_{K1} = 1$ nS, for the electrical compartment; the forward coupling strength, $g_{MET} = 1$ nS. A1–A3: time traces for the hair bundle position, $X(t)$, and the membrane potential, $V(t)$; $\alpha = 0$ in A1, $\alpha = 1$ in A2, and $\alpha = 2.4$ in A3. These parameter values are the same as in Fig. 4.3–A. B,C: power spectral densities (PSD) of the hair bundle position (B) and of the membrane potential (C) versus frequency for the indicated values of the backward coupling strength $\alpha$, in panels A1–A3.

An increase of $\alpha$ moves the system into the oscillation region (see Fig. 4.3–A). As a result, oscillations of both compartments becomes more coherent as seen in time traces of Fig. 4.6–A2. Corresponding PSDs show sharp narrow peaks at the same frequencies

in both compartments (solid green lines in Fig. 4.6–B,C). Further increase of backward coupling strength $\alpha$ beyond oscillation region ceases oscillations (Fig. 4.6–A3,B,C). The quality of oscillations in both compartments is maximal in the middle of the oscillation region bounded by AH bifurcation lines in Fig. 4.3–A.

The above observations are applicable for a wide range of the bidirectional coupling strengths. Figure 4.7–A shows that a region of large amplitude mechanical oscillations extends below the lower boundary of deterministic oscillatory region. Noise-induced

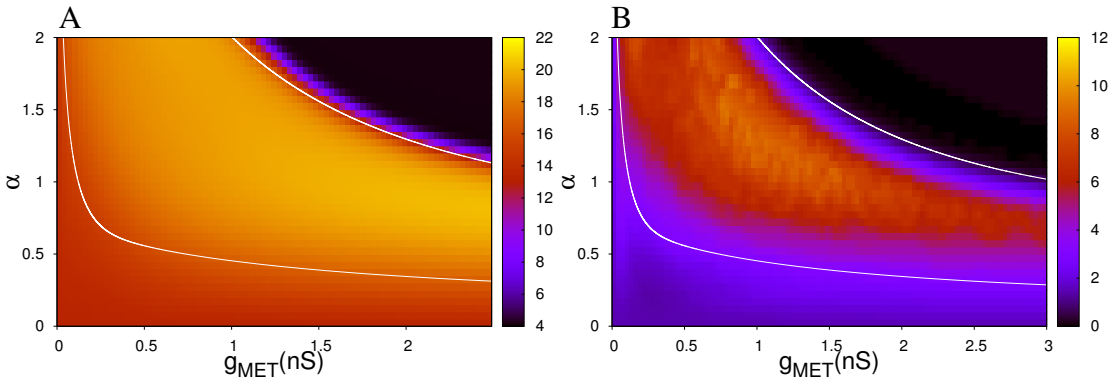


Figure 4.7: Spontaneous dynamics of the hair cell model versus coupling strengths. Both compartments are at equilibrium when uncoupled. A: Standard deviation (SD) of the hair bundle position, the color bar shows SD in nm. B: Quality factor $Q$ of the main peak in the power spectral density of the hair bundle oscillation. On both panels the AH bifurcation lines of the deterministic system are shown by white lines. The parameters are the same as in Fig. 4.3–A.

bundle motion leads to opening of MET channels and since the Ca feedback is relatively weak below the lower AH bifurcation line, adaptation brings the bundle back to the equilibrium position allowing a large-amplitude oscillation. In contrast, above the upper boundary of deterministic oscillatory region large values of the backward coupling $\alpha$ lead to weak adaptation resulting in small-amplitude fluctuations of the hair bundle around the equilibrium with the MET channels in the open state (Fig. 4.3–A3). The coherence of spontaneous oscillations quantified with the quality factor, $Q$ (Fig. 4.7–B), of the main peak

in the PSD of the hair bundle position, shows non-monotonous behavior being maximal at the center of the oscillatory region. In the region below the lower AH line, the dynamics of the system is dominated by noise resulting in noisy oscillations around the equilibrium resulting in broad peaks in PSDs at the natural frequency determined by the imaginary parts of the equilibrium eigenvalues. In the deterministic oscillatory region, both compartments shows synchronous and coherent oscillations with sharp peaks in PSDs (Fig. 4.6–B,C, and Fig. 4.7–B).

The coherence of stochastic oscillations depends crucially on the parameters of electrical compartment, as variation of basolateral ionic currents strength can promote self-sustained oscillations of initially quiescent cells (see Fig. 4.1–A). Figure 4.8 demonstrates that blocking of BK currents may result in a dramatic increase of oscillation coherence. For large BK current strength ($b_{\mathrm{K}} = 1$) the cell was in the quiescent state (traces A1 in Fig. 4.1). Noise induces non-coherent oscillations in both compartments (Fig. 4.8–A1) which are characterized by wide peaks in corresponding PSDs (dashed black lines in Fig. 4.8–B,C). A decrease in $b_{\mathrm{K}}$, corresponds to blocking of BK currents, and leads to large-amplitude coherent oscillations (Fig. 4.8–A2) reflected by large and narrow peaks in the PSDs (solid red lines in Fig. 4.8–B,C).

We now turn to the case when both cell compartments are oscillating at similar natural frequencies when uncoupled, referring to the deterministic case shown in Fig. 4.4–A. With noise added, the mechanical compartment represents a low-quality oscillator, coupled to a noiseless electrical compartment, potentially a high-quality oscillator. According to the theory of coupled self-sustained stochastic oscillators, bidirectional coupling of such distinct oscillators may improve their coherence, if the coupling strength from low-noise to high-noise oscillators is larger than that from high-noise to low-noise oscillator [111, 112]. Backward electro-mechanical coupling from a high-quality somatic oscillator to low quality noisy hair bundle oscillator may then improve overall quality of oscillations.

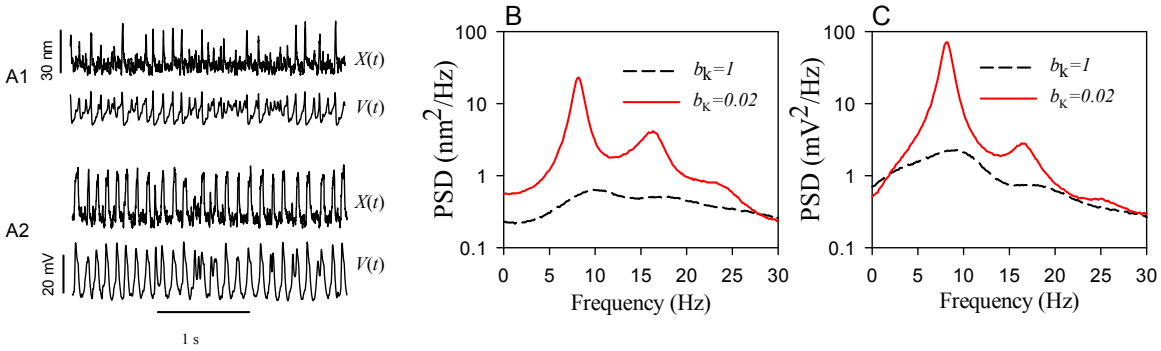


Figure 4.8: Stochastic spontaneous dynamics of the hair cell system for two different strengths of $Ca^{2+}$ controlled K (BK) current. The parameters of the mechanical compartment are $S_0 = 1.13$, $F_{max} = 55$ pN, and $g_{K1} = 1$ nS, for the electrical compartment; the coupling strengths are $g_{MET} = 0.5$ nS, $\alpha = 0.5$. A1–A2: time traces for the hair bundle position, $X(t)$, and the membrane potential, $V(t)$; $b_K = 1$ for A1, $b_K = 0.02$ for A2. B,C: PSDs of the hair bundle position (B) and of the membrane potential (C) versus frequency for the indicated values of the BK current strength, $b_K$, corresponding to panels A1–A2.

In contrast, forward mechano-electrical coupling brings stochasticity from the mechanical compartment to the electrical compartment which could presumably worsen oscillation quality. The example shown in Fig. 4.9 demonstrates this effect. For a fixed small forward

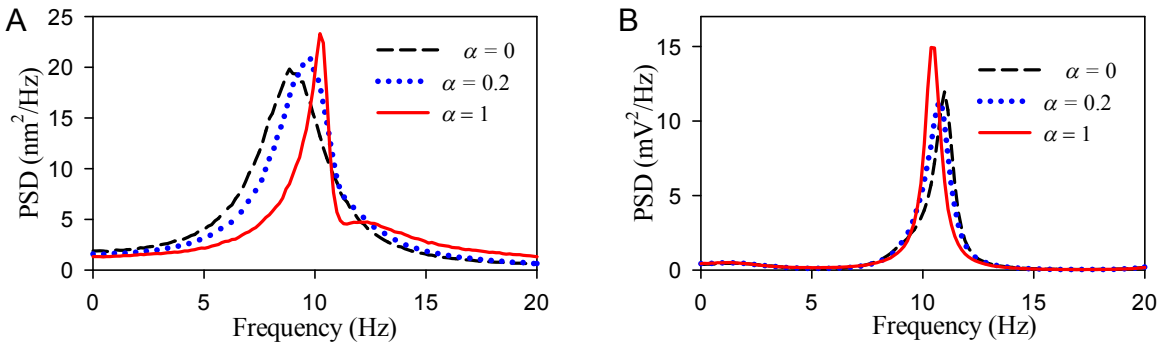


Figure 4.9: Effect of coupling on the coherence of spontaneously oscillating hair cell with closely tuned compartments. The parameters of the mechanical compartment are $S_0 = 0.66$, $F_{max} = 50.18$ pN, and $b_K = 0.1$, $g_{K1} = 10$ nS, for the electrical compartment. A, B: PSDs of the hair bundle position (A) and of the membrane potential (B) for $g_{MET} = 0.05$ nS, and indicated values of backward coupling strength, $\alpha$.

coupling strength, $g_{\mathrm{MET}}$, the increase of backward coupling strength, $\alpha$ leads to narrower peaks in the PSDs (Fig. 4.9–A,B), and hence larger quality of the electrical and mechanical oscillations. This increase in the coherence of the oscillations is quantified by the quality factor which is shown in Fig. 4.10–A,B. The effect becomes less pronounced for larger values of $g_{\mathrm{MET}}$ and disappears for $g_{\mathrm{MET}} = 0.5$ nS. As predicted by the theory developed in Chapter 5, oscillation coherence decreases with the increase of forward coupling, $g_{\mathrm{MET}}$: quality factors of mechanical and electrical oscillations decrease when $g_{\mathrm{MET}}$ increases, as shown in Fig. 4.10–C. We note, that while the backward coupling strength is a rather artificial parameter, the strength of MET current, i.e. the strength of forward coupling can be altered in an experiment by blocking inward MET current as in [11].

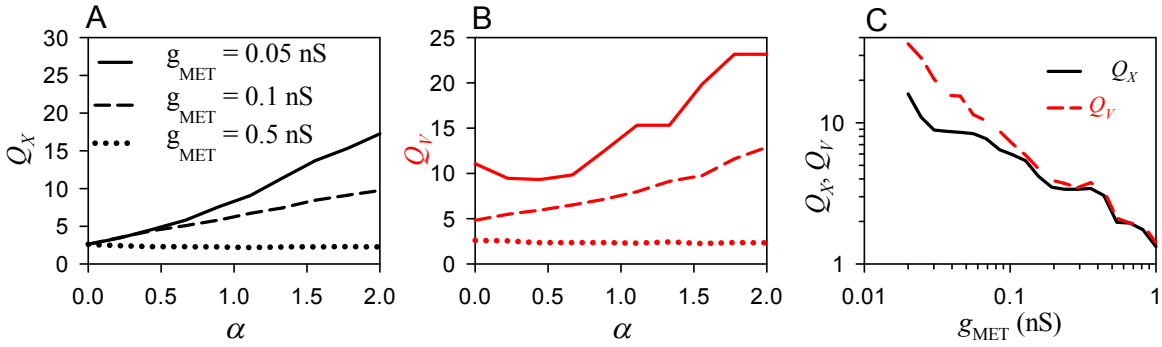


Figure 4.10: Effect of coupling on the quality $Q$ of hair bundle and membrane potential for spontaneously oscillating hair cell with closely tuned compartments when uncoupled. The parameters of the mechanical compartment are $S_0 = 0.66$, $F_{\max} = 50.18$ pN, and for the electrical compartment model are $b_{\mathrm{k}} = 0.1$, $g_{\mathrm{K1}} = 10$ nS. A, B: Quality factor of the hair bundle oscillations ($Q_X$, panel A) and of the membrane potential ($Q_V$, panel B) versus $\alpha$ for the indicated values of forward mechano-electrical coupling strength, $g_{\mathrm{MET}}$. C: Quality factors of mechanical (solid curve) and electrical (dashed curve) oscillations versus $g_{\mathrm{MET}}$ for the fixed $\alpha = 1$.

Finally we consider two highly detuned oscillating compartments referring to Fig. 4.5–A. For weak forward coupling, compartments showed distinct stochastic dynamics: the hair bundle oscillates at 10 Hz, while the membrane potential shows large amplitude, low-

frequency intermittency between spikes and bursts at 4.5 Hz (Fig. 4.11–A1). Fig. 4.11–B shows two distinct peaks in their corresponding PSDs. With increased forward coupling, oscillations in both compartments become synchronous (Fig. 4.11–A2) with frequencies locked at 7.5 Hz, as indicated by PSDs of both compartments, shown in Fig. 4.11–C, peaked at this frequency.

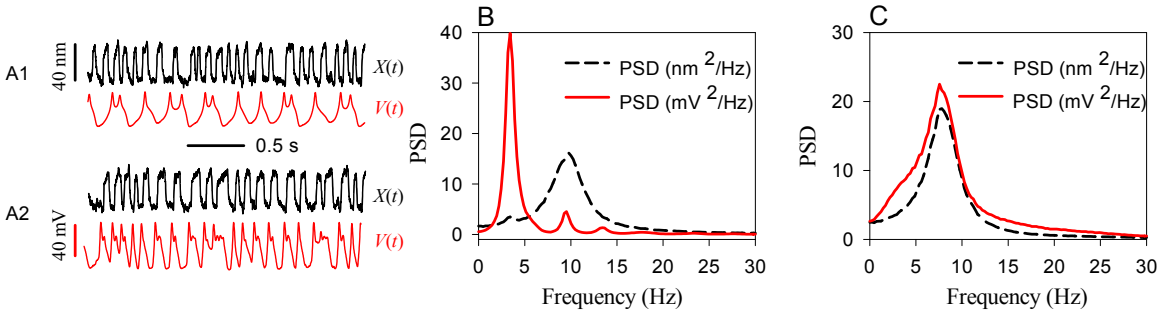


Figure 4.11: Frequency locking of detuned hair cell compartments. The parameters are $S_0 = 0.66$, $F_{\max} = 50.18$ pN, and $b_K = 0.01$, $g_{K1} = 25$ nS; backward coupling strength, $\alpha = 0.2$. A1–A2: time traces for the hair bundle position, $X(t)$ (black lines), and the membrane potential, $V(t)$ (red lines) for small ($g_{MET} = 0.015$ nS , A1) and strong ($g_{MET} = 0.3$ nS, A2) coupling. B, C: PSDs of the hair bundle position (dashed black lines) and of the membrane potential (solid red lines) corresponding to time traces in panels A1 and A2.

### 4.2.3 Response dynamics

Input-output relations of the hair cell system were probed with two types of external mechanical forces: sinusoidal, $F_{ext}(t) = F_0 \sin(2\pi f_s t)$, and broad-band Gaussian noise as described in the methods section in Chapter 2. The sensitivity functions estimated for weak mechanical stimuli were peaked at the natural frequencies of the cell's compartments. Fig. 4.12 shows representative example of sensitivity functions for the case when both deterministic compartments were not oscillating when uncoupled (c.f. Fig. 4.6 for spontaneous dynamics). With no backward coupling, $\alpha = 0$, the sensitivity functions are broad, centred at distinct frequencies (Fig. 4.12–A,B). Transition to deterministic

oscillating for $\alpha = 1$ is characterized by higher and sharper sensitivity functions, peaked at the same frequency. Further increase of backward coupling strength, moves the system closer to the upper bound of the oscillation region (Fig. 4.3–A), thus decreases the sensitivity of both compartments (Fig. 4.13). Similar behavior of the sensitivity is observed for varying forward coupling, $g_{\mathrm{MET}}$, and fixed $\alpha$. Sensitivity over the whole frequency domain is maximal for intermediate values of coupling strengths in the middle of oscillation region in Fig. 4.13. Approaching to the AH bifurcation lines turns the system more susceptible to internal noise, which worsen its sensitivity to external mechanical force.

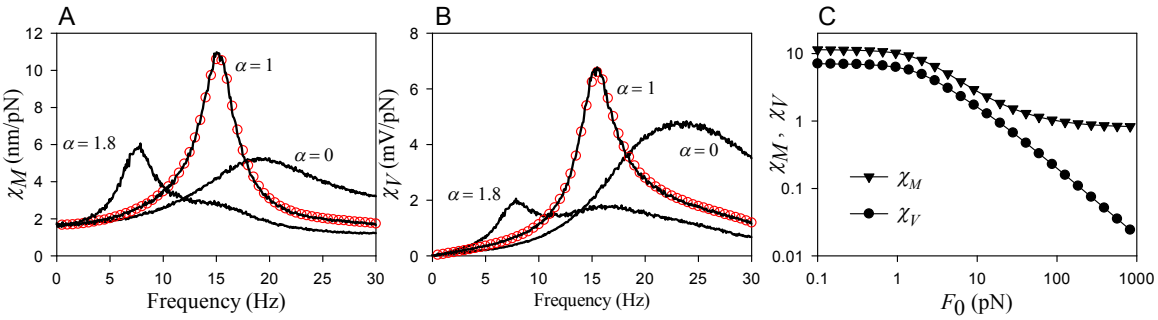


Figure 4.12: Sensitivity functions of the hair cell system for different backward coupling strengths. The parameters of the hair cell compartments are $S_0 = 1.13$, $F_{\mathrm{max}} = 55$ pN; $b_{\mathrm{K}}$=0.01, $g_{\mathrm{K1}} = 1$ nS. The forward coupling strength is $g_{\mathrm{MET}}$=1 nS. A,B: Sensitivity of the hair bundle ($\chi_M$, A) and of the membrane potential ($\chi_V$, B) to noise stimulus with the standard deviation, $F_0 = 1$ pN for the indicated values of the backward coupling strength $\alpha$. For comparison, red circles show the sensitivities calculated for sinusoidal external force with the amplitude $F_0 = 0.5$ pN. C: Sensitivity functions for the hair bundle and the membrane potential versus the amplitude of sinusoidal stimulus at the stimulus frequency, $f_s = 15$ Hz for $\alpha = 1$.

Figure 4.13 shows the maximal sensitivities of hair bundle and membrane potential for a wide range of forward and backward coupling strengths ($g_{\mathrm{MET}} \in [0, 1.6]$nS), ($\alpha \in [0, 2]$). For each values of $g_{\mathrm{MET}}$ and $\alpha$, we calculate the sensitivity of the hair bundle and the membrane potential as a function of the frequency of the weak sinusoidal stimulus.

Then we find the global maximum of this curve. This procedure was repeated for all combinations of $\alpha$ and $g_{\mathrm{MET}}$. As a result, we obtain a color–coded map of the maximal sensitivity of the hair bundle (Fig. 4.13–A) and membrane potential (Fig. 4.13–B) in the bidirectional coupling parameter plane. These maps clearly show the existence of optimal coupling strengths at which hair cells with quiescent uncoupled compartments, is most sensitive to periodic perturbations. Note that the hair bundle is most sensitive the region that is bounded by the Andronov–Hopf bifurcation lines, a region that is characterized by coherent electrical and mechanical oscillations (Fig.4.7–B).

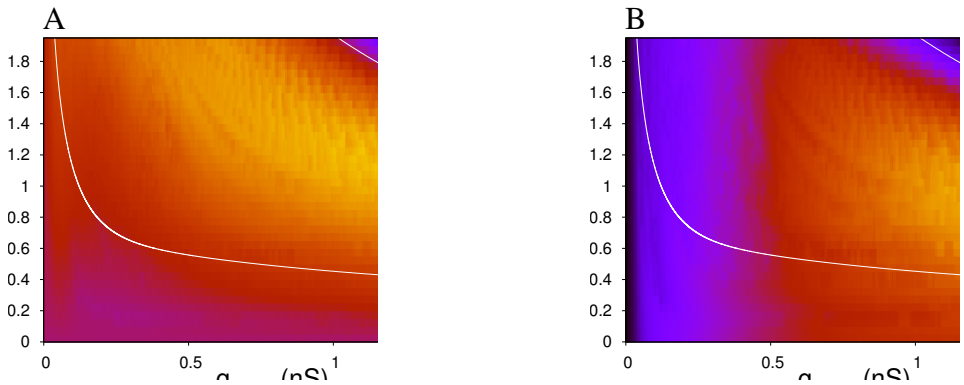


Figure 4.13: Sensitivity maps for the hair bundle (A) and for the membrane potential (B) compartments in response to a weak,$F_0$ = 2 pN, sinusoidal stimulus in bidirectional coupling, ($\alpha$, $g_{\mathrm{MET}}$) plane. The maximal sensitivity is color coded; sensitivity of the hair bundle is measured in nm/pN, while that of the membrane potential in mV/pN. Parameters are the same as F.g 4.3–A.

For large-amplitude stimuli, the response of the hair cell becomes nonlinear. In particular the hair bundle demonstrates the phenomenon of compressive nonlinearity [7, 22, 108], whereby sensitivity is enhanced for weak stimuli and suppressed for strong stimuli. Fig. 4.12–C demonstrates that the compressive nonlinearity is preserved for the hair cell system with coupled mechanical and electrical compartments. In particular, the hair bundle sensitivity shows qualitatively the same dependence versus the stimulus

amplitude as reported before for the hair cell model with *fixed* membrane potential [22]: the response is linear for weak, $F_0 < 1$ pN, and very large, $F_0 > 100$ pN, stimulus amplitude and is nonlinear for intermediate values. The sensitivity of electrical compartment does not saturate for large $F_0$ and the response continues to be nonlinear.

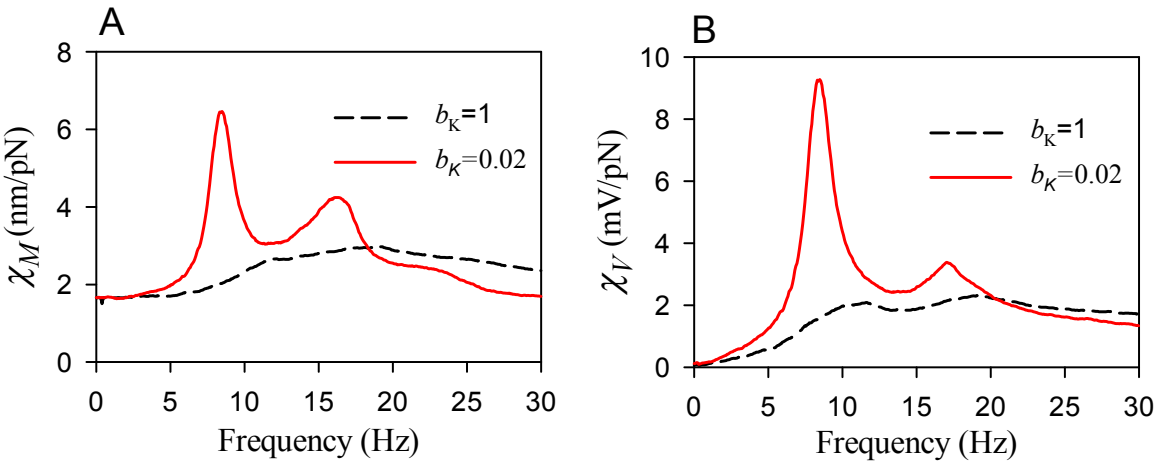


Figure 4.14: Sensitivity functions of the hair cell system versus frequency for two different BK current strengths. The parameters are the same as in Fig. 4.8, except that external broad-band Gaussian noise stimulus with the standard deviation $F_0 = 1$ pN is applied to the mechanical compartment. A: Sensitivity function of the hair bundle, $\chi_M$. B: Sensitivity function of the somatic potential, $\chi_V$.

Variations of basolateral ionic current strength affect significantly the response dynamics of the hair cell. Figure 4.14 shows the sensitivity functions of a cell which was initially non-oscillating (c.f. with Fig. 4.8). For relatively strong BK currents ($b_K = 1$) when spontaneous activity of the cell is solely due to noise-induced oscillations of the hair bundle, the sensitivities of both compartments attain low values and is characterized by broad frequency distribution (dashed black lines in Fig. 4.14). Suppressing of BK currents ($b_K = 0.02$) moves the cell into oscillation region, boosting its sensitivity and frequency selectivity, as evidenced by sharp sensitivity functions of both compartments (solid red lines in Fig. 4.14).

Cells with detuned oscillatory mechanical and electrical compartments show a general response trend, exemplified in Fig. 4.15. For a weak coupling, the sensitivity functions showed two main peaks corresponding to natural frequencies of the hair bundle and the membrane potential (green lines in Fig. 4.15–A,B). The increase of forward coupling strength, $g_{\mathrm{MET}}$ leads to frequency locking (c.f. Fig. 4.11), resulting in larger and sharper sensitivity functions (dashed black lines in Fig. 4.15–A,B). Further increase of coupling strength moves the cell out of oscillation region (see Fig. 4.5–A) which results in suppression of the sensitivity function (dotted red lines in Fig. 4.15–A,B). For the somatic potential the maximal sensitivity across the whole frequency band thus become a non-monotonous function of the MET conductance, taking its maximum at intermediate values of $g_{\mathrm{MET}}$, as shown in Fig. 4.15–C. The effect is observed for large enough values of backward coupling strength, $\alpha$. The effect mentioned above is also observed for cells with with closely tuned compartments (Fig. 4.2). We note, that the MET conductance can be altered in an experiment [11], so that this model prediction can be verified in an experiment.

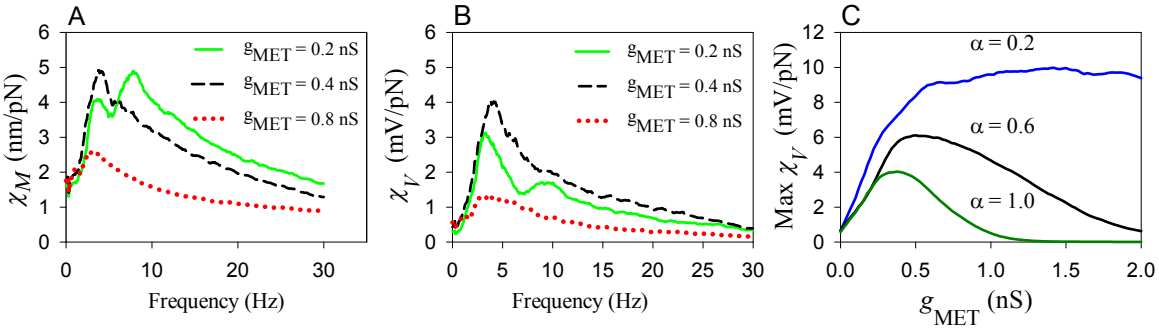


Figure 4.15: (Color online) Effect of coupling strengths on sensitivity functions. The parameters of the cell's compartment, $S_0$, $F_{\mathrm{max}}$, $b_{\mathrm{K}}$ and $g_{\mathrm{K1}}$ are the same as in Fig. 4.11. External broad-band Gaussian noise stimulus with the standard deviation $F_0 = 1$ pN is applied to the mechanical compartment. A,B: Sensitivity functions of the hair bundle, $\chi_M$, and of the somatic potential, $\chi_V$, for $\alpha = 1$ and indicated values of $g_{\mathrm{MET}}$. C: Maximal value of the sensitivity function of somatic potential across the whole frequency band versus $g_{\mathrm{MET}}$ for the indicated values of backward coupling strength, $\alpha$.

We note that for a sensor composed of two unidirectionally coupled linear cascades it is expected that the response at the output of the second cascade would increase with the coupling strength between cascades, as more stimulus power entering to the first cascade will become available for the second cascade [107]. This tendency is indeed observed in the hair cell model for small coupling strengths. However, besides transformed stimulus, the MET current, which is proportional to $g_{\mathrm{MET}}$, brings to the stochastic variability from the noisy hair bundle to the somatic electrical compartment. This variability is then fed back to the mechanical compartment by backward electro-mechanical transduction, which suppresses the sensitivity for strong enough coupling strengths (Fig. 4.15–C).

## 4.3 Conclusions

We studied spontaneous and response dynamics of a hair cell model which incorporates a nonlinear stochastic hair bundle oscillator and a Hodgkin-Huxley type system of basolateral ionic currents. We focused in particular on the role of bidirectional mechano-electrical and electro-mechanical coupling between these two compartments and on the role of voltage dynamics on the emergence of oscillations, their coherence and on amplification properties of the cell.

We have isolated oscillation regions bounded by the lines of Andronov–Hopf bifurcations in the parameter space of the model. Our results show that the hair bundle alters its dynamical state in response to membrane potential variations, in agreement with the results in Chapter 3, albeit in Chapter 3, membrane potential was fixed to different levels of voltage clamps ($V_c$, see Chapter 3). In addition, the dynamical state of the hair bundle changes in response to changes in the forward and backward coupling strengths. We show that changing in the coupling strength may revert non-oscillating hair bundle to oscillatory ones, and vice versa. Furthermore, oscillatory hair cells exhibit spiking, bursting, and chaotic patterns in response to variations of coupling strengths and of changes in the

conductances of basolateral ionic currents. Even for a relatively weak forward coupling ($g_{\mathrm{MET}} > 0.1$ nS) oscillations of hair bundles and membrane potential are synchronized. For large coupling strengths, oscillation quenching takes place, at which mechano-electrical transduction channels are mostly in the open state while the cell is depolarized. Thus, a balance between these coupling strengths is needed in order to keep the cell in self-sustained oscillatory states.

The model has a limitation in that it does not demonstrate a specific bursting patterns observed for free-standing hair bundles [9, 11]. These multimodal oscillations are characterized by large and extremely slow negative excursions of the hair bundle, which disappear when the hair bundle is loaded. Such multimodal dynamics would require an additional slow variable in the hair bundle model, e.g. slow modulation of the gating spring stiffness proposed in Ref. [9]. The hair bundle model which is used here does not include this additional slow variable. Rather, it assumes a stimulation fiber attached to the hair bundle and thus an external mechanical load [22]. Consequently, a bursting patterns generated by the model (Fig. 4.2, panel A2) are solely due to strong backward electro-mechanical coupling, whereby bursting of the membrane potential drives the hair bundle dynamics.

Spontaneous dynamics of the hair cell is inherently noisy mainly due to fluctuations of the hair bundle compartment [104]. In the model stochastic terms were incorporated in the hair bundle compartment which fed fluctuating mechano-electrical transduction current to the electrical compartment. The coherence of mechanical and electrical spontaneous oscillations depends crucially on the coupling strengths and on the conductances of the basolateral ionic currents. In particular the model predicts that for weak forward mechano-electrical coupling (small values of $g_{\mathrm{MET}}$) the coherence of spontaneous oscillations can be enhanced by backward electro-mechanical coupling (Fig. 4.9). Our results indicate that spontaneous noisy oscillations of hair bundles routinely reported in experimental studies

can result from nonlinear interaction of mechanical and electrical compartments of the hair cell. This is supported by a recent experimental study where drastic changes of hair bundle oscillations in response to basolateral ion channel blockage were reported [11]. The model

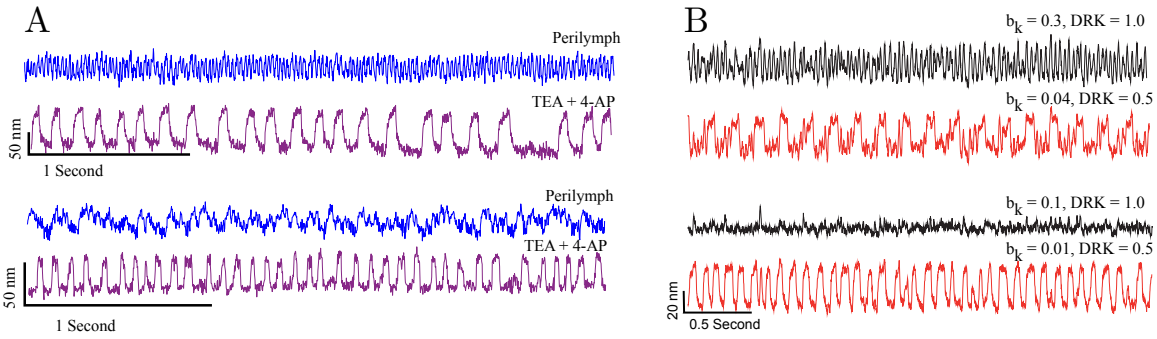


Figure 4.16: Effect of ion channels blockers on spontaneous oscillations of the hair bundle in the model. Experiment (A) versus modeling (B). A: Two sets of experimental time traces of the hair bundle position when the somatic compartment was in regular perilymph (no channel bolckers were added) and after blocking the calcium activated potassium current ($I_{\mathrm{BK}}$) and the delayed rectifier current ($I_{\mathrm{DRK}}$) using specific chemical blockers (TEA and 4-AP). Modified from [11]. B: time traces generated using the model. Black traces show the original dynamics of the hair bundle while red traces show the dynamics after two types of ionic currents $I_{\mathrm{BK}}$, and $I_{\mathrm{DRK}}$ are blocked. The strength of $I_{\mathrm{BK}}$ is controlled by the parameter $b_{\mathrm{K}}$, and $I_{\mathrm{DRK}}$ is controlled by the parameter DRK in Eq.(2.6, Chapter 2). Higher values of these parameters correspond to larger currents. The parameter values for the upper traces in B are: $S_0$=0.9, $F_{\mathrm{max}}$=75 pN, $g_{\mathrm{K1}}$=7.5 nS, $g_{\mathrm{L}}$ = 0, $\alpha$=1.6, $g_{\mathrm{MET}}$=0.1 nS, and for the lower traces in B are: $S_0$=1.4, $F_{\mathrm{max}}$=55 pN, $g_{\mathrm{K1}}$=7.5 nS, $g_{\mathrm{L}}$ = 0, $\alpha$=1.6, $g_{\mathrm{MET}}$=0.1 nS.

shows qualitative agreement with these experimental observations, exemplified in Fig. 4.16. Blocking of calcium activated potassium channels (BK), and delayed rectifier potassium current (DRK) activates large-amplitude low-frequency voltage oscillations, causing high frequency mechanical oscillations to slow down, and increase their amplitude (Fig. 4.16–A). An initially quiescent hair bundle (Fig. 4.16–B) starts oscillating when the cell becomes depolarized upon blockage of BK and DRK ion currents. Alongside these observations, our model shows that blocking of calcium activated potassium channels alone induces

large amplitude coherent oscillations as shown in Fig. 4.8, enhancing the coherence of oscillations, and renders the cell more sensitive and frequency selective (see Fig. 4.14).

The main characteristics of the active hair bundle, such as compressive nonlinearity and frequency selectivity are reproduced by the two compartmental model. Both compartments showed frequency selectivity, sensitivity, and compressive non-linearity for incoming mechanical stimuli with amplitudes greater than 1 pN. However, while the mechanical hair bundle showed saturated response for stimuli greater than 100 pN, the electrical compartment sustained its compressive response for large ($>$ 100 pN) stimuli. An important issue of exponent of nonlinear compression [108] was not studied here. In particular, an interesting question on how the exponent of nonlinear compression depends on the coupling strengths and detuning of the cell compartments will be addressed elsewhere. In this respect, we refer to theoretical study [99], where this question was addressed in a deterministic hair cell model for the case of weak coupling.

Noise is the limiting factor of the hair bundle sensitivity [22, 108]. We find that the sensitivity to weak stimuli can be maximized by adjusting the interaction between hair cell compartments. For a cell whose uncoupled compartments are at equilibrium the sensitivity can be maximized in the middle of oscillatory region bounded by the lines of an Andronov–Hopf bifurcation (Figs. 4.3–A and 4.12). That is, variation of both the forward and backward coupling can maximize the sensitivity. However, for a cell with oscillating uncoupled compartments the maximal sensitivity depends non-monotonically on the MET conductance in the presence of backward electro-mechanical coupling (see e.g. Fig. 4.15), while the reverse electro-mechanical transduction degrades the sensitivity. This shows that stochastic hair bundle oscillations limits the sensitivity of the hair cell.

# 5 Dynamics of two coupled stochastic phase oscillators

*Part of this chapter was published in Amro et al. (2015)* [113]

## 5.1 Introduction

In Chapter 4 we explored the effect of bidirectional coupling on the dynamics of the hair bundle and the membrane potential. Due to the high dimensionality of the model, a numerical approach was followed to investigate the response of those cells for different values of the coupling strengths. The striking effect is the existence of optimal coupling strength which maximizes the sensitivity of the hair cell system to mechanical stimuli. This effect was attributed to the fact that the mechanical oscillator is much more noisy than the electrical oscillator and so the increase of MET conductance (coupling strength), while bringing more signal to the cell, also carries randomness, which betrays the sensitivity and selectivity of the cell. In this chapter we use simple phase models to theoretically study the sensitivity of a two-cascaded amplifier with unequal noise levels in each cascade.

Previous studies suggested that the hair bundle and the basolateral compartments when uncoupled may operate near Andronov–Hopf bifurcation. In particular, biophysical models suggested that the dynamical aspects of the hair bundle are captured using dynamical equations of a system poised near Andronov–Hopf bifurcation [7,22,25,114]. Other studies modeled voltage dynamics with a Hodgkin-Huxley type system which possesses a Hopf instability too [89,90].

For a system operating near critical instability, the generic aspects of its dynamics can be studied in terms of a normal form, therefore, the two systems are said to be topologically equivalent [115]. Motivated with this idea, the computational neuroscience literature is rich with the use of different types of normal forms [116]. Normal forms allow to reduce the dimensionality of the system as well as to carry some analytical calculations in specific cases, albeit, the detailed dynamics of the biophysical model are not preserved. In studying

sensory hair cells, several theoretical studies explored the dynamics of the hair bundle using normal forms of the Andronov–Hopf bifurcation [108, 117]. Recently, Shlomovitz et.al. showed that a wide range of experimental observations of bullfrog saccular hair bundles can be captured with a simple phase equation [118]. Most recently, an array of driven noisy Adler's equations was used to describe the *in vitro* spontaneous activity of hair bundles subjected to mechanical load [119]. The study showed that the signal to noise ratio can be maximized for an optimal noise level, thus demonstrating the phenomenon of stochastic resonance. Application of the normal form theory is not limited to single hair bundle, but also applicable to a group of coupled hair bundles. For instance, frequency discrimination and signal amplifications in addition to hearing loss in mammalian ear can be explained using a set of coupled deterministic phase oscillators [120]. Normal forms were used to study bidirectionally coupled mechanical and electrical *deterministic* hair cell compartments in [99] and showed compressive nonlinearity for large driving as in the detailed biophysical model of Chapter 4.

## 5.2 The model

We start with the so-called Landau-Stuart oscillator, which also serves as the normal form for supercritical Andronov–Hopf bifurcation [111],

$$\dot{Z} = (r + i\omega)Z - |Z|^2 Z, \tag{5.1}$$

where $\omega$ is the natural frequency of the oscillator and $r$ is the bifurcation parameter. For $r < 0$ the oscillator possesses a single stable equilibrium, which undergoes supercritical Andronov–Hopf bifurcation at $r = 0$, and for $r > 0$ the system possesses a stable limit cycle.

To mimic the dynamics of coupled electrical and mechanical compartments we consider two bi-directionally coupled stochastic Landau-Stuart oscillators,

$$\dot{Z}_1 = (r_1 + i\omega_1)Z_1 - |Z_1|^2 Z_1 + \alpha Z_2 + f\, e^{i\omega_s t} + \sqrt{2\mathrm{D}_1}\zeta(t),$$
$$\dot{Z}_2 = (r_2 + i\omega_2)Z_2 - |Z_2|^2 Z_2 + \beta Z_1 + \sqrt{2\mathrm{D}_2}\eta(t). \tag{5.2}$$

In Eqn.5.2, $\alpha$ and $\beta$ are the coupling strengths: $\alpha$ scales the influence of the second oscillator ($Z_2$) on the first oscillator ($Z_1$) and corresponds to the backward electro-mechanical coupling parameter in the detailed biophysical model of Chapter 4; $\beta$ scales the influence of the first oscillator on the second oscillator and corresponds to the direct mechano-electrical coupling in the hair cell model. Noise terms $\zeta(t)$ and $\eta(t)$ are two complex uncorrelated Gaussian white noises (GWNs), $\langle \zeta(t)\eta(t) \rangle = 0$, and individually their real and complex parts are $\delta$– correlated GWNs; $\mathrm{D}_{1,2}$ are the noise intensities. In the following, we assume that noise in the first oscillator, referring to mechanical compartment is much larger than noise in the second oscillator (electrical compartment), that is, $\mathrm{D}_1 \gg \mathrm{D}_2$. Finally, the external periodic force, $f\, e^{i\omega_s t}$, is introduced to the first oscillator. Synchronization and bifurcations in the deterministic autonomous case, $f = \mathrm{D}_1 = \mathrm{D}_2 = 0$, was studied in details in [121].

In the following we set $r_1 = r_2 = 1$, i.e. we consider both oscillators in the regime of limit cycle oscillations and transform variables to the polar coordinate systems, $Z_j = \mathcal{R}_j e^{i\Phi_j}$; $j = 1, 2$, where $\mathcal{R}_j$ and $\Phi_j$ are instantaneous amplitudes and phases, respectively. This gives two equations for the amplitudes,

$$\dot{\mathcal{R}}_1 = \mathcal{R}_1 - \mathcal{R}_1^3 + \alpha \mathcal{R}_2 \cos(\Phi_1 - \Phi_2) + f \cos(\omega_s t - \Phi_1) + \sqrt{2\mathrm{D}_1}\, \Gamma_1(t),$$
$$\dot{\mathcal{R}}_2 = \mathcal{R}_2 - \mathcal{R}_2^3 + \beta \mathcal{R}_1 \cos(\Phi_1 - \Phi_2) + \sqrt{2\mathrm{D}_2}\, \Gamma_2(t),$$

and two for the phases,

$$\dot{\Phi}_1 = \omega_1 - \alpha \frac{\mathcal{R}_2}{\mathcal{R}_1} \sin(\Phi_1 - \Phi_2) + \frac{f}{\mathcal{R}_1} \sin(\omega_s t - \Phi_1) + \sqrt{\frac{2\mathrm{D}_1}{\mathcal{R}_1^2}}\, \xi_1(t),$$
$$\dot{\Phi}_2 = \omega_2 + \beta \frac{\mathcal{R}_1}{\mathcal{R}_2} \sin(\Phi_1 - \Phi_2) + \sqrt{\frac{2\mathrm{D}_2}{\mathcal{R}_2^2}}\, \xi_2(t), \tag{5.3}$$

where $\Gamma_1(t)$, $\Gamma_2(t)$, $\xi_1(t)$ and $\xi_2(t)$ are uncorrelated GWNs with their correlation function $< \xi_j(t)\xi_{j'}(t+\tau) >= \delta(\tau)\delta_{j,j'}$, and $< \Gamma_j(t)\Gamma_{j'}(t+\tau) >= \delta(\tau)\delta_{j,j'}$.

Further simplification can be achieved by neglecting fluctuations of amplitudes, a procedure often used in theoretical studies of noisy oscillators [111, 112]. Here we set $\mathcal{R}_1 = \mathcal{R}_2 = 1$ which leads to the final phase equations,

$$\dot{\Phi}_1 = \omega_1 - \alpha \sin(\Phi_1 - \Phi_2) + f \sin(\omega_s t - \Phi_1) + \sqrt{2\mathrm{D}_1}\, \xi_1(t),$$
$$\dot{\Phi}_2 = \omega_2 + \beta \sin(\Phi_1 - \Phi_2) + \sqrt{2\mathrm{D}_2}\, \xi_2(t), \tag{5.4}$$

Our aim is to calculate the sensitivity function of the system, that is, given the input $f\, e^{i\omega_s t}$, to calculate the response, $\langle Z_2(t) \rangle$. We note that even in the deterministic case, $D_1 = D_2 = 0$, the dynamics of the phase model Eq. 5.4 is highly non-trivial [122]. Indeed, depending on the coupling strengths, the amplitude of external force and frequencies, the model may possess three distinct regimes: complete synchronization, when external force synchronizes both oscillators; partial synchronization, when external force synchronizes only one oscillator; and non-synchronous case when both oscillators and the external force oscillate with distinct frequencies [122].

### 5.3 Spontaneous phase dynamics

We start with the analysis of oscillation coherence in the absence of external force, $f = 0$,

$$\dot{\Phi}_1 = \omega_1 - \alpha \sin(\psi) + \sqrt{2D_1}\, \xi_1(t),$$
$$\dot{\Phi}_2 = \omega_2 + \beta \sin(\psi) + \sqrt{2D_2}\, \xi_2(t). \tag{5.5}$$

The phase difference, $\psi = \Phi_1 - \Phi_2$, follows the stochastic Adler's equation,

$$\dot{\psi} = \Delta - (\alpha + \beta)\sin\psi + \zeta_1(t), \tag{5.6}$$

where $\Delta = \omega_1 - \omega_2$ is the frequency detuning between the two oscillators; and $\zeta_1(t)$ is a $\delta-$ correlated GWN with $\langle\zeta_1(t)\zeta_1(t+\tau)\rangle = 2\mathrm{D}\delta(\tau)$, such that, $\mathrm{D} = \mathrm{D}_1 + \mathrm{D}_2$.

For $\Delta < \alpha + \beta$ the deterministic oscillators will become synchronized. With noise taken into account, the phases of both oscillators as well as the phase difference $\psi$ diffuse, and the effective diffusion coefficients are quantitative measures of the coherence of oscillations. Asymptotically for large time the variances of phases follow the diffusion law, $\mathrm{var}(\Phi_1) = 2\mathcal{D}_1\, t$, $\mathrm{var}(\Phi_2) = 2\mathcal{D}_2\, t$ and $\mathrm{var}(\psi) = 2\mathcal{D}_\psi\, t$, where $\mathcal{D}_{1,2}$ and $\mathcal{D}_\psi$ are effective diffusion constants of the phases and the phase difference, respectively. For zero coupling, $\alpha = \beta = 0$, the diffusion coefficients are equal to noise intensities, $\mathcal{D}_{1,2} = D_{1,2}$.

Below we follow A.N. Malakhov [112] in derivation for the diffusion coefficients of the first, $\mathcal{D}_1$, and the second, $\mathcal{D}_2$, oscillators. Let us introduce the phase sum, $\theta = \beta\Phi_1 + \alpha\Phi_2$, for which we obtain a simple diffusion on a tilted plane,

$$\dot{\theta} = (\alpha\omega_2 + \beta\omega_1) + \zeta_2(t),$$

where the GWN $\zeta_2(t)$ has the intensity $Q = \beta^2\mathrm{D}_1 + \alpha^2\mathrm{D}_2$. Thus, the following two-dimensional process describes coupled oscillators,

$$\dot{\psi} = \Delta - (\alpha + \beta)\sin\psi + \sqrt{2D}\zeta_1(t),$$
$$\dot{\theta} = (\alpha\omega_2 + \beta\omega_1) + \sqrt{2Q}\zeta_2(t),$$

Notice that white noises $\zeta_{1,2}$ for $\psi$ and $\theta$ are correlated: $\langle\zeta_1(t)\zeta_2(t+\tau)\rangle = 2(\beta\mathrm{D}_1 - \alpha\mathrm{D}_2)\delta(\tau)$. with $\langle\zeta_1(t)\zeta_2(t+\tau)\rangle = 2R\delta(\tau)$ with $R = \beta\mathrm{D}_1 - \alpha\mathrm{D}_2$. Hence, $\psi$ and $\theta$ are correlated. In this regard, the effective diffusion constants for $\psi$ and $\theta$ are known. On one hand, $\mathcal{D}_\psi$ can be calculated analytically in quadratures [123]. In particular for $\Delta = 0$ (i.e. for zero frequency

mismatch), it is given by [124],

$$\mathcal{D}_\psi = \mathrm{D}\left[I_0\left(\frac{\alpha+\beta}{\mathrm{D}}\right)\right]^{-2}, \tag{5.7}$$

where $I_0$ is the modified Bessel function of the first order. On the other hand, $\mathcal{D}_\theta = Q = \beta^2\mathrm{D}_1 + \alpha^2\mathrm{D}_2$. The individual phases can be expressed in terms of $\psi$ and $\theta$ as,

$$\Phi_1 = \frac{\theta+\alpha\psi}{\alpha+\beta}, \quad \Phi_2 = \frac{\theta-\beta\psi}{\alpha+\beta}.$$

Thus, their variances are given by:

$$\mathrm{var}(\Phi_1) = \frac{\mathrm{var}(\theta)+\alpha^2\mathrm{var}(\psi)+2\alpha\langle\psi,\theta\rangle}{(\alpha+\beta)^2},$$
$$\mathrm{var}(\Phi_2) = \frac{\mathrm{var}(\theta)+\beta^2\mathrm{var}(\psi)-2\beta\langle\psi,\theta\rangle}{(\alpha+\beta)^2},$$

where the cumulant bracket $\langle\psi,\theta\rangle = \langle\psi\theta\rangle - \langle\psi\rangle\langle\theta\rangle$. As a result, the effective diffusion coefficients are given by,

$$\mathcal{D}_1 = \frac{\mathcal{D}_\theta+\alpha^2\mathcal{D}_\psi+2\alpha\mathcal{D}_x}{(\alpha+\beta)^2},$$
$$\mathcal{D}_2 = \frac{\mathcal{D}_\theta+\beta^2\mathcal{D}_\psi-2\beta\mathcal{D}_x}{(\alpha+\beta)^2}, \tag{5.8}$$

where $\mathcal{D}_x = (1/2)d\langle\psi,\theta\rangle/dt$ is given by

$$\mathcal{D}_x = \mathcal{D}_\psi\frac{R}{\mathrm{D}} = \mathcal{D}_\psi\frac{\beta\mathrm{D}_1-\alpha\mathrm{D}_2}{\mathrm{D}_1+\mathrm{D}_2}. \tag{5.9}$$

Thus, by substituting the expressions of $\mathcal{D}_x$, $\mathcal{D}_\theta$, and $\mathcal{D}_\psi$ from Eq.5.7 into Eq. 5.8, we obtain the desired result for the effective diffusion constants, $\mathcal{D}_1$ and $\mathcal{D}_2$. Fig. 5.1– **B** shows that analytical results match perfectly with the direct numerical simulations (depicted in diamond symbols) of Eq.5.5.

Below we consider the case which is similar to that of the hair cell system, where the peripheral compartment (the first oscillator) is more noisy compared to the electrical compartment (second oscillator). In this regard without loss of generality, we set $\mathrm{D}_1 = 0.1$,

and $D_2 = 0.001$, albeit, the effect of changing $D_1$ will be explored later in this chapter. Under these assumptions, the diffusion coefficients calculated using Eqs. 5.8, show that for sufficiently small forward coupling strength $\alpha$ and increasing backward coupling strength $\beta$, the diffusion coefficient of the first oscillator $\mathcal{D}_1$ decreases, while $\mathcal{D}_2$ increases. The diffusion coefficient of the phase difference $\mathcal{D}_\psi$ decreases too, which indicates that the two oscillators becomes gradually synchronized by increasing the forward coupling strength. The decrease in $\mathcal{D}_1$ is attributed to the less noisy nature of the second oscillator. Hence, for $\beta << \alpha$, the backward coupling stabilizes the first oscillator. For increasing $\beta$, more noise is being fed froward into the second oscillator, hence, the noise overcomes the stabilizing effect of the second oscillator. As a result, $\mathcal{D}_1$ attains a minimum (c.f. Fig. 5.1 **A**– **C**). Beyond this minimum, further increase of $\beta$ results in an increase in $\mathcal{D}_2$, and $\mathcal{D}_1$. Fig. 5.1– **C** shows that this effect disappears for large $\alpha$, for the same obvious reason, that the noise fed backward to the first oscillator carries more weight (indicated by larger $\alpha$), and so the diffusion in both oscillators becomes comparable, leading to earlier saturation of both diffusion coefficients $\mathcal{D}_1$ and $\mathcal{D}_2$ to a common asymptotic level as indicated in **C**. This early saturation stage is marked by the drop to zero in $\mathcal{D}_\psi$. Therefore, in general, increasing the forward coupling results in increase of the diffusion coefficients $\mathcal{D}_1$, and $\mathcal{D}_2$, except for a narrow range of the coupling strengths as indicated in Fig. 5.1 **A**– **C**. In other words, oscillators becomes less coherent with the increase of forward coupling, $\beta$. On the other hand, increasing $\alpha$ for fixed forward coupling, causes the diffusion coefficients to decrease monotonically ( Fig. 5.1– **D**), indicating that $\alpha$, in general contributes to minimize the noise in both oscillators. In essence, the second (less noisy) oscillator improves coherence of the first oscillator.

While variation of the coupling strengths $\beta$ and $\alpha$ for fixed noise levels $D_1$ resulted in intuitive changes in the coherence of oscillators, variation of noise in the first oscillator led to a *novel* counter–intuitive behavior of the oscillators' coherence. Intuition dictates that

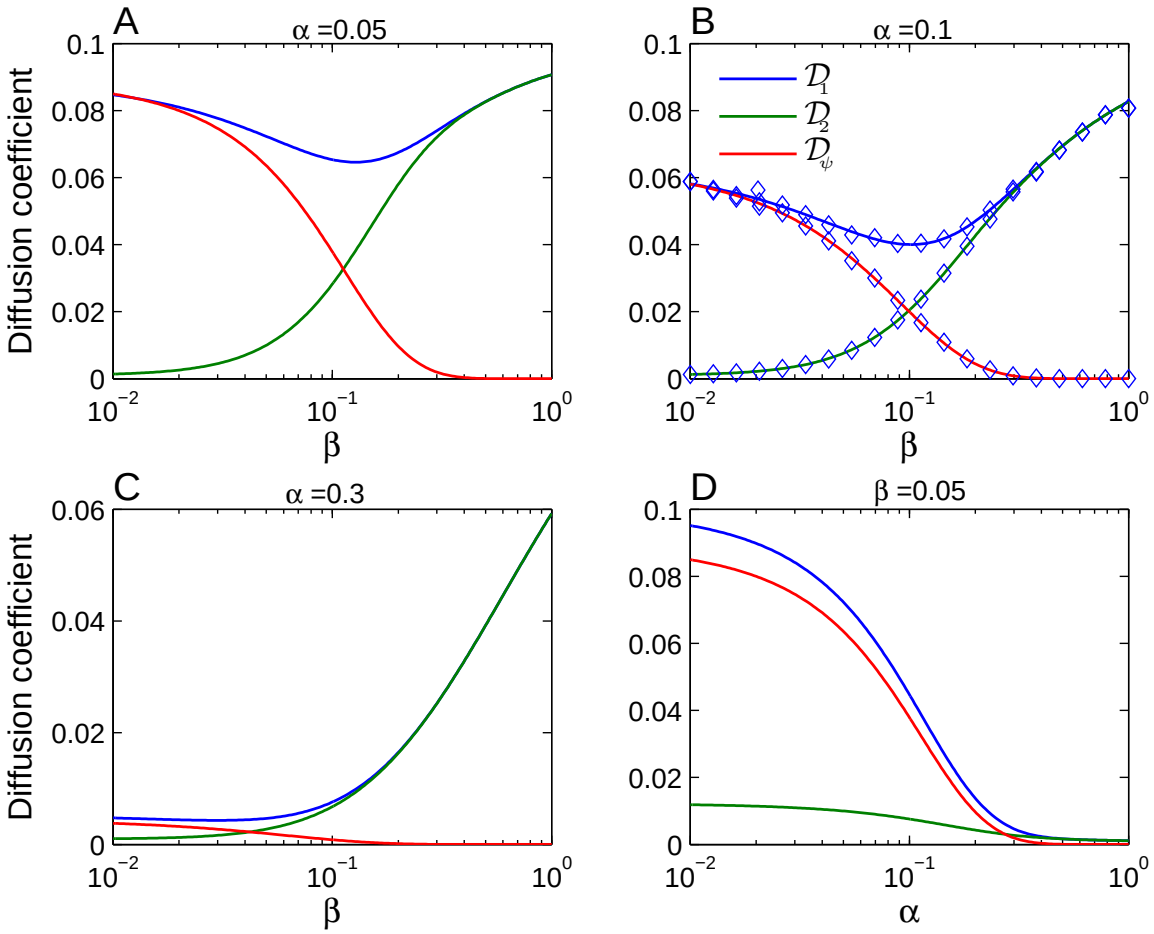


Figure 5.1: Effect of coupling strength on the diffusion coefficients $\mathcal{D}_1$,$\mathcal{D}_2$, and that of the phase difference $\mathcal{D}_\psi$ for (**A**) $\alpha = 0.05$, (**B**) $\alpha = 0.1$, (**C**) $\alpha = 0.1$, (**D**) $\beta = 0.05$. The calculation are done using the analytical expressions for $\mathcal{D}_\psi, \mathcal{D}_1$, and $\mathcal{D}_2$ for $D_1$=0.1 and $D_2 = 0.001$, and $\Delta\omega = 0$. For $\alpha = 0.1$ (panel **B**), numerical calculations (diamonds) are superimposed on the corresponding analytical curves. Numerical calculations are done by averaging an ensemble of $2^{18}$ realizations, each of 100 seconds in length.

an increase of noise in the first oscillator, $D_1$ should lead to less coherent oscillations of the first oscillator (larger phase diffusion constant, $\mathcal{D}_1$, and because of coupling, should lead to less coherent oscillations of the second oscillator (larger phase diffusion constant $\mathcal{D}_2$). However, we have found that the although the first oscillator does indeed follows such a behavior, the diffusion constant of the second oscillator possesses a maximum as a function of noise level in the first oscillator and then drops. In other words, pumping more noise in

the first oscillator enhances the coherence of oscillations of the second oscillator, despite their coupling! The effect is illustrated in Fig. 5.2 **A**– **B**. We notice that the maximal value of $\mathcal{D}_2$ decreases with increasing $\alpha$ (c.f. Fig. 5.2– **A**) and increases with increasing $\beta$ as shown in Fig. 5.2– **B**.

This effect is indeed different from stochastic resonance [125, 126] where signal to noise ratio is maximized for an optimal value of the noise intensity. In particular, stochastic resonance requires the existence of external forcing, which is absent in the dynamics considered here ($f = 0$). On the other hand, the phenomenon of coherence resonance [127–129] is also not relevant, as it requires a maximization for the coherence, while here the coherence is minimized at certain noise intensity.

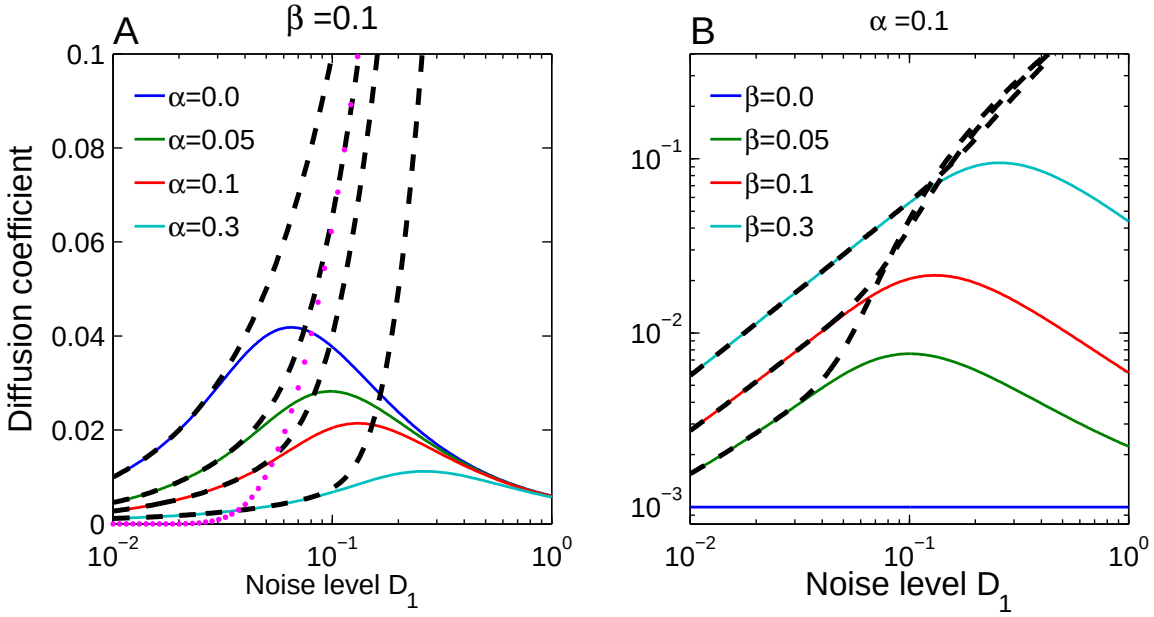


Figure 5.2: Effect of $D_1$ on the diffusion coefficient of $\Phi_2$. In (**A**) $\alpha = 0.1$; (**B**) $\beta = 0.1$. Continuous (colored) lines correspond to the diffusion coefficient of the second oscillator $\mathcal{D}_2$ for the parameter values in the legends; dashed black lines correspond to $\mathcal{D}_1$, each dashed line corresponds to the parameter value for the curve of $\mathcal{D}_2$ it asymptotes to at low noise levels. The dotted magenta line in (**A**) is the diffusion coefficient $\mathcal{D}_\psi$ for $\alpha = 0$, and $\beta = 0.1$. The calculations are done the same way in Fig. 5.1 with $D_2$=0.001, and $\Delta\omega = 0$ are held fixed.

In Fig. 5.2, we notice that $\mathcal{D}_1$, and $\mathcal{D}_2$ coincide with each other for small noise intensities, but they depart from each other for increasing noise levels (dashed black lines versus colored lines in Fig. 5.2). Moreover, $\mathcal{D}_\psi$ is slightly increasing for small $D_1$, but increases rapidly for larger $D_1$ (Fig. 5.2–bf A, dotted magenta line), indicating that the two oscillators becomes less phase coherent. This non-monotonous behavior of $\mathcal{D}_2$ is robust for all values of $\alpha$ and nonzero values of $\beta$ . Thus, to explain the above described phenomenon we can set $\alpha = 0$ (blue curve in Fig. 5.2–**A**), which corresponds to the unidirectionally coupled oscillators. This simplifies the diffusion coefficient to,

$$\mathcal{D}_2 = D_1 + \mathcal{D}_\psi \left(1 - \frac{2D_1}{D_1 + D_2}\right), \quad \mathcal{D}_\psi = \frac{D_1 + D_2}{I_0^2\left(\frac{\beta}{D_1+D_2}\right)}. \tag{5.10}$$

For weak noise, $D_1 \ll 1$, the phase difference diffusion is small, $\mathcal{D}_\psi \ll 1$, and so from the equation above $\mathcal{D}_2 \approx D_1$ and increases with $D_1$, as observed in Fig. 5.2, where both $\mathcal{D}_1$ and $\mathcal{D}_2$ coincide with each other in this limit. For large noise, $D_1 \gg 1$, $I_0(\beta/D) \approx 1$, and $\mathcal{D}_\psi \approx D_1 + D_2$, and so $\mathcal{D}_2 \approx D_2$. In other words, for $D_1 \to \infty$, the diffusion constant of the second oscillator attains its uncoupled value, so that the second oscillator does not feel any input from the first oscillator.

Now consider the dynamical equation for $\Phi_1$ when $\alpha = 0$:

$$\dot{\phi_1} = \omega_1 + \sqrt{2D_1}\xi_1(t),$$

Although $\Phi_1(t)$ is non-stationary processes, the process defined by $x = \cos(\Phi_1)$ is stationary with the autocorrelation function,

$$C_1(\tau) =< x(t)x(t+\tau) >= \frac{1}{2}e^{-D_1\tau}\cos(\omega_1\tau).$$

The one-sided power spectral density is,

$$S_1(\omega) = \int_0^\infty C_1(\tau) * e^{-i\omega\tau}d\omega = \frac{1}{2}D_1\left[\frac{1}{D_1^2 + (\omega_1+\omega)^2} + \frac{1}{D_1^2 + (\omega_1-\omega)^2}\right], \tag{5.11}$$

which is a shifted Lorentzian centered around $\omega_1$, with its full width half maximum (FWHM) equal to $D_1$, where FWHM is defined to be the frequency difference between the frequencies at which $S_1(\omega) = S_1(\omega_1)/2$. Thus, by increasing noise level $D_1$ the first oscillator becomes more noisy indicated by a decrease in its power spectral density (PSD) peak and the increase in its FWHM as shown in Fig. 5.3–**A**. On the other hand, since both oscillators are tuned to the same angular frequency ($\omega_1 = \omega_2 = \omega_0$), one would expect that the power spectral density of the second oscillator to be of Lorentzian shape too, and its width to be proportional to the effective noise experienced by it. The noise level in the second oscillator when $\beta = 0$ is given by $D_2$. While for non-zero value of $\beta$ it is given by the diffusion coefficient $\mathcal{D}_2$, thus the one-sided power spectral density for the second oscillator is given by,

$$S_2(\omega) = \frac{1}{2}\mathcal{D}_2\left[\frac{1}{\mathcal{D}_2^2 + (\omega+\omega_2)^2} + \frac{1}{\mathcal{D}_2^2 + (\omega-\omega_2)^2}\right]. \tag{5.12}$$

Indeed, this is in quite agreement with the numerical calculations as indicated in Fig. 5.3–**B**. Notice that the non–monotonous behavior of $\mathcal{D}_2$ (Fig. 5.2) is also characterized by the a non-monotonous change in the width of the power spectrum of $\Phi_2$ as indicated in Fig. 5.3–**B** (red curve versus blue curve).

Now we can use expressions for the PSDs to proceed in quantifying the effect of noise in terms of power transferred from the first oscillator within the bandwidth of the second oscillator. To do so, we proceed as follows. First, since the second oscillator is most sensitive to frequencies within its bandwidth, we need to find the left ($\omega_{2,l}$) and the right $\omega_{2,r}$ frequencies corresponding to $S_2(\omega_2)/2$. From the above equation of $S_2(\omega)$ we find that, $\omega_{2,r} - \omega_{2,l} = \mathcal{D}_2$; $\omega_{2,l} = \omega_2 - \mathcal{D}_2/2$. Second, to find the power transferred from the first oscillator within this bandwidth ($\mathcal{P}_{BW}$), we integrate $S_1(\omega)$ between $\omega_{2,l}$ and $\omega_{2,r}$, hence,

$$\mathcal{P}_{BW} = \int_{\omega_l}^{\omega_r} S_1(\omega)\, d\omega = \frac{1}{2}\tan^{-1}\left[\frac{2\omega\mathcal{D}_1}{{\mathcal{D}_1}^2 - (\omega^2 - \omega_1^2)}\right]\Bigg|_{\omega_l}^{\omega_R} = \frac{1}{2}\tan^{-1}\left[\frac{\mathcal{D}_2/\mathcal{D}_1}{1 - (\frac{\mathcal{D}_2}{2\mathcal{D}_1})^2}\right] \tag{5.13}$$

where we neglected the first term on the right hand side of $S_2(\omega)$ due to its small contribution at positive frequencies. While the area under $S_1(\omega)$ curve is preserved and given by $(var(\Phi_1)/2)$ [130]. For large $D_1$, $S_1(\omega)$ becomes nearly flat as that for a Gaussian white noise. Therefore, the power is distributed evenly all over the frequency range, hence, less power per unit frequency is achieved. Consequently, the power transferred within the bandwidth of the second oscillator is reduced as shown in Fig. 5.3–**C**. This reduction in $\mathcal{P}_{BW}$ means that the diffusion coefficient of the second oscillator $\mathcal{D}_2$ becomes smaller and smaller as less noise power is transferred from the first oscillator to the second.

Using Eq. 5.13, for $\frac{\mathcal{D}_2}{\mathcal{D}_1} << 1$, $\mathcal{P}_{BW} \approx \frac{1}{2}\frac{\mathcal{D}_2}{\mathcal{D}_1}$. Fig. 5.3– **C** shows this dependency for $\alpha = 0,$ and $\beta = 0.1$ (blue curve in Fig. 5.2–**A**). Fig. 5.3–**C** shows that the power changing linearly for small $D_1$, and then reduced for further increase in $D_1$, a point characterized by reduction in the increasing rate of $\mathcal{D}_2$ as shown in Fig. 5.2, at which also $\mathcal{D}_1$ and $\mathcal{D}_2$ depart from each other.

## 5.4 Response dynamics

In the presence of external perturbation ($f \neq 0$), Eq. 5.4 can be rewritten with the phases being expressed with respect to a frame co–rotating with frequency equal to that of the external perturbation $\omega_s$, then by introducing the following set of variables

$$\varphi_1 = \Phi_1 - \omega_s t, \quad \varphi_2 = \Phi_2 - \omega_s t,$$

$$\delta_1 = \omega_1 - \omega_s, \quad \delta_2 = \omega_2 - \omega_s$$

The phase dynamics equations then take the form,

$$\dot{\varphi}_1 = \delta_1 - \alpha \sin(\varphi_1 - \varphi_2) - A \sin(\varphi_1) + \sqrt{2D_1}\xi_1 \tag{5.14}$$

$$\dot{\varphi}_2 = \delta_1 - \Delta + \beta \sin(\varphi_1 - \varphi_2) + \sqrt{2D_2}\xi_2 \tag{5.15}$$

where, $\Delta = \omega_1 - \omega_2$. Deterministic dynamics ($D_1 = D_2 = 0$) of these two coupled phase oscillators are studied in details in [122]. According to linear stability analysis for the

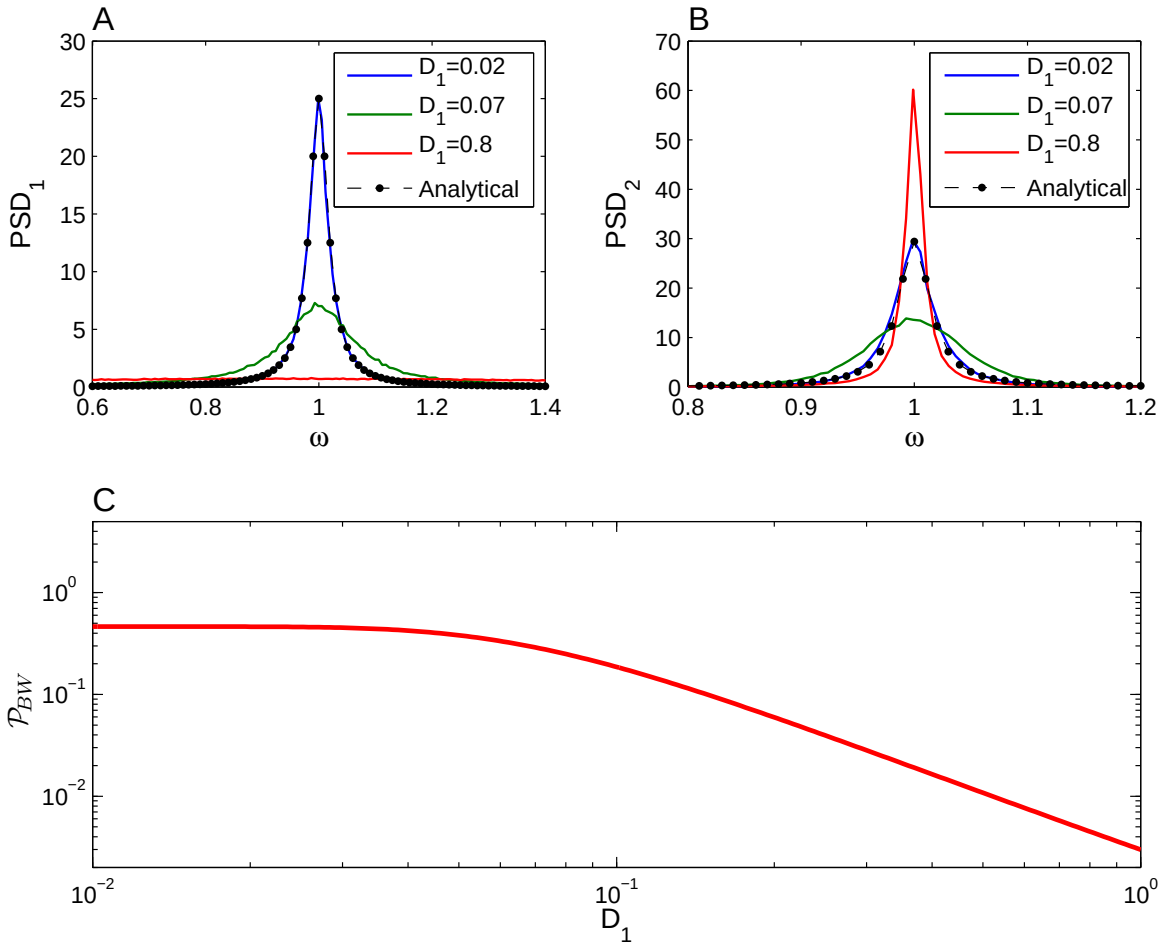


Figure 5.3: Energy transfer per unit time (power transfer) from the first oscillator to the second one. (**A**) Power spectral density of the first oscillator for different noise levels in the first oscillator $D_1$ as indicated in the legend. (**B**) Same as in **A** but for the second oscillator. Both in **A** and **B** the analytical calculations are superimposed with black dots for $D_1 = 0.8$. (**C**) The power transferred $\mathcal{P}_{\mathcal{BW}}$ as a function of $D_1$ which is equal $\mathcal{D}_1$ for $\alpha = 0$. Other parameters are $\alpha = 0, \beta = 0.1$, and $D_2 = 0.001$.

deterministic system possesses four equilibrium points, provided that

$$\left|\frac{\Delta - \delta_1}{\beta}\right| \leq 1, \text{ and } \quad \left|\frac{\alpha(\delta_1 - \Delta) - \beta\delta_1}{f\beta}\right| \leq 1 \tag{5.16}$$

According to Anishchenko et al. [122], these four points will lose stability through saddle-node bifurcation, where a stable node (equilibrium point) collides with a saddle point on the stable manifold, and they annihilate together at the bifurcation line determined by the

two parameters $f$ and $\delta_1$. Within this regime, the system posses a single stable fixed point, and the regime is characterized by complete synchronization, in which the frequency of the two oscillators is locked to that of the driving (i.e. $\omega_1 = \omega_2 = \omega_s$). Outside this regime, two scenarios can take place depending of the frequency mismatch between the two oscillators ($\Delta$), and between the first oscillator and the external driving $\delta_1$. In the case $\Delta = 0$, and $\delta_1 \neq 0$ or $\Delta \neq 0$ and $\delta_1 = 0$, two invariant curves in the phase space corresponding to two dimensional torus. This two dimensional torus disappears through a saddle–node bifurcation of the invariant curves, at the point where three distinct frequencies appear in the system (i.e. $\omega_1 \neq \omega_2 \neq \omega_s$, and they are in irrational ratios with each other). Beyond this point, a three dimensional invariant torus exists.

In this section, we study the effect of bidirectional coupling strength, noise level $D_1$, and external sinusoidal perturbations on the response of the system when the two oscillators are tuned with each other ($\Delta = 0$), and with the external forcing ($\delta_1 = 0$). For $f \neq 0$, the time dependent ensemble average $\langle Z_j(t) \rangle$, where $j = 1, 2$ stands for the desired oscillator, is periodic with a period of $2\pi/\omega_s$ [25], thus it can be represented in terms of its Fourier components (FCs).

$$\langle Z_j(t) \rangle = \sum_{n=0}^{\infty} z_{j,n} e^{in\omega_j t}$$

On the other hand,

$$\langle Z_j(t) \rangle = \langle e^{i\Phi_j} \rangle = \langle e^{i\varphi_j} \rangle \, e^{i\omega_s t},$$

and so the fundamental harmonics are given by, $z_{j,1} = \langle e^{i\varphi_j} \rangle$. Here $\langle e^{i\varphi_j} \rangle$ indicates the degree of synchronization between the oscillator $j$ and the external force, which can be calculated using the stationary joint probability density of the phase differences, $P(\varphi_1, \varphi_2)$, as

$$z_{j,1} = \langle e^{i\varphi_j} \rangle = \int_0^{2\pi} \int_0^{2\pi} e^{i\varphi_j} P(\varphi_1, \varphi_2) d\varphi_1 \, d\varphi_2.$$

Therefore, the sensitivity function is defined as

$$\chi_j = \frac{|z_{j,1}|}{f} = \frac{\left| \langle e^{i\varphi_j} \rangle \right|}{f} \tag{5.17}$$

In order to calculate the sensitivity we need to find the stationary joint probability density function $P(\varphi_1, \varphi_2)$. To do so, we proceed by writing the two dimensional Fokker–Planck equation (FPE) [130] corresponding to the driven system

$$\begin{aligned}\frac{\partial P(t,\varphi_1,\varphi_2)}{\partial t} = \quad & -\frac{\partial}{\partial \varphi_1}\left(\left[\delta_1 - \alpha\, \sin(\varphi_1-\varphi_2) - f\, \sin(\varphi_1)\right] P\right) \\ & -\frac{\partial}{\partial \varphi_2}\left(\left[\delta_2 + \beta\, \sin(\varphi_1-\varphi_2)\right] P\right) + \mathrm{D}_1 \frac{\partial^2 P}{\partial \varphi_1^2} + \mathrm{D}_2 \frac{\partial^2 P}{\partial \varphi_2^2}.\end{aligned}$$

We note that the probability density is $2\pi$-periodic with respect to the phase differences, $P(t,\varphi_1,\varphi_2) = P(t,\varphi_1+2\pi,\varphi_2+2\pi)$, and can be expanded in Fourier series,

$$P(t,\varphi_1,\varphi_2) = \frac{1}{4\pi^2}\sum_{k=-\infty}^{\infty}\sum_{m=-\infty}^{\infty}\rho_{k,m}(t)e^{ik\varphi_1+im\varphi_2}, \tag{5.18}$$

where $\rho_{k,m}(t)$ are in general complex numbers and time dependent,

$$\rho_{k,m} = \frac{1}{4\pi^2}\int_{-\pi}^{\pi}\int_{-\pi}^{\pi} e^{-i(k\varphi_1+m\varphi_2)}P(t,\varphi_1,\varphi_2)\,d\varphi_1\,d\varphi_2.$$

The time evolution for its Fourier harmonics can be obtained by substituting the above form of the probability density function $P(t,\varphi_1,\varphi_2)$ in the FPE. Using the advantage that this is an infinite series, we can change indices. Using the following new set of indices

$$m+1 = m', k+1 = k'$$

$$m-1 = m'', k-1 = k''$$

Fokker-Planck equation can be rewritten in the following form,

$$\begin{aligned}\sum_{k,m=-\infty}^{\infty}\frac{\partial \rho_{k,m}}{\partial t}e^{ik\varphi_1+im\varphi_2} = \quad & \sum_{k',m''=-\infty}^{\infty}\left[\frac{\alpha}{2}k' - \frac{B}{2}m''\right]\rho_{k'-1,m''+1}e^{ik'\varphi_1+im''\varphi_2} \\ & -\sum_{k'',m'=-\infty}^{\infty}\left[\frac{\alpha}{2}k'' - \frac{B}{2}m'\right]\rho_{k''+1,m'-1}e^{ik''\varphi_1+im'\varphi_2} \\ & +\sum_{k',m=-\infty}^{\infty}\frac{A}{2}k'\rho_{k'-1,m}e^{ik'\varphi_1+im\varphi_2} - \sum_{k'',m=-\infty}^{\infty}\frac{f}{2}k''\rho_{k''+1,m}e^{ik''\varphi_1+im\varphi_2} \\ & -\sum_{k,m=-\infty}^{\infty}\left[i(k\delta_1+m\delta_2) + \mathrm{D}_1k^2 + \mathrm{D}_2\,m^2\right]\rho_{k,m}e^{ik\varphi_1+im\varphi_2}.\end{aligned}$$

Now, acknowledging that $m, k, k'$, and $k''$ are dummy indices, and by comparing terms on both sides, the above equation reduces to,

$$\begin{aligned}\dot{\rho}_{k,m} = \quad & \left[\frac{\alpha}{2}k - \frac{B}{2}m\right](\rho_{k-1,m+1} - \rho_{k+1,m-1}) + \frac{f}{2}k\,(\rho_{k-1,m} - \rho_{k+1,m}) \\ & - \left[i(k\delta_1 + m\delta_2) + \mathrm{D}_1 k^2 + \mathrm{D}_2 m^2\right]\rho_{k,m}, \end{aligned} \tag{5.19}$$

with $k, m$ taking integer values in $(-\infty, \infty)$, and $\rho_{0,0} = 1$, since $P(t, \varphi_1, \varphi_2)$ is normalized. By setting $\alpha$ and $\beta$ to zero, we recover the one dimensional case that corresponds to the Adler's equation [131]. As we can see from Eq. 5.19, every FC depends implicitly on the rest of the FCs. In the steady state where the left hand side of Eq. 5.19 vanishes we obtain an infinite chain of linear algebraic equations,

$$\begin{aligned}\left[\frac{\alpha}{2}k - \frac{B}{2}m\right](\rho_{k-1,m+1} - \rho_{k+1,m-1}) + \frac{f}{2}k\,(\rho_{k-1,m} - \rho_{k+1,m}) \\ - \left[i(k\delta_1 + m\delta_2) + \mathrm{D}_1 k^2 + \mathrm{D}_2 m^2\right]\rho_{k,m} = 0. \end{aligned} \tag{5.20}$$

In practice, such equations are solved for increasing number of harmonics, until a desired accuracy of probability density is achieved [131].

Note that the running indices $k$ and $m$ in general take on the integer numbers in $[-\infty, \infty]$. Thus, the stationary probability density can be found by solving a system of linear algebraic equations (Eqs. 5.21). The coefficients matrix corresponding to Eq. 5.21 is

$$\mathbf{A} = \begin{pmatrix} a_{-k,-m} & a_{-k,-m+1} & \cdots & a_{-k,m} \\ a_{-k+1,-m} & a_{-k+1,-m+1} & \cdots & a_{-k+1,m} \\ \vdots & \vdots & \ddots & \vdots \\ a_{k,-m} & a_{k,-m+1} & \cdots & a_{k,m} \end{pmatrix}$$

where $a_{k,m}$ is the coefficient of the corresponding Fourier harmonic $\rho_{k,m}$, i.e. $a_{k,m} = -\left[i(k\delta_1 + m\delta_2) + \mathrm{D}_1 k^2 + \mathrm{D}_2 m^2\right]$ ...etc. Now, consider $n \times n$ to be the maximum number of Fourier harmonics we are solving for, and consequently the number of equations to be solved. The indexes $k$ and $m$ take values from $-n, -n+1, \ldots, n-1, n$. For example, if n=2; then the matrix $\mathbf{A}$ is,

$$\mathbf{A} = \begin{pmatrix} a_{-2,-2} & a_{-2,-1} & a_{-2,0} & a_{-2,1} & a_{-2,2} \\ a_{-1,-2} & a_{-1,-1} & a_{-1,0} & a_{-1,1} & a_{-1,2} \\ a_{0,-2} & a_{0,-1} & a_{0,0} & a_{0,1} & a_{0,2} \\ a_{1,-2} & a_{1,-1} & a_{1,0} & a_{1,1} & a_{1,2} \\ a_{2,-2} & a_{2,-1} & a_{2,0} & a_{2,1} & a_{2,2} \end{pmatrix}$$

As one can see, the coefficients corresponding to a single equation (for single value of $k$, and $m$ in Eq. 5.21) are arranged in S–shape (indicated by the elements marked in red) in the matrix **A**. This calls to rearrange the matrix so that the coefficients for every equation are located in a single row. To do so, we set up a new matrix $\mathcal{A}$, with the dimension $[(2n+1)^2 \times (2n+1)^2]$ ($n = 2$ in the above example). Notice that every Fourier harmonic may appear in more than one equation, so we have to collect the coefficients corresponding to that harmonic in one column in the matrix $\mathcal{A}$. Moreover, every equation contains five variables (five Fourier harmonics), but they are not adjacent in the matrix $\mathcal{A}$, i.e. in one row of the matrix $\mathcal{A}$, their coefficients will not appear in five consecutive columns. Therefore, the length of the row is not 5, but it is 25 in this example. Thus each single row can have up to five nonzero elements. The coefficient of the Fourier harmonic $\rho_{k,m}$ ($a_{k,m}$), is mapped from $A$ to $\mathcal{A}$ using the element mapping

$$\mathcal{A}_{l,((k+n)*(2n+1)+m+n+1)} = a_{k,m}$$

where, $l = 1, 2, \ldots, (2n+1)^2$ stands for the equation (row) number. Since, the only known harmonic is $\rho_{0,0} = 1$, we are not solving for it. Instead, the column (coefficients) corresponding to this harmonic, will serve as the inhomogeneous part of the linear system. So, by eliminating this column, and the equation corresponding to it (row) from the matrix $\mathcal{A}$ we obtain a new coefficient matrix, which we will call **C**, with the dimension $[((2n+1)^2-1)\times((2n+1)^2-1)]$. The system now can be written in standard form $\mathbf{C}\rho = \mathbf{B}$, where **B** is the inhomogeneous part corresponding to the the vector of length $(2n+1)^2 - 1$

which contains all the coefficients corresponding to $\rho_{0,0}$ and $\rho$ is the vector of FCs. Note that $\rho$ has the dimension of $[((2n+1)^2-1)\times 1]$, which is equal to the dimension of one column of $\mathcal{A}$ reduced by 1 as we dropped the element $\rho_{0,0}$.

The above matrix equation was solved with standard method using Matlab, $\rho = \mathbf{C}^{-1}\mathbf{B}$. Each individual Fourier harmonic is given by $\rho_{k,m} = \rho((k+n)(2n+1)+m+n+1)$. The dimension ($[n\times n]$) of the matrix **A** was adjusted with increasing increment of 5 so that the first five harmonics converge within six significant digits, leaving the error on the order of ($O(10^{-7})$).

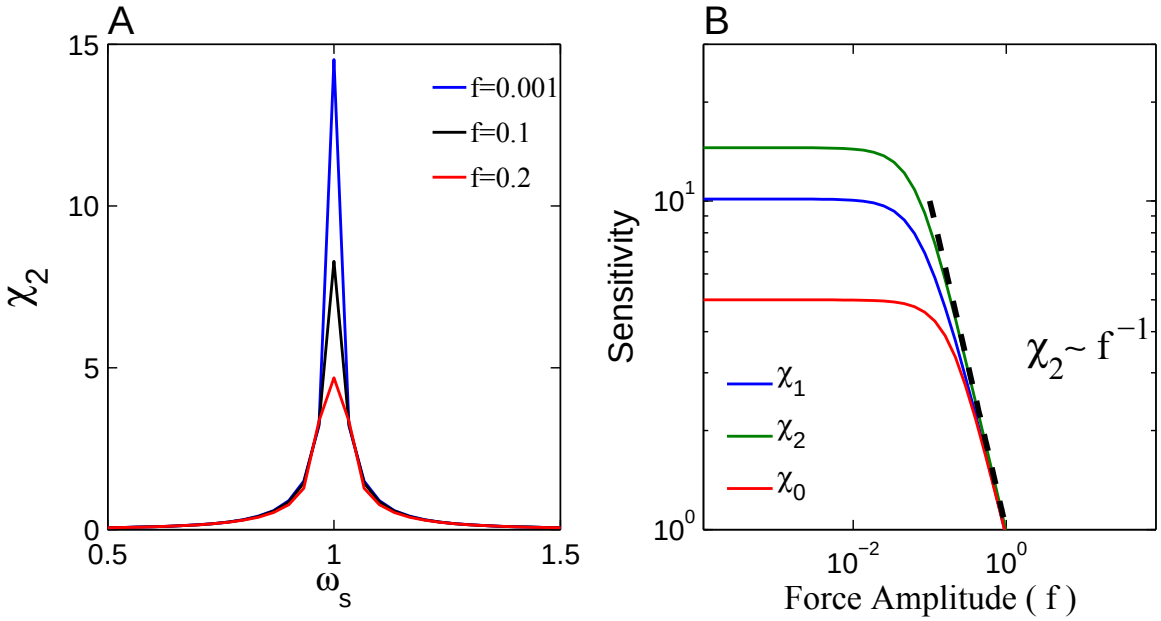


Figure 5.4: Sensitivity functions of single uncoupled oscillator ($\chi_0$), first oscillator ($\chi_1$), and the system ($\chi_2$). (**A**) Response function of the second oscillator ($\chi_2$) as a function of the external driving angular frequency ($\omega_s$), for $\alpha = 0.1$ and $\beta = 0.05$. (**B**) Response function of the first, second for $\alpha = 0.1$, $\beta = 0.05$, and that for a single oscillator ($\alpha = 0.0$) as a function of the driving amplitude ($f$) for $\delta_1 = 0$. Here The noise level $D_1 = 0.1$, $D_2 = 0.001$ , and $\Delta = 0$ are kept fixed for all curves in **A** and **B**.

Thus, by finding $\rho_{1,0}$, and $\rho_{0,1}$, we can rewrite the time dependent averages as

$$\langle Z_1(t)\rangle = \rho_{1,0}e^{i\omega_s t}, \text{ and } \quad \langle Z_2(t)\rangle = \rho_{0,1}e^{i\omega_s t},$$

Therefore, the sensitivity functions (Eq. 5.17) take the form

$$|\chi_1(f,\omega)| = \frac{|\rho_{1,0}|}{f}, \quad |\chi_2(f,\omega)| = \frac{|\rho_{0,1}|}{f},$$

where, $\chi_1$ and $\chi_2$ are the sensitivity of the first oscillator and the whole system composed of the two oscillators respectively.

In the absence of coupling ($\alpha = \beta = 0$) the sensitivity for the single oscillator, $\chi_0$, can be expressed via modified Bessel functions of the first kind with possibly complex order [108]:

$$\chi_0(f,\omega_s) = \frac{1}{f}\left|\frac{I_{1+i\delta_1/\mathrm{D}}(f/\mathrm{D}_1)}{I_{i\delta_1/\mathrm{D}}(f/\mathrm{D}_1)}\right|. \tag{5.21}$$

For small forcing, $\lim_{f\to 0}\chi_0 = \frac{1}{2\mathrm{D}_1}$, while for large forcing, the sensitivity scales as $\chi_0 \propto 1/f$ [108]. Hence, the response is linear for small forcing, and follows a power law with an exponent $-1$ for large forcing.

In a similar manner to the single uncoupled phase oscillator, we found that the system responds linearly to weak signals ($\chi_2$ = const), while for a strong signal it shows nonlinear compression with an exponent of -1 ($\chi_2 \propto f^{-1}$, Fig. 5.4–**B**), a phenomenon of great importance in the theory of sensory hair cells (Chapter 4), termed *compressive nonlinearity*. A comparison between $\chi_1, \chi_2$ versus $\chi_0 = \chi_1|_{\alpha=0}$, shows that coupling has an advantage in boosting the sensitivities $\chi_1$ and $\chi_2$ as indicated in the linear response regime where $f << \alpha$ and $\beta$. Increasing the amplitude of the external force degrades the sensitivity, and increases the width of the sensitivity curves, hence the system becomes less selective for fixed values of the coupling strength as shown in Fig. 5.4– **A** and **B**. Thus, based on the amplitude of the external driving ($f$), the system responds with specific sensitivity and frequency selectivity. In general, for ($\Delta = 0$), the system response function peaks at $\omega_s$ (Fig. 5.4– **A**), and so, stimulating the system at this frequency and measuring its response $\chi_2$, is equivalent to finding the maximal sensitivity as in Chapter 4.

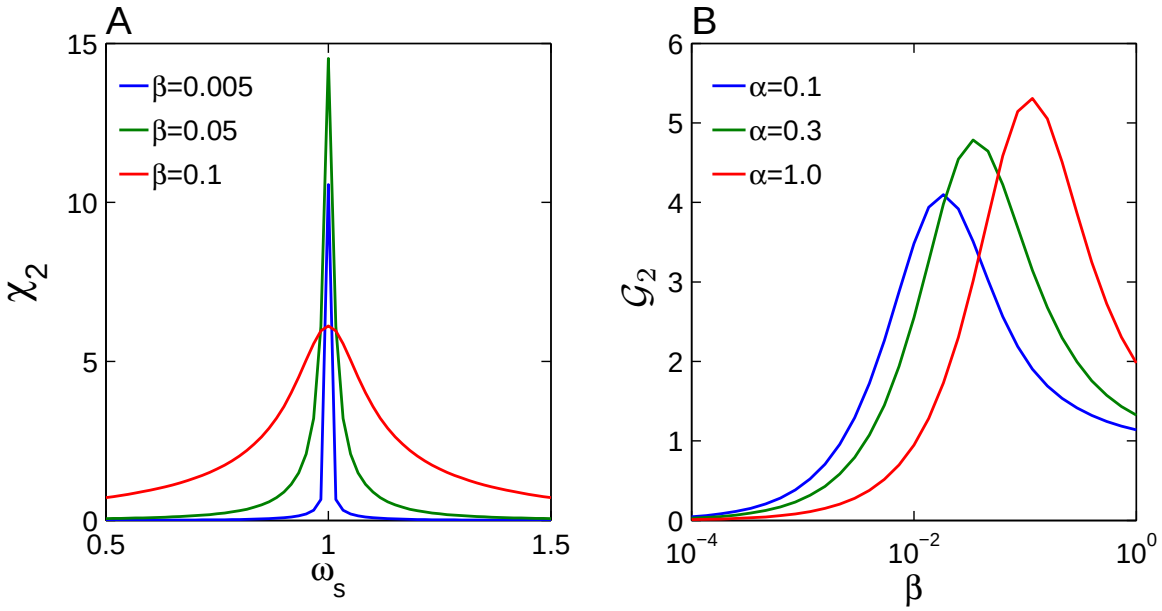


Figure 5.5: Effect of coupling strength on the system's response function ($\chi_2$), and gain $\mathcal{G}_2$. (**A**) $\chi_2$ as function of the driving frequency $\omega_s$ for $\alpha = 0.1$, blue curve in **B**, and different forward coupling strengths as indicated in the legend. (**B**) $\mathcal{G}_2$ as a function of the forward coupling strength $\beta$ for different backward coupling strengths $\alpha$ as indicated in the legend. Other parameters $D_1 = 0.1, f = 0.001$, $D_2 = 0.001$ , and $\Delta = 0$. In **B** we used a tuned stimulus for which $\delta_1 = 0$.

Coupling strengths can serve to control both sensitivity and frequency selectivity. Fig. 5.5 shows that increasing the forward coupling strength $\beta$ results in less frequency selectivity (panel **A**) indicated by the widening in the frequency response curve, $\chi_2(\omega_s)$. To characterize the effect of coupling on the system's sensitivity we introduce a sensitivity gain as the ratio of the system's sensitivity, $\chi_2$, to that of the single uncoupled oscillator $\chi_0$ which has the same noise as the peripheral (first) oscillator in the coupled system,

$$\mathcal{G}_j = \frac{\chi_j}{\chi_0}.$$

We notice that, although increasing the forward coupling strength, $\beta$, reduces the selectivity of the system to the input frequency, the system gain ($\mathcal{G}_2$) attains its maximum at a certain coupling strength $\beta$ for fixed backward coupling strength $\alpha$ as shown in Fig. 5.5– **B**. This behavior proves to exist for fixed $\beta$ and large $\alpha > 1$ too (see Fig. 5.6–**B**). We note, that

qualitatively similar behavior, i.e. the existence of optimal coupling was observed for the detailed biophysical model of the hair cell in Chapter 4 (cf. Fig. 4.15).

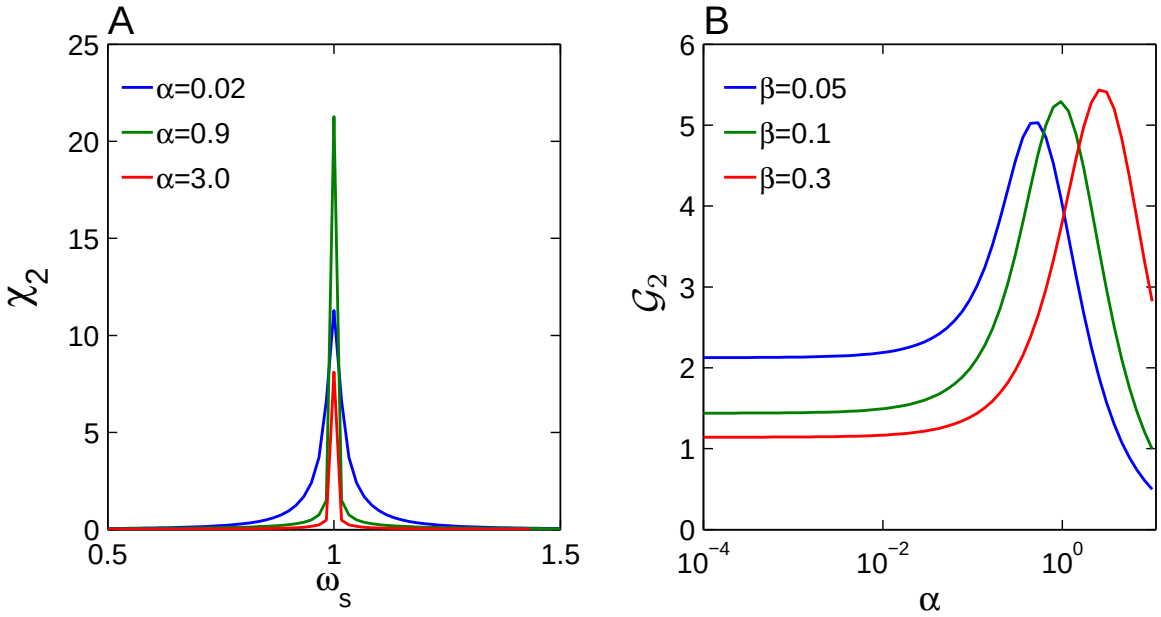


Figure 5.6: Effect of backward coupling strength $\alpha$ on the response of the response of the system ($\chi_2$) to external sinusoidal driving. (**A**) $\chi_2$ as function of the driving frequency $\omega_s$ for $\beta = 0.1$, blue curve in **B**, and different backward coupling strengths as indicated in the legend. (**B**) $\mathcal{G}_2$ as a function of the backward coupling $\beta$ for different forward coupling strengths $\alpha$ as indicated in the legend. Other parameters $D_1 = 0.1$, $D_2 = 0.001$ ,$f = 0.001$,and $\Delta = 0$. In **B**, we used a tuned stimulus for which $\delta_1 = 0$.

We note that for a system composed of two coupled linear cascades it is expected that an increase in forward coupling between cascades should boost the amplification of the system. This is indeed observed for small-to-moderate coupling strengths of our nonlinear coupled oscillators system. However, in contrast to a linear amplifier the sensitivity decreases for large coupling, which contradicts a mere "linear" intuition. The existence of an optimal coupling which maximizes the sensitivity can be explained by noticing two competitive tendencies. First, the sensitivity tends to increase with the increase of $\beta$ because increasing $\beta$ brings more signal from the first oscillator to the second one. Second, larger

coupling brings more noise from the first oscillator to the second oscillator, resulting in larger diffusion constant, as we have shown in the previous section. This second tendency reduces the sensitivity of the system. Thus, competition of these mechanisms results in the optimal coupling at which the sensitivity attains its maximal value. Increasing the backward coupling strength, $\alpha$, stabilizes the peripheral (first) oscillator, enhancing its coherence and thus decreasing the noise transferred to the second oscillator. Consequently, the gain $\mathcal{G}_2$ increases initially with $\alpha$. Further increase of $\alpha$ results in more robust system, which makes it harder for the stimulus to change the internal dynamics of the less noisy system. For large $\alpha$, $\mathcal{G}_2 < 1$ (see Fig. 5.6–**B**), indicating that it is harder for the stimulus to change the internal dynamics for a system composed of two oscillators as compared to that of a single uncoupled oscillator.

## 5.5 Effect of noise level on the system's sensitivity and gain

So far we have studied the response of the coupled oscillators system for fixed noise intensities $D_1$ and $D_2$. An important question is how the coupled system performs with respect to a single oscillator under increasing noise level? In the following we fixed noise intensity in the second oscillator, $D_2$, and vary noise in the first (peripheral) oscillator, $D_1$. Figure 5.7– **A** indicates that the sensitivities decrease with the increase of noise intensity. An interesting observation is that the system's sensitivity, $\chi_2$, tends to saturate at high values of noise intensity $D_1$ (green line in Fig. 5.7– **A**). This can be explained by the fact that the coherence of the second (output) oscillator increases for large noise in the first (peripheral) oscillator as was discussed in the previous section. Comparison of performance of the coupled system to a single oscillator using the gain, $\mathcal{G}$, shows that the coupled oscillators outperform the single oscillator for large noise intensities as shown in Fig. 5.7– **B**. For small noise in the first (peripheral) oscillator, $D_1 < D_2$, the gain is smaller than one, indicating

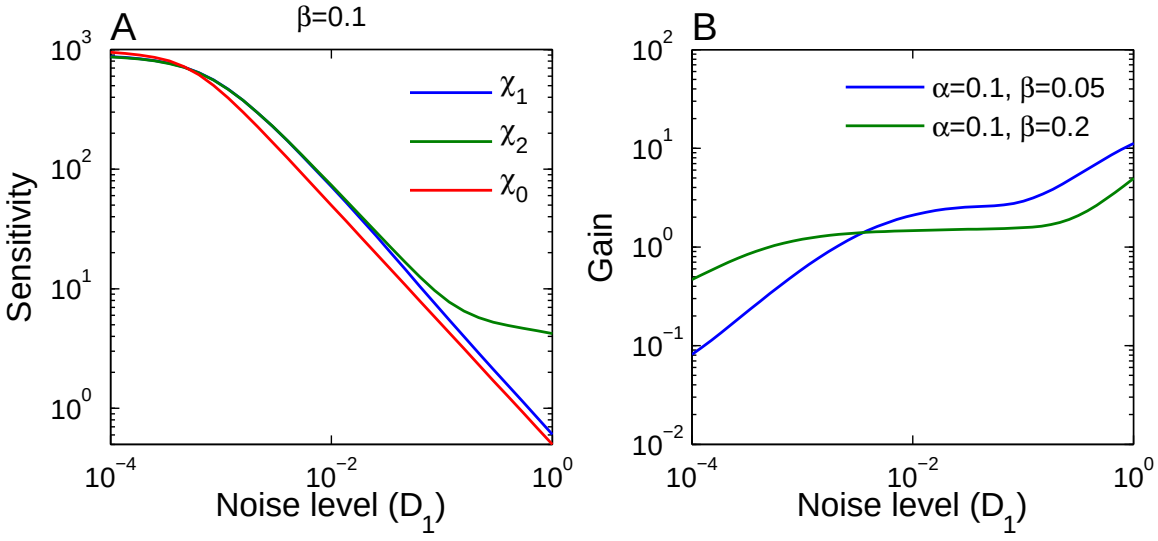


Figure 5.7: Effect of noise level in the first oscillator $D_1$ on the sensitivity and the gain of the system. (**A**) Sensitivity functions $\chi_1, \chi_2$, and that for single oscillator $\chi_0$ as a function of $D_1$ for $f = 10^{-3}$, $\alpha = 0.05$, and $\beta = 0.1$. (**B**) The gain function $\mathcal{G}_2$ for system composed of two noisy oscillators versus $D_1$ for two sets of coupling strengths ($\alpha$, and $\beta$), for $f = 10^{-4}$. Other parameters, $D_2 = 0.001$, $\delta_1 = 0$, and $\Delta = 0$ are held fixed.

that a single oscillator performs better than the coupled system. However, for $D_1 > D_2$, the coupled system possesses higher sensitivity as the gain is greater than 1.

Increasing the noise level $D_1$ also affects the selectivity of the system as demonstrated in Figure 5.8). For the coupled phase oscillators, increasing noise level $D_1$ in the first oscillator, renders the system more selective, an effect marked by the decrease in the band width of $\chi_2$ versus $\omega_s$ curve, as shown in Fig. 5.8–**B**. In contrast, for a single oscillator, increasing the noise level, decreases its coherence and freequency selectivity (Fig. 5.8–**A**). This effect is attributed to the decrease in the diffusion constant, $\mathcal{D}_2$, which enhances the coherence of oscillations and thus sharpness of the response to periodic forcing.

## 5.6 Conclusions

In this chapter we developed a general theoretical framework to study response properties of coupled stochastic oscillators to external periodic signal. We introduced a

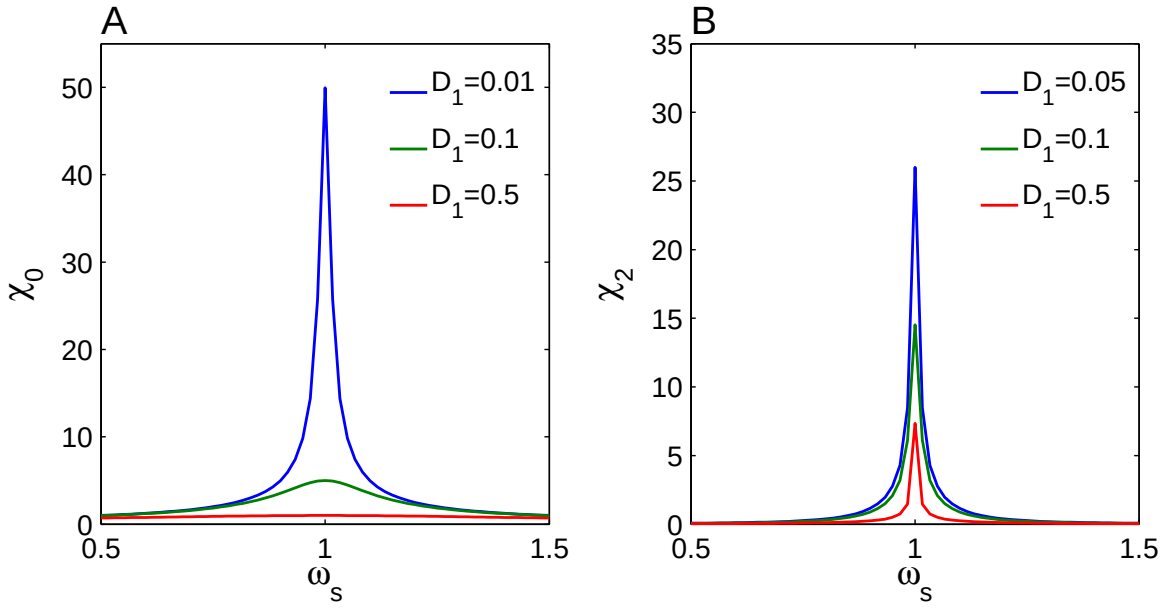


Figure 5.8: Sensitivity versus the frequency of the external driving $\omega_s$ for different noise levels $D_1$ as indicated in the legend. (**A**) Sensitivity of single oscillator $\chi_0$. (**B**) Sensitivity of the system composed of two coupled oscillator as a function of the driving frequency, for $\alpha = 0.1$, and $\beta = 0.05$ and $D_2 = 0.001$. The amplitude of the external forcing was set to $f = 10^{-3}$ in both **A** and **B**.

generic model of two bi-directionally coupled stochastic phase oscillators, whereby the external periodic force is applied to the first (peripheral) oscillator and the response is measured from the second (output) oscillator. The peripheral oscillator was assumed to be more noisy than the output oscillator. This arrangements resulted in a competition game of the ”bad” (more noisy, peripheral) and the ”good” (less noisy, output) oscillators in amplification of weak periodic signal.

We first studied oscillation coherence of the autonomous system (no external periodic force) and calculated analytically effective diffusion constants of both oscillators. We showed that the increase of forward coupling from the peripheral to the output oscillator (parameter $\beta$) suppresses coherence of both oscillators, as their diffusion constants decrease with the increase of the forward coupling strength. We note that the quality factor of an oscillator is reciprocal to the effective diffusion constant of oscillator's phase, i.e. smaller

phase diffusion refers to higher quality of oscillations. Thus, our theory explains the effect observed for the detailed biophysical model in Chapter 4, as the decrease of the quality factors of spontaneous oscillations with the increase of MET conductance shown in Fig. 4.10–C. In this game, the bad oscillator wins, as it has more influence on the system. In contrast, the increase in the backward coupling strength (parameter $\alpha$), i.e. coupling from the good to the bad oscillators, improves the oscillators' coherence, again in accordance with numerical results of biophysical hair cell model (cf. Fig. 4.10–A,B). The good oscillator wins, as it suppresses noise in the system.

A novel counter–intuitive effect was discovered when the noise level in the peripheral oscillator was varied. We made the bad oscillator even worse by increasing the noise in it. Intuition suggested that because of forward coupling to the good oscillator, the latter one should become more noisy. This was indeed observed: the effective diffusion constant of the output oscillator increased with the noise in the peripheral oscillator, but only up to a certain level, after which the output oscillator re-gained its coherence. In other words, the increase in input noise resulted in decrease of the effective diffusion constant of the second oscillator and in enhancement of its coherence. The explanation of this effect is rooted in the fact that the contribution from stochastic process corresponding to the peripheral oscillator, to the second oscillator is apparently a bounded noise [132]. Its variance is fixed and does not depend on the intensity of white Gaussian input noise, while it's power within a frequency band around it's natural frequency decreases with the increase of white Gaussian input noise, as the power spreads over a wider range of frequencies. Thus, the power effectively transmitted to the output oscillator decreases with the increase of noise in the input oscillator. As a result, the diffusion constant of the output oscillator decreases and it's coherence increases for large noise in the input oscillator.

Next, we used the Fokker-Planck equation formalism to calculate the sensitivity of the coupled oscillators system to external periodic force. In particular, we have developed

a numerical algorithm which allowed us to calculate the sensitivity of the system to any given accuracy. In this respect, we would like to stress that our approach is distinct from a direct simulation of the corresponding stochastic differential equations. We have shown that the effect of optimal coupling strength which maximized the sensitivity of the hair cell (observed in Chapter 4) is a rather generic phenomenon for a system composed of two unequally noisy coupled oscillators. It is explained by the competition of two mechanisms: (i) increase of sensitivity because more signal is coming to the output oscillator when the forward coupling strength increases and (ii) decrease of sensitivity, because the output oscillator becomes less coherent due to noise brought up from the peripheral oscillator. We demonstrated that the coupled oscillator system is beneficial in enhancing sensitivity and selectivity in noisy environment, when the first cascade (peripheral oscillator) is much noisier than the output cascade.

# 6 Conclusion and outlook

This dissertation presents a computational study of basic physical and dynamical principles involved in operation of peripheral mechanoreceptors, sensory hair cells, in vertebrates. It focuses on yet deficiently understood mechanisms underlying the onset of spontaneous voltage oscillations and reciprocal interactions between the individual and coupled mechanical and electrical compartments of hair cells in lower vertebrates. Through such interactions, hair cells are able to shape their response properties to amplify weak mechanical stimuli. In light of the recent hypothesis supported by experimental studies, it elaborates on how hair bundle mechanics along with multi-scale dynamics of the membrane potential in cells provide the feedback for amplification and tuning, thus reducing the effects of inevitable thermal fluctuations, and improving the sensitivity and selectivity of the system. The main results of this dissertation are listed below.

1. The developed computational model of coupled noisy mechanical and deterministic electrical compartments of the hair cell reproduces several previously reported experimental findings and provides experimentally testable predictions.

2. Membrane potential plays significant role in spontaneous dynamics of the sensory hair cells. In amphibians, the membrane potential serves as a control parameter: variation of the membrane potential can revert a quiescent hair bundle to an oscillatory, and vice versa.

3. Oscillatory hair cells exhibit diverse dynamical patterns in response to changes in the bidirectional coupling strengths between their mechanical and electrical compartments. The model predicts that within physiological range of the coupling strength mechanical and electrical oscillations are synchronized.

4. Variations in the conductances of basolateral ionic currents result in diverse dynamical patterns of the hair bundle dynamics and influence strongly the operational performance of the hair cell.

5. Thermal noise is a limiting factor for the sensitivity and selectivity of the hair cell. The coherence of spontaneous oscillations can be optimized by adjusting the strength of the bidirectional coupling or conductances of basolateral potassium currents.

6. The sensitivity and frequency selectivity of the hair cell to weak mechanical stimuli is maximized for optimal values of coupling strengths. Chapter 5 shows that this is a generic phenomenon for a sensor composed of two unequally noisy bi-directionally coupled oscillators.

7. In a general setup of two unequally noisy bi-directionally coupled oscillators the phase coherence of the less noisy oscillator depends in a non-monotonic fashion on the noise intensity of less coherent oscillator. We provide an analytical theory for this novel counter-intuitive effect.

Indeed, experiments on hair cells where both the hair bundle position and membrane potential are free to change, are needed for verifying model assumptions and predictions. These experiments are underway in the laboratory of Dr. Bozovic at UCLA.

For a better estimate of the membrane potential effects on the response and spontaneous dynamics of the hair bundle, we suggest to follow the voltage clamp protocol used in Chapter 3 of this dissertation. In this protocol the command voltage is given by a Gaussian band-limited noise, which allows for reliable estimates of the dynamic response of the hair bundle within the frequency band of the stimulus.

Several improvements are needed for the existing model. The main one is to use a more elaborate model for the mechanical compartment, which would include particulars

of location of mechano-electrical transduction channels, fast adaptation and the calcium dynamics. A major step forward would be to use biologically realistic finite-element type simulations of the hair bundle mechanics like in the group of Dr. Jong-Hoon Nam at University of Rochester, combined with detailed modeling of the membrane potential.

Saccular hair cells in bullfrogs are aggregated in groups of different activation polarity across the maccula. The frequency distribution of these hair cells is uniform across the epithelium [23]. *In vivo* the hair bundles are coupled by the overlaying otolithic membrane [41], and operate in groups. Previous modeling studies on coupled hair cells were limited only to coupled hair bundle. An obvious and important extension is to include the dynamics of the membrane voltage for each of coupled hair cells.

# References


[1] A. J. Hudspeth. Integrating the active process of hair cells with cochlear function. *Nat Rev Neurosci*, 15(9):600–614, 2014.

[2] A. J. Hudspeth. The cellular basis of hearing: the biophysics of hair cells. *Science*, 230(4727):745–752, 1985.

[3] M. A. Vollrath, K. Y. Kwan, and D. P. Corey. The micromachinery of mechanotransduction in hair cells. *Annual review of neuroscience*, 30:339, 2007.

[4] G. M. Shepherd and D. P. Corey. The extent of adaptation in bullfrog saccular hair cells. *The Journal of neuroscience*, 14(10):6217–6229, 1994.

[5] P. Martin, A. J. Hudspeth, and F. Jülicher. Comparison of a hair bundle's spontaneous oscillations with its response to mechanical stimulation reveals the underlying active process. *Proc.Natl.Acad.Sci.U.S.A*, 98(25):14380–14385, 2001.

[6] P. Martin, A. D. Mehta, and A. J. Hudspeth. Negative hair-bundle stiffness betrays a mechanism for mechanical amplification by the hair cell. *Proc. Natl. Acad. Sci USA*, 97(22):12026–12031, 2000.

[7] P. Martin and A. J. Hudspeth. Compressive nonlinearity in the hair bundle's active response to mechanical stimulation. *Proc. Natl. Acad. Sci. USA*, 98(25):14386–14391, 2001.

[8] P. Martin, D. Bozovic, Y. Choe, and A. J. Hudspeth. Spontaneous oscillation by hair bundles of the bullfrog's sacculus. *J. Neurosci.*, 23(11):4533–4548, 2003.

[9] Y. Roongthumskul, L. F. Hemsing, A. Kao, and D. Bozovic. Multiple-timescale dynamics underlying spontaneous oscillations of saccular hair bundles. *Biophysical journal*, 101(3):603–610, 2011.

[10] M. A. Rutherford and W. M. Roberts. Spikes and membrane potential oscillations in hair cells generate periodic afferent activity in the frog sacculus. *J. Neurosci.*, 29(32):10025–10037, 2009.

[11] D. Ramunno-Johnson, C. E. Strimbu, A. Kao, L. F. Hemsing, and D. Bozovic. Effects of the somatic ion channels upon spontaneous mechanical oscillations in hair bundles of the inner ear. *Hear. Res.*, 268(1-2):163–171, 2010.

[12] R. M. Amro and A. B. Neiman. Effect of bidirectional mechanoelectrical coupling on spontaneous oscillations and sensitivity in a model of hair cells. *Phys Rev E Stat Nonlin Soft Matter Phys*, 90(5-1):052704, 2014.

[13] J. Ashmore, P. Avan, W.E. Brownell, P. Dallos, K. Dierkes, R. Fettiplace, K. Grosh, C. M. Hackney, A. J. Hudspeth, F. Jülicher, B. Lindner, P. Martin, J. Meaud, C. Petit, J. R. Sacchi, and B. Canlon. The remarkable cochlear amplifier. *Hear. Res.*, 266:1–17, 2010.

[14] A. J. Hudspeth. Making an effort to listen: mechanical amplification in the ear. *Neuron*, 59(4):530–545, 2008.

[15] A. J. Hudspeth, F. Jülicher, and P. Martin. A critique of the critical cochlea: Hopf–a bifurcation–is better than none. *J. Neurophysiol.*, 104(3):1219–1229, 2010.

[16] T. Reichenbach and A. J. Hudspeth. The physics of hearing: fluid mechanics and the active process of the inner ear. *Reports on Progress in Physics*, 77(7):076601, 2014.

[17] G. A. Manley. Evidence for an active process and a cochlear amplifier in nonmammals. *J. Neurophysiol*, 86(2):541–549, 2001.

[18] R. Fettiplace and C. M. Hackney. The sensory and motor roles of auditory hair cells. *Nat. Rev. Neurosci.*, 7(1):19–29, 2006.

[19] P. Martin and A. J. Hudspeth. Active hair-bundle movements can amplify a hair cell's response to oscillatory mechanical stimuli. *Proc.Natl.Acad.Sci.U.S.A*, 96(25):14306–14311, 1999.

[20] G. A. Manley and L. Gallo. Otoacoustic emissions, hair cells, and myosin motors. *J. Acoust. Soc. Am.*, 102(2 Pt 1):1049–1055, 1997.

[21] M. Gelfand, O. Piro, M. O. Magnasco, and A. J. Hudspeth. Interactions between hair cells shape spontaneous otoacoustic emissions in a model of the tokay gecko's cochlea. *PloS one*, 5(6):e11116, 2010.

[22] B. Nadrowski, P. Martin, and F. Jülicher. Active hair-bundle motility harnesses noise to operate near an optimum of mechanosensitivity. *Proc. Natl. Acad. Sci. USA*, 101(33):12195–12200, 2004.

[23] D. Ramunno-Johnson, C. E. Strimbu, L. Fredrickson, K. Arisaka, and D. Bozovic. Distribution of frequencies of spontaneous oscillations in hair cells of the bullfrog sacculus. *Biophys.J.*, 96(3):1159–1168, 2009.

[24] V. M. Eguiluz, M. Ospeck, Y. Choe, A. J. Hudspeth, and M. O. Magnasco. Essential nonlinearities in hearing. *Phys. Rev. Lett.*, 84(22):5232–5235, 2000.

[25] S. Camalet, T. Duke, F. Jülicher, and J. Prost. Auditory sensitivity provided by self-tuned critical oscillations of hair cells. *Proc.Natl.Acad.Sci.U.S.A*, 97(7):3183–3188, 2000.

[26] D. Bozovic and A.J. Hudspeth. Hair-bundle movements elicited by transepithelial electrical stimulation of hair cells in the sacculus of the bullfrog. *Proc.Natl.Acad.Sci.U.S.A*, 100(3):958–963, 2003.

[27] C. E. Strimbu, D. Ramunno-Johnson, L. Fredrickson, K. Arisaka, and D. Bozovic. Correlated movement of hair bundles coupled to the otolithic membrane in the bullfrog sacculus. *Hear. Res.*, 256(1-2):58–63, 2009.

[28] M. A. Ruggero, N. C. Rich, A. Recio, S. S. Narayan, and L. Robles. Basilar-membrane responses to tones at the base of the chinchilla cochlea. *J. Acoust. Soc. Am.*, 101(4):2151–2163, 1997.

[29] L. Robles, M. A. Ruggero, and N. C. Rich. Basilar membrane mechanics at the base of the chinchilla cochlea. i. input-output functions, tuning curves, and response phases. *J. Acoust. Soc. Am.*, 80(5):1364–1374, 1986.

[30] D. T. Kemp. Stimulated acoustic emissions from within the human auditory system. *J Acoust Soc Am*, 64(5):1386–1391, 1978.

[31] D. T. Kemp. Evidence of mechanical nonlinearity and frequency selective wave amplification in the cochlea. *Arch Otorhinolaryngol*, 224(1-2):37–45, 1979.

[32] P. van Dijk, H. P. Wit, and J. M. Segenhout. Spontaneous otoacoustic emissions in the european edible frog (rana esculenta): spectral details and temperature dependence. *Hear Res*, 42(2-3):273–282, 1989.

[33] C. Köppl and G. A. Manley. Spontaneous otoacoustic emissions in the bobtail lizard. I: General characteristics. *Hear Res*, 71(1-2):157–169, 1993.

[34] G. A. Manley, L. Gallo, and C. Köppl. Spontaneous otoacoustic emissions in two gecko species, gekko gecko and eublepharis macularius. *J. Acoust. Soc. Am.*, 99(3):1588–1603, 1996.

[35] G. Taschenberger and G. A. Manley. Spontaneous otoacoustic emissions in the barn owl. *Hear Res*, 110(1-2):61–76, 1997.

[36] J. F. Ashmore. A fast motile response in guinea-pig outer hair cells: the cellular basis of the cochlear amplifier. *J Physiol*, 388:323–347, 1987.

[37] P. Dallos. The active cochlea. *J. Neurosci.*, 12(12):4575–4585, 1992.

[38] A. J. Hudspeth, Y. Choe, A. D. Mehta, and P. Martin. Putting ion channels to work: mechanoelectrical transduction, adaptation, and amplification by hair cells. *Proc. Natl. Acad. Sci. USA*, 97(22):11765–11772, 2000.

[39] M. S. Smotherman and P. M. Narins. Hair cells, hearing and hopping: a field guide to hair cell physiolog in the frog. *J. Exp. Biol.*, 203:2237–2246, 2000.

[40] J C-Dalsgaard. *Sound Source Localization*. Springer, 2005.

[41] D. P. Corey and A. J. Hudspeth. Response latency of vertebrate hair cells. *Biophys J*, 26(3):499–506, 1979.

[42] A. J. Hudspeth. How the ear's works work: mechanoelectrical transduction and amplification by hair cells. *C.R.Biol.*, 328(2):155–162, 2005.

[43] J. Howard, W. M. Roberts, and A. J. Hudspeth. Mechanoelectrical transduction by hair cells. *Annu.Rev.Biophys.Biophys.Chem.*, 17:99–124, 1988.

[44] D. P. Corey and J. A. Assad. Transduction and adaptation in vertebrate hair cells: correlating structure with function. *Soc Gen Physiol Ser*, 47:325–342, 1992.

[45] J. R. Holt and D. P. Corey. Two mechanisms for transducer adaptation in vertebrate hair cells. *Proc Natl Acad Sci U S A*, 97(22):11730–11735, 2000.

[46] J. A. Assad, G. M. Shepherd, and D. P. Corey. Tip-link integrity and mechanical transduction in vertebrate hair cells. *Neuron*, 7(6):985–994, Dec 1991.

[47] B. Kachar, M. Parakkal, M. Kurc, Y. Zhao, and P. G. Gillespie. High-resolution structure of hair-cell tip links. *Proc.Natl.Acad.Sci U.S.A*, 97(24):13336–13341, 2000.

[48] J. Siemens, C. Lillo, R. A. Dumont, A. Reynolds, D. S. Williams, P. G. Gillespie, and U. Müller. Cadherin 23 is a component of the tip link in hair-cell stereocilia. *Nature*, 428(6986):950–955, 2004.

[49] Z. M. Ahmed, R. Goodyear, S. Riazuddin, A. Lagziel, P. K. Legan, M. Behra, S. M. Burgess, K. S. Lilley, E. R. Wilcox, S. Riazuddin, A. J. Griffith, G. I. Frolenkov, I. A. Belyantseva, G. P. Richardson, and T. B. Friedman. The tip-link antigen, a protein associated with the transduction complex of sensory hair cells, is protocadherin-15. *J Neurosci*, 26(26):7022–7034, 2006.

[50] R. A. Jacobs and A. J. Hudspeth. Ultrastructural correlates of mechanoelectrical transduction in hair cells of the bullfrog's internal ear. In *Cold Spring Harbor symposia on quantitative biology*, volume 55, pages 547–561. Cold Spring Harbor Laboratory Press, 1990.

[51] A. Flock, B. Flock, and E. Murray. Studies on the sensory hairs of receptor cells in the inner ear. *Acta Otolaryngol*, 83(1-2):85–91, 1977.

[52] A. S. Kozlov, T. Risler, and A. J. Hudspeth. Coherent motion of stereocilia assures the concerted gating of hair-cell transduction channels. *Nat Neurosci*, 10(1):87–92, 2007.

[53] K. D. Karavitaki and D. P. Corey. Sliding adhesion confers coherent motion to hair cell stereocilia and parallel gating to transduction channels. *J. Neurosci*, 30(27):9051–9063, 2010.

[54] C. E. Strimbu, A. Kao, J. Tokuda, D. Ramunno-Johnson, and D. Bozovic. Dynamic state and evoked motility in coupled hair bundles of the bullfrog sacculus. *Hear. Res.*, 265(1-2):38–45, 2010.

[55] J. Barral, K. Dierkes, B. Lindner, F. Jülicher, and P. Martin. Coupling a sensory hair-cell bundle to cyber clones enhances nonlinear amplification. *Proc. Natl. Acad. Sci. USA*, 107(18):8079–8084, 2010.

[56] K. Dierkes, B. Lindner, and F. Jülicher. Enhancement of sensitivity gain and frequency tuning by coupling of active hair bundles. *Proc. Natl. Acad. Sci. USA*, 105(48):18669–18674, 2008.

[57] K. Dierkes, F. Jülicher, and B. Lindner. A mean-field approach to elastically coupled hair bundles. *Eur Phys J E Soft Matter*, 35(5):37, 2012.

[58] K. J. Kim and K. H. Ahn. Amplitude death of coupled hair bundles with stochastic channel noise. *Phys Rev E Stat Nonlin Soft Matter Phys*, 89(4):042703, 2014.

[59] D. P. Corey and A. J. Hudspeth. Ionic basis of the receptor potential in a vertebrate hair cell. *Nature*, 281(5733):675–677, 1979.

[60] R. A. Eatock. Adaptation in hair cells. *Annu. Rev. Neurosci.*, 23:285–314, 2000.

[61] E. A. Stauffer, J. D. Scarborough, M. Hirono, E. D. Miller, K. Shah, J. A. Mercer, J. R. Holt, and P. G. Gillespie. Fast adaptation in vestibular hair cells requires myosin-1c activity. *Neuron*, 47(4):541–553, 2005.

[62] D. P. Corey and A. J. Hudspeth. Kinetics of the receptor current in bullfrog saccular hair cells. *The journal of Neuroscience*, 3(5):962–976, 1983.

[63] A. C. Crawford, M. G. Evans, and R. Fettiplace. The actions of calcium on the mechano-electrical transducer current of turtle hair cells. *J. Physiol.*, 434:369–398, 1991.

[64] A. J. Ricci and R. Fettiplace. Calcium permeation of the turtle hair cell mechanotransducer channel and its relation to the composition of endolymph. *J. Physiol*, 506 ( Pt 1):159–173, 1998.

[65] A. W. Peng, T. Effertz, and A. J. Ricci. Adaptation of mammalian auditory hair cell mechanotransduction is independent of calcium entry. *Neuron*, 80(4):960–972, 2013.

[66] J. R. Holt, S. K. H. Gillespie, D. W. Provance, K. Shah, K. M. Shokat, D. P. Corey, J. A. Mercer, and P. G. Gillespie. A chemical-genetic strategy implicates myosin-1c in adaptation by hair cells. *Cell*, 108(3):371–381, 2002.

[67] J. Y. Tinevez, F. Jülicher, and P. Martin. Unifying the various incarnations of active hair-bundle motility by the vertebrate hair cell. *Biophys.J.*, 93(11):4053–4067, 2007.

[68] E. L. M. Cheung and D. P. Corey. $Ca^{2+}$ changes the force sensitivity of the hair-cell transduction channel. *Biophys J*, 90(1):124–139, 2006.

[69] M. E. Benser, R. E. Marquis, and A. J. Hudspeth. Rapid, active hair bundle movements in hair cells from the bullfrog's sacculus. *J. Neurosci.*, 16(18):5629–5643, 1996.

[70] P. G. Gillespie and D. P. Corey. Myosin and adaptation by hair cells. *Neuron*, 19(5):955–958, 1997.

[71] D. Lenzi and W. M. Roberts. Calcium signalling in hair cells: multiple roles in a compact cell. *Curr Opin Neurobiol*, 4(4):496–502, 1994.

[72] N. Hacohen, J. A. Assad, W. J. Smith, and D. P. Corey. Regulation of tension on hair-cell transduction channels: displacement and calcium dependence. *J Neurosci*, 9(11):3988–3997, 1989.

[73] A. Vilfan and T. Duke. Two adaptation processes in auditory hair cells together can provide an active amplifier. *Biophys. J.*, 85(1):191–203, 2003.

[74] R. Fettiplace. Active hair bundle movements in auditory hair cells. *J. Physiol.*, 576:29–36, 2006.

[75] R. Fettiplace and A. C. Crawford. The origin of tuning in turtle cochlear hair cells. *Hear. Res.*, 2(3-4):447–454, 1980.

[76] A. C. Crawford and R. Fettiplace. An electrical tuning mechanism in turtle cochlear hair cells. *J. Physiol.*, 312:377–412, 1981.

[77] R. S. Lewis and A. J. Hudspeth. Voltage- and ion-dependent conductances in solitary vertebrate hair cells. *Nature*, 304(5926):538–541, 1983.

[78] A. J. Hudspeth and R. S. Lewis. Kinetic analysis of voltage- and ion-dependent conductances in saccular hair cells of the bull-frog, rana catesbeiana. *J. Physiol.*, 400:237–274, 1988.

[79] A. J. Hudspeth and R. S. Lewis. A model for electrical resonance and frequency tuning in saccular hair cells of the bull-frog, rana catesbeiana. *J. Physiol.*, 400:275–297, 1988.

[80] J. F. Ashmore. Frequency tuning in a frog vestibular organ. *Nature*, 304(5926):536–538, 1983.

[81] C. J. Kros and M. G. Evans. Tuning in to cochlear hair cells. *J. Physiol*, 576(Pt 1):7–9, 2006.

[82] J. E. Songer and R. A. Eatock. Tuning and timing in mammalian type i hair cells and calyceal synapses. *J. Neurosci*, 33(8):3706–3724, 2013.

[83] A. Rodriguez-Contreras and E. N. Yamoah. Direct measurement of single-channel $Ca^{2+}$ currents in bullfrog hair cells reveals two distinct channel subtypes. *J Physiol*, 534(Pt 3):669–689, 2001.

[84] L. Catacuzzeno, B. Fioretti, P. Perin, and F. Franciolini. Frog saccular hair cells dissociated with protease viii exhibit inactivating bk currents, k(v) currents, and low-frequency electrical resonance. *Hear.Res.*, 175(1-2):36–44, 2003.

[85] L. Catacuzzeno, B. Fioretti, and F. Franciolini. Voltage-gated outward k currents in frog saccular hair cells. *J. Neurophysiol.*, 90(6):3688–3701, 2003.

[86] L. Catacuzzeno, B. Fioretti, P. Perin, and F. Franciolini. Spontaneous low-frequency voltage oscillations in frog saccular hair cells. *J. Physiol.*, 561:685–701, 2004.

[87] F. Jørgensen and A.B. Kroese. Ion channel regulation of the dynamical instability of the resting membrane potential in saccular hair cells of the green frog (rana esculenta). *Acta Physiol. Scand.*, 185(4):271–290, 2005.

[88] C. E. Armstrong and W. M. Roberts. Electrical properties of frog saccular hair cells: distortion by enzymatic dissociation. *J Neurosci*, 18(8):2962–2973, 1998.

[89] A. B. Neiman, K. Dierkes, B. Lindner, L. Han, and A. L. Shilnikov. Spontaneous voltage oscillations and response dynamics of a hodgkin-huxley type model of sensory hair cells. *The Journal of Mathematical Neuroscience (JMN)*, 1(1):1–24, 2011.

[90] M. Ospeck, V. M. Eguiluz, and M. O. Magnasco. Evidence of a hopf bifurcation in frog hair cells. *Biophys. J.*, 80(6):2597–2607, 2001.

[91] M. A. Rutherford and W. M. Roberts. Frequency selectivity of synaptic exocytosis in frog saccular hair cells. *Proc Natl Acad Sci U S A*, 103(8):2898–2903, 2006.

[92] Y. Kataoka and H. Ohmori. Activation of glutamate receptors in response to membrane depolarization of hair cells isolated from chick cochlea. *J. Physiol*, 477 ( Pt 3):403–414, 1994.

[93] E. C. Keen and A. J. Hudspeth. Transfer characteristics of the hair cell's afferent synapse. *Proc Natl Acad Sci U S A*, 103(14):5537–5542, 2006.

[94] W. Denk and W.W. Webb. Forward and reverse transduction at the limit of sensitivity studied by correlating electrical and mechanical fluctuations in frog saccular hair cells. *Hear. Res.*, 60(1):89–102, 1992.

[95] J. A. Assad, N. Hacohen, and D. P. Corey. Voltage dependence of adaptation and active bundle movement in bullfrog saccular hair cells. *Proc Natl Acad Sci U S A*, 86(8):2918–2922, 1989.

[96] J. Howard and A. J. Hudspeth. Compliance of the hair bundle associated with gating of mechanoelectrical transduction channels in the bullfrog's saccular hair cell. *Neuron*, 1(3):189–199, 1988.

[97] F. Jørgensen and H. Ohmori. Amiloride blocks the mechano-electrical transduction channel of hair cells of the chick. *J Physiol*, 403:577–588, 1988.

[98] L. Han and A. B. Neiman. Spontaneous oscillations, signal amplification, and synchronization in a model of active hair bundle mechanics. *Phys Rev E*, 81:041913, 2010.

[99] K. A. Montgomery, M. Silber, and S. A. Solla. Amplification in the auditory periphery: the effect of coupling tuning mechanisms. *Phys Rev E*, 75(5 Pt 1):051924, 2007.

[100] R. A. Eatock, D. P. Corey, and A. J. Hudspeth. Adaptation of mechanoelectrical transduction in hair cells of the bullfrog's sacculus. *J. Neurosci.*, 7(9):2821–2836, 1987.

[101] A. J. Ricci, A. C. Crawford, and R. Fettiplace. Tonotopic variation in the conductance of the hair cell mechanotransducer channel. *Neuron*, 40(5):983–990, 2003.

[102] A. J. Hudspeth. Hair-bundle mechanics and a model for mechanoelectrical transduction by hair cells. *Soc. Gen. Physiol Ser.*, 47:357–370, 1992.

[103] D. Clausznitzer, B. Lindner, F. Jülicher, and P. Martin. Two-state approach to stochastic hair bundle dynamics. *Phys.Rev.E.Stat.Nonlin.Soft.Matter Phys.*, 77(4 Pt 1):041901–, 2008.

[104] W. Denk and W.W. Webb. Thermal-noise-limited transduction observed in mechanosensory receptors of the inner ear. *Phys. Rev. Lett.*, 63(2):207–210, 1989.

[105] Y. A. Kuznetsov. *ftp://ftp.cwi.nl/pub/CONTENT*.

[106] P. E. Kloeden and E. Platen. *Numerical solution of stochastic differential equations*, volume 23. Springer, 1992.

[107] J. S. Bendat and A. G. Piersol. *Random data analyis and measurement procedures*. Wiley, New York, 3rd edition, 2000.

[108] B. Lindner, K. Dierkes, and F. Jülicher. Local exponents of nonlinear compression in periodically driven noisy oscillators. *Phys. Rev. Lett.*, 103(25):250601, 2009.

[109] I. Bashkirtseva, A. B. Neiman, and L. Ryashko. Stochastic sensitivity analysis of the noise-induced excitability in a model of a hair bundle. *Phys Rev E Stat Nonlin Soft Matter Phys*, 87(5):052711, 2013.

[110] R. M. Amro and A. B. Neiman. Effect of voltage oscillations on response properties in a model of sensory hair cell. In *International Conference on Theory and Application in Nonlinear Dynamics (ICAND 2012)*, pages 237–247. Springer, 2014.

[111] A. Pikovsky, M. Rosenblum, and J. Kurths. *Synchronization: a universal concept in nonlinear sciences*, volume 12. Cambridge university press, 2003.

[112] A. N. Malakhov. *Fluctuations in freely oscillating systems*. Nauka, Moscow, 1968.

[113] R. M. Amro, B. Lindner, and A. B. Neiman. Phase diffusion in unequally noisy coupled oscillators. *Phys. Rev. Lett.*, 115(3):034101, 2015.

[114] Y. Choe, M.O. Magnasco, and A.J. Hudspeth. A model for amplification of hair-bundle motion by cyclical binding of $Ca^{2+}$ to mechanoelectrical-transduction channels. *Proc.Natl.Acad.Sci U.S.A*, 95(26):15321–15326, 1998.

[115] Y. A. Kuznetsov. Topological equivalence, bifurcations, and structural stability of dynamical systems. *Elements of Applied Bifurcation Theory*, pages 39–78, 1998.

[116] E. M. Izhikevich. *Dynamical systems in neuroscience*. MIT press, 2007.

[117] F. Jülicher, K. Dierkes, B. Lindner, J. Prost, and P. Martin. Spontaneous movements and linear response of a noisy oscillator. *Eur. Phys. J. E.*, 29(4):449–460, 2009.

[118] R. Shlomovitz, L. F. Hemsing, A. Kao, S. W. F. Meenderink, R. Bruinsma, and D. Bozovic. Low frequency entrainment of oscillatory bursts in hair cells. *Biophys J*, 104(8):1661–1669, 2013.

[119] R. Shlomovitz, Y. Roongthumskul, S. Ji, D. Bozovic, and R. Bruinsma. Phase-locked spiking of inner ear hair cells and the driven noisy adler equation. *Interface focus*, 4(6):20140022, 2014.

[120] Z. Liu, B. Li, and Y. C. Lai. Enhancing mammalian hearing by a balancing between spontaneous otoacoustic emissions and spatial coupling. *Europhysics Letters*, 98(2):20005, 2012.

[121] D. G. Aronson, G. B. Ermentrout, and N. Kopell. Amplitude response of coupled oscillators. *Physica D: Nonlinear Phenomena*, 41(3):403 – 449, 1990.

[122] V. S. Anishchenko, S. Astakhov, and T. Vadivasova. Phase dynamics of two coupled oscillators under external periodic force. *EPL (Europhysics Letters)*, 86(3):30003, 2009.

[123] B. Lindner, M. Kostur, and L. Schimansky-Geier. Optimal diffusive transport in a tilted periodic potential. *Fluctuation and Noise Letters*, 01(01):R25–R39, 2001.

[124] H. Risken. *Fokker-Planck Equation*. Springer, 1984.

[125] L. Gammaitoni, P. Hänggi, P. Jung, and F. Marchesoni. Stochastic resonance. *Reviews of modern physics*, 70(1):223, 1998.

[126] V. S. Anishchenko, A. B. Neiman, F. Moss, and L. Shimansky-Geier. Stochastic resonance: noise-enhanced order. *Physics-Uspekhi*, 42(1):7, 1999.

[127] B. Lindner and L. Schimansky-Geier. Analytical approach to the stochastic fitzhugh-nagumo system and coherence resonance. *Physical Review E*, 60(6):7270, 1999.

[128] B. Lindner and L. Schimansky-Geier. Coherence and stochastic resonance in a two-state system. *Physical Review E*, 61(6):6103, 2000.

[129] S. G. Lee, A. B. Neiman, and S. Kim. Coherence resonance in a hodgkin-huxley neuron. *Physical Review E*, 57(3):3292, 1998.

[130] C. W. Gardiner. *Handbook of stochastic methods for physics, chemistry and the natural sciences*. Springer-Verlag, 1994.

[131] H. Sakaguchi, S. Shinomoto, and Y. Kuramoto. Phase transitions and their bifurcation analysis in a large population of active rotators with mean-field coupling. *Progress of Theoretical Physics*, 79(3):600–607, 1988.

[132] R. T. Botts, A. J. Homburg, and T. R. Young. The hopf bifurcation with bounded noise. *Discrete and continuous dynamical systems. Series A*, 32(8):2997, 2012.


Thesis and Dissertation Services